

# BEYOND STANDARD MODEL, LHC PHENOMENOLOGY AND DARK MATTER

BY YUE ZHAO

A dissertation submitted to the  
Graduate School—New Brunswick  
Rutgers, The State University of New Jersey  
in partial fulfillment of the requirements  
for the degree of  
Doctor of Philosophy  
Graduate Program in Physics and Astronomy

Written under the direction of  
Professor Scott Thomas  
and approved by

---

---

---

---

---

New Brunswick, New Jersey

October, 2012

## **ABSTRACT OF THE DISSERTATION**

# **BEYOND STANDARD MODEL, LHC PHENOMENOLOGY AND DARK MATTER**

**by Yue Zhao**

**Dissertation Director: Professor Scott Thomas**

The standard model in particle physics is such a successful model, which agrees well with almost all experimental tests in the past more than 20 years. However, there is large hope that new physics beyond the standard model would show up in the Large Hadron Collider (LHC). Meanwhile, many direct and indirect dark matter searches have shown signs of potential signals. If confirmed, the properties of the most mysterious but dominant part of matter constitute will be unveiled soon.

In this thesis, we mainly have three sections. First, we will talk in detail about LHC phenomenology. This includes several topics, recovering particle masses from missing energy signatures with displaced tracks, diagnosing the top-quark angular asymmetry using LHC intrinsic charge asymmetries, signature searches, including multi-lepton and diphoton searches, in the early LHC. After collider phenomenology, we will discuss a study for dark matter, which is focused on the indirect search, i.e. gamma ray spectra from dark matter annihilation and decay. And in the last section, we will cover several topics about some studies on formal side of physics, including metastable spontaneous SUSY breaking in a landscape of fuzzy droplets, entropic force and its fluctuation from gauge/gravity duality.

## Acknowledgements

First and foremost, I want to express my deepest appreciation to my advisor, Prof Scott Thomas. Without his guidance and continuous support, this dissertation would not have been possible. I am always impressed by the breadth and depth of his understanding on physics. I feel it is hard for me to find a topic which is interesting and Scott does not understand. I'm lucky to have him as my advisor. His door is always open, and he is always patient to answer my many and sometimes naive questions. I'm very grateful to him on so many helps, physics related or not, during the past 5 years.

Further, I would like to thank the faculties in both high energy theory and high energy experiment groups in Rutgers, Professor Tom Banks, John Paul Chou, Duiliu Emanuel Diaconescu, Dan Friedan, Yuri Gershtein, Eva Halkiadakis, Amitabh Lath, Sergei Lukyanov, Greg Moore, David Shih, Sunil Somalwar, Matt Strassler and Alexander Zamolodchikov. I also thank Shirley Hinds, Ronald Ransome, Diane Soyak, Richard Vaughn and Ted Williams for their help.

In particular, it is a pleasant time to have discussions with Evgeny Andriyash, Nathaniel Craig, Wu-yen Chuang, Rouven Essig, Jared Evans, Jean-Francois Fortin, Richard Gray, Jose Juknevich, Yevgeny Kats, Can Kilic and Jessie Shelton over the years.

I want to thank my fellow graduate students in NHETC, Simon Knapen, Pietro Longhi, Michael Park, Mohammad Ramezanali, Robert Schabinger and Omar Shams. Especially, I would like to thank Guang Pan and Yi Zhang for company and support through this 5 years, with lots of wonderful memory.

Finally, I thank my family, especially both my parents and my wife, for their continued love and support. I cannot imagine a life without them. And I appreciate to have them with me, no matter they are near around or half earth away.

## Dedication

*To*  
*My Parents*  
*&*  
*My Wife*

# Table of Contents

|   |     |
|---|-----|
| <b>Abstract</b> . . . . .   | ii  |
| <b>Acknowledgements</b> . . . . .   | iii |
| <b>Dedication</b> . . . . .   | iv  |
| <b>1. Introduction</b> . . . . .  | 1   |
| 1.1. LHC Phenomenology . . . . .  | 1   |
| 1.2. Searches of Dark Matter . . . . .  | 3   |
| 1.3. Formal studies of high energy theory . . . . .   | 3   |
| <b>2. Recovering Particle Masses from Missing Energy Signatures with Displaced Tracks</b> . . . . .   | 5   |
| 2.1. Introduction . . . . .   | 5   |
| 2.2. Counting the Unknowns . . . . .  | 7   |
| 2.3. Parameterizing the Unknowns . . . . .  | 9   |
| 2.4. Examples with a Massless LSP . . . . .   | 12  |
| 2.5. Examples with a Massive LSP . . . . .  | 18  |
| 2.6. Conclusions . . . . .  | 24  |
| 2.7. Appendix A . . . . .   | 26  |
| 2.8. Appendix B . . . . .   | 27  |
| <b>3. Diagnosing the Top-quark Angular Asymmetry Using LHC Intrinsic Charge Asymmetries</b> . . . . . | 31  |
| 3.1. Introduction . . . . .   | 31  |
| 3.2. Benchmark Models . . . . .   | 33  |
| 3.3. A mass variable . . . . .  | 35  |
| 3.4. Event selection and processing . . . . .   | 38  |
| 3.5. Analysis and results . . . . .   | 41  |
| 3.6. An angle variable . . . . .  | 49  |

|   |           |
|---|-----------|
| 3.7. Final Remarks . . . . .  | 51        |
| 3.8. Appendix A: Additional Results . . . . .   | 54        |
| 3.9. Appendix B: Strategy Details . . . . .   | 57        |
| 3.10. Appendix C: The $P_T$ -difference variables . . . . .                               | 58        |
| <b>4. Multi-Lepton GMSB Scenarios for Early LHC Running . . . . .</b>                     | <b>65</b> |
| 4.1. Introduction . . . . .   | 65        |
| 4.2. Benchmark Parameter Spaces . . . . .   | 66        |
| 4.3. Monte Carlo Simulations . . . . .  | 68        |
| <b>5. Entropic Force And its Fluctuation in Euclidian Quantum Gravity . . . . .</b>       | <b>72</b> |
| 5.1. Introduction . . . . .   | 72        |
| 5.2. Entropic Force in gauge/gravity duality . . . . .                                    | 74        |
| 5.3. Understanding Entropic Force From Gravity Side Alone . . . . .                       | 77        |
| 5.4. Thermal Fluctuation . . . . .  | 78        |
| 5.5. Discussion . . . . .   | 81        |
| <b>6. Metastable Spontaneous SUSY Breaking in a Landscape of Fuzzy Droplets . . . . .</b> | <b>86</b> |
| 6.1. Introduction . . . . .   | 86        |
| 6.2. The model . . . . .  | 86        |
| 6.3. Model without mass terms . . . . .   | 87        |
| 6.4. Model with mass terms . . . . .  | 93        |
| 6.5. Counting the number of vacua . . . . .   | 102       |

# Chapter 1

## Introduction

### 1.1 LHC Phenomenology

The standard model in particle physics has passed plenty of experimental tests during the past more than 20 years. However, many questions in the standard model remained to be answered, for example the hierarchy problem in Electroweak theory, the unified description of gravity with other forces, dark matter and dark energy, etc. Without new data at a much higher energy, people do not have a clear clue on what is the correct direction to pursue.

Now particle physics has entered a new exciting era, the excellent performance of the LHC at 7 TeV in 2011 brings us to a much higher energy region than previous colliders, people expect new physics may show itself in the current or maybe a little bit higher energy region. The 8 TeV and finally 14 TeV of the LHC may provide us the clues for new physics beyond the standard model.

In the first part of this thesis, I would like to discuss several research projects related to the study in the LHC.

First we talk about extracting particle masses from missing energy signatures with displaced tracks using just a few events. This project aims to extract the essential information of new physics if they leave a signature as displaced vertices or tracks. We analyze the kinematics of dual cascade decays ending with a stable non-interacting particle which is the sole source of missing energy. We find that if the next-to-lightest particle in the spectrum is metastable with a finite decay length, then a measurement of the resulting displaced vertices or tracks can be used to constrain the problem enough to measure masses with just a few events. If the event contains two measurable displaced vertices, then mass measurement can be made with  $O(1)$  event. If event contains displaced tracks only, we develop some techniques to make the mass measurements with  $O(10)$  events, in several different scenarios. We find when the number of unknowns is more than number of constraints in the system, by scanning one kinematic parameter, one gains an extra effective constraint to help solving the system. Due to the low request on number of events, these techniques can be applied to the very early stage of discovery.

Nature can be surprising and it is very plausible that unexpected signals could show up, providing us hints for new physics. Currently, the most robust anomaly in Tevatron is the top-antitop forward-backward asymmetry. We will discuss diagnosing the top-quark angular asymmetry using LHC intrinsic charge asymmetries. Tevatron finds a strong hint for deviation from SM prediction in the measurement of  $t\bar{t}$  forward-backward asymmetry. This may serve as a clue to new physics. Flavor-violating interactions involving new heavy particles are among proposed explanations for the  $t\bar{t}$  forward-backward asymmetry observed at the Tevatron. Many of these models generate a  $t\bar{t}$ -plus-jet signal at the LHC. In this paper we identify several new charge asymmetric variables in  $t\bar{t}j$  events that can contribute to the discovery of such models at the LHC. We propose a data-driven method for the background, largely eliminating the need for a Monte Carlo prediction of  $t\bar{t}$ -plus-jets, and thus reducing systematic errors. With a fast detector simulation, we estimate the statistical sensitivity of our variables for one of these models, finding that with 5 inverse fb the LHC experiments should be able to exclude the Standard Model across much of the mass and coupling range. Should any signal appear, our variables will be useful in distinguishing classes of models from one another.

Classifying models by their signature is a very efficient way, and it makes the search more model and detailed spectrum independent. SUSY models are well motivated, and can serve as benchmarks for many signatures. At last of the section of the LHC phenomenology, we will briefly discuss multi-lepton and diphoton searches in the early LHC. Low scale gauge-mediated supersymmetry breaking naturally gives rise to superpartner spectra with nearly degenerate right-handed sleptons playing the role of co-next to lightest superpartner (co-NLSP), with a bino-like neutralino as the next to next to lightest superpartner (NNLSP). For spectra of this type, cascade decays from heavier superpartners always pass sequentially through the bino, then to one of the co-NLSP sleptons emitting a lepton, and finally to the un-observed Goldstino, emitting another lepton. Therefore, pair-production of heavier superpartners gives rise to inclusive signatures that include four hard leptons and missing transverse energy. This signature is best covered by an exclusive hierarchical search for quad-leptons, tri-leptons, and same-sign dileptons, including missing energy in the latter two cases as necessitated by backgrounds. A reach or upper limit on multi-lepton signature as a function of the gluino and the chargino masses provides a unified summary of the sensitivity to this topology for both strong and weak production of superpartners.



## 1.2 Searches of Dark Matter

Dark matter is the most mysterious but dominant constituent of matter. Recently, some DM experiments show hints of signals, both in direct and indirect detections. The next few years could be a crucial era for exploring DM.

In this section, we study gamma ray spectra for various scenarios of dark matter annihilation and decay. We focus on the processes which can only generate high energy leptons and photons but no proton/anti-proton, to be compatible with PAMELA's data. We generically divide the processes into two kinds: one is photons generated by final state radiation from high energy leptons, and the one where photons directly generated from high order (non-renormalizable) operators which are obtained after one integrates out the heavy modes. We compare the amplitudes of those two kinds, assuming different properties of dark matter particles. A rough estimation gives us that if the particle mediates the annihilation/decay process is heavier than  $\mathcal{O}(1000\text{TeV})$ , all spectra are dominated by final state radiation. And if lighter than  $\mathcal{O}(1000\text{TeV})$ , the spectra of some processes are dominated by photons directly from higher order operators, which are peaked more likely at high energy regime than the ones from final state radiation.

## 1.3 Formal studies of high energy theory

### 1.3.1 Entropic force and its fluctuation in Euclidian Quantum Gravity

The thermodynamics of black hole has been studied for several decades since the discover of Hawking radiation. It reveals a deep connection between the structure and dynamics of space-time and laws of thermodynamics. And more recently, the work by Jacobson shows an explicit derivation from laws of thermodynamics to Einstein equation. The attempts to explain gravity as an emergent phenomena is based on the holographic principle. And AdS/CFT correspondence provides strong support and explicit examples on how thermodynamics of space-time can be related to thermodynamics of the dual system living on holographic screen.

In this section, we study the idea about gravity as entropic force proposed by Verlinde. By interpreting Euclidean gravity in the language of thermodynamic quantities on holographic screen, we find the gravitational force can be calculated from the change of entropy on the screen. We show normal gravity calculation can be reinterpreted in the language of thermodynamic variables. We also study the fluctuation of the force and find the fluctuation acting on the point-like particle can never be larger than the expectation value of the force. For a black

hole in AdS space, by gauge/gravity duality, the fluctuation may be interpreted as arising from thermal fluctuation in the boundary description. And for a black hole in flat space, the ratio between fluctuation and force goes to a constant  $\frac{T}{m}$  at infinity.

### 1.3.2 Metastable Spontaneous SUSY Breaking in a Landscape of Fuzzy Droplets

Supersymmetric field theory has many fantastic features. A class of  $\mathcal{N} = 1$  supersymmetric theories with gauge group  $U(N_c)$  and chiral multiplet matter in the adjoint representation along with  $N_f$  flavors of fundamental plus anti-fundamental is analyzed. With non-vanishing Fayet-Iliopoulos and matter field mass terms, these theories are shown to have a landscape of metastable vacua with spontaneously broken supersymmetry. The adjoint field configurations in the local metastable vacua are non-commutative, and may be interpreted as a fluid consisting of fuzzy droplets in a confining potential. And the excited states of the meta-stable vacua may be interpreted as excitations of the fuzzy fluid droplets. The number of metastable vacua is exponentially large in the product of the gauge group rank and number of flavors. In the limit of large ratio of Fayet-Iliopoulos to mass terms, the lifetime of the metastable vacua become exponentially large in the inverse square of this ratio. The theories analyzed here could provide a simple analog model for a landscape of metastable vacua that may arise in certain classes of string or M-theory compactifications with blown-up branes dissolved inside branes.

## Chapter 2

# Recovering Particle Masses from Missing Energy Signatures with Displaced Tracks

### 2.1 Introduction

The Large Hadron Collider (LHC), now in the early stages of discovery level searches, is currently probing the weak scale for signs of physics beyond the Standard Model (SM). Although a model independent approach to new physics searches should primarily involve searching for deviations from SM predictions of any kind, a specific discovery cannot be claimed without more detailed information about the processes that occur subsequent to the initial particle collisions. Therefore obtaining precise measurements of theoretical parameters, such as the mass spectrum of new particle states, is an endeavor of particular importance.

In this paper, we propose techniques for measuring particle masses from several different signatures containing missing transverse momentum. We assume that some heavy new particle states are pair produced and then participate in sequential two-body cascade decays that produce visible SM particles, until some effectively stable and non-interacting new particle is reached at the bottom of the decay chain. This is the canonical and well-studied “dual cascade decay chain” signature, well known for being the canonical signature of R-parity conserving supersymmetry (SUSY) models. None of the kinematic techniques discussed in this paper will rely on the fact that the cascade decay chains be supersymmetric in nature, thus all of these techniques may be applied generally to any BSM model that contains this topology as a signature. However, due to the familiarity with supersymmetric terminology, we will generically refer to the “Lightest meta-Stable Particle” as the “LSP” and the “Next-to-Lightest meta-Stable Particle” as the “NLSP”. Our analysis will focus on a subset of these scenarios in which the last step of the cascade decay involves some long-lived new particle state that travels a finite distance before decaying in flight. This will result in a signature of displaced vertices or displaced tracks in the detector.

The techniques to be described here are model independent which is fortunate since missing transverse momentum is a fairly generic feature of models for physics beyond the SM. This

is because general phenomenological considerations often motivate new discrete symmetries, resulting in the presence of effectively non-interacting stable particle states. In the case of SUSY for example, R-parity is often invoked to exclude dangerous operators that can result in phenomenologically inconsistent effects like proton decay. In the case of extra dimensional models, it is the conservation of momentum along the extra dimension that will result in the pair production of Kaluza-Klein (KK) states and subsequently guarantee the stability of the lightest KK mode. One can even invoke cosmological arguments like the “WIMP Miracle” calculations to argue that missing energy signatures might be a generic phenomenologically desirable feature of models for new physics at the weak scale. The presence of metastable new particle states is also fairly common and can arise in supersymmetric models with low scale SUSY breaking or scenarios where R-parity conservation is only approximate. In this paper, we address the question of whether or not it is possible, under any circumstances, to recover all of the kinematic information lost through missing energy on an event-by-event basis.

If all of the final state particles from a given collision are visible through the detector, then the measurement of on-shell particle masses can easily be performed through the straightforward reconstruction of a mass resonance peak. However, if one or more of the final state particles are effectively stable and non-interacting, then the situation is much more challenging. In particular, particle masses cannot be calculated directly on a mass peak resonance since crucial kinematic quantities cannot be measured. In response to this issue, many general techniques have been developed for performing indirect measurements of particle masses through cleverly constructed kinematic variables (1; 2; 3; 4; 5; 6). In particular, the author in (9) introduces a very generic method for constructing such variables via phase space singularity structures. Many studies have also been performed based on kinematics specific to the canonical cascade decay chain (10; 11; 12; 13; 14; 15; 16; 17; 18; 19; 20; 21; 22; 23; 24; 25). In general, novel kinematic structures that characterize an event can often be used to reconstruct lost information. For example, (7; 8) also discuss a long-lived NLSP, and the use of timing information to perform such reconstructions. For different topologies of the decay chain, (26) provides a comprehensive review. The drawback to most of these methods is the fact that most of the kinematic variables that can be constructed to provide an indirect mass measurement, require a very large number of events for telling features to become practically visible in statistical distributions. These methods would therefore be difficult to utilize during early discovery level searches.

First, using our assumptions we will show that one can write down an expression for the 3-momenta of each LSP as a function of the direction of the 3-momenta of each NLSP. This unit vector can then be written in terms of the locations of the secondary vertices. We will

then follow with a description of some novel methods for reconstructing particle masses using this information. Examples of explicit mass reconstruction will be performed using Monte Carlo parton-level data, highlighting the effectiveness of these methods in some of the diverse topologies that can occur within the cascade. Finally we will conclude with a discussion of how this relates to current SUSY searches being performed at the LHC. We argue then, that the optimal strategy for “searching under the lamp post” during these early runs will be to search for signatures with two displaced vertices (or two displaced tracks in situations where the exact location of the secondary vertices cannot be measured).

## 2.2 Counting the Unknowns

Let us denote the stable LSP particles by  $X_1$  and  $Y_1$ , their mother NLSP particles as  $X_2$  and  $Y_2$  and the final visible SM particles as  $a_1$  and  $b_1$ . Figure [2.1] shows a diagram of a typical event. Since we assume that the 4-momenta of the two LSP’s are not measurable, each event yields 8 unknown quantities. The transverse missing momentum is given by the vector sum of the LSP 3-momenta projected onto the transverse plane. Since this plane is 2-dimensional, a missing transverse momentum measurement eliminates 2 degrees of freedom bringing the number of unknowns down to 6. In order to construct constraint equations with which to solve for these unknowns, we follow the work of (27; 28; 29) and assume some symmetry between the two sides of the decay chains. For example, if we assume that  $m_{X_2} = m_{Y_2}$  then we can use the fact that  $(p_{X_1}^\mu + p_{a_1}^\mu)^2 = (p_{Y_1}^\mu + p_{b_1}^\mu)^2$  as a constraint with which to eliminate one of the unknown momentum components.

Let  $k$  denote the number of such equations we can construct. Since all of the unknown quantities involve components of the LSP 4-momenta,  $k$  can be viewed as the number of masses starting from the bottom of one decay chain but excluding the LSP, that we assume to be equal to the masses on the opposite side of the decay chain. Utilizing these constraints, the number of unknowns can be reduced to  $6 - k$ . It is important to keep in mind however, that such an exact relationship between the masses of these particles only holds in the very narrow width limit. In general, the true kinematically reconstructed masses will lie on the distribution of some mass peak resonance and the equality of the masses will only be approximately true. This will affect both the accuracy of the mass measurement as well as potentially the existence of solutions to the constraint equations. We will return to a more detailed discussion of this in the body of the paper.

If we assume that we have access to  $m$  events with the same topology then we can use

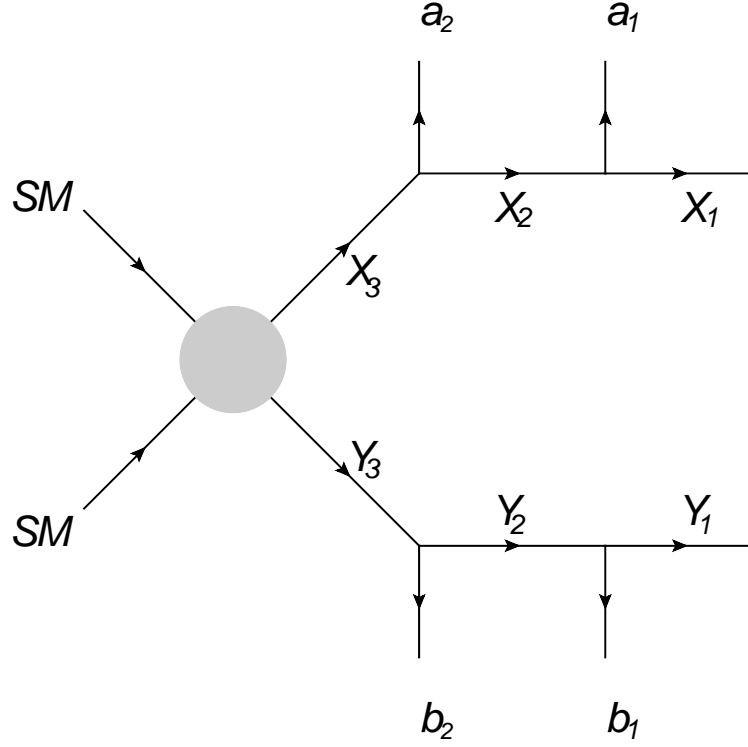


Figure 2.1: The decay topology for the canonical dual cascade decay chain. Two heavy new particle states ( $X_3$  and  $Y_3$ ) are pair produced. They then cascade down to a pair of non-interacting stable particles ( $X_1$  and  $Y_1$ ) shooting off visible SM particles ( $a_1$ ,  $b_1$ ,  $a_2$  and  $b_2$ ) along the way.

the equality of masses across events to further constrain the problem as done in (27; 28; 29). For the first event we counted  $6 - k$  unknowns. Each additional event contributes another  $6 - k$  unknowns but if we enforce the equality of masses across different events then we should subtract off another factor of  $k$ . Thus each additional event contributes  $6 - 2k$ . For  $m$  events, the total number of unknowns is  $6 - k + (m - 1)(6 - 2k) = 6m - 2km + k$ . The condition which must be satisfied in order to properly constrain the problem is thus clearly  $6m - 2km + k \leq 0$ .

Given our assumptions that the NLSP is the only particle in the spectrum with a finite and measurable decay length, an accurate measurement of the locations of the displaced vertices can be used to provide additional constraints. Here we assume that all of the decays occur on a microscopic length scale before the NLSP's travel a finite macroscopic distance and decay to a pair of invisible LSP's and a pair of visible SM particles. This implies that the direction of the NLSP 3-momentum is equal to the unit vector pointing in the direction of the secondary vertex. The NLSP unit 3-momentum contains two degrees of freedom, thus an accurate measurement of two displaced vertices will allow us to subtract off another  $4m$  unknowns. In some situations, it

will not be possible to measure the locations of the displaced vertices and only the trajectories of the displaced tracks will be visible. In these situations, the locations of the secondary vertices can be constrained to lie on the trajectories of the displaced tracks and can be parameterized by one number thus removing  $2m$  unknown quantities.

## 2.3 Parameterizing the Unknowns

In this section we propose a parameterization of the unknown quantities that makes the utility of displaced vertices and displaced tracks maximally transparent. More specifically, we will show that it will be possible to write down an expression for the 3-momenta of each LSP that depends only the location of the displaced vertices. Throughout this analysis let us assume that the 4-momenta of the visible Standard Model particles  $a_1$  and  $b_1$  can be measured accurately. Let us restrict our attention to one side of the decay chain and denote the 4-momenta for particle  $X_1$ ,  $X_2$  and  $a_1$  as in Eq. [2.3.1]

$$p_{X_1} = \begin{pmatrix} E_{X_1} \\ |\vec{p}_{X_1}| \hat{p}_{X_1} \end{pmatrix} \quad ; \quad p_{X_2} = \begin{pmatrix} E_{X_2} \\ |\vec{p}_{X_2}| \hat{p}_{X_2} \end{pmatrix} \quad ; \quad p_{a_1} = \begin{pmatrix} E_{a_1} \\ |\vec{p}_{a_1}| \hat{p}_{a_1} \end{pmatrix} \quad (2.3.1)$$

To isolate the unknown quantities, it is useful to decompose the 3-momenta of particles  $a_1$  and  $X_1$  in terms of their components parallel and orthogonal to the momentum of particle  $X_2$  as in Figure [2.2]. For notational convenience, let us define the projection symbol as in Eq. [2.3.2]

$$\mathbb{P}_j^i \equiv \vec{p}_i \cdot \hat{p}_j \quad (2.3.2)$$

This denotes the projection of the 3-momentum of particle  $i$  along the direction of the 3-momentum of a different particle  $j$ . In this basis and with this notation we can decompose  $\vec{p}_{a_1}$  into its components parallel  $\vec{p}_{a_1}^{\parallel} = \mathbb{P}_{X_2}^{a_1} \hat{p}_{X_2}$  and orthogonal  $\vec{p}_{a_1}^{\perp} = \vec{p}_{a_1} - \mathbb{P}_{X_2}^{a_1} \hat{p}_{X_2}$  to particle  $X_2$ . Conservation of momentum then allows us to immediately write down the orthogonal component of the 3-momentum of particle  $X_1$  as  $\vec{p}_{X_1}^{\perp} = -\vec{p}_{a_1}^{\perp} = \mathbb{P}_{X_2}^{a_1} \hat{p}_{X_2} - \vec{p}_{a_1}$ . The magnitude of the component of the 3-momentum of particle  $X_1$  along the direction of  $X_2$  remains unknown. In this paper we will denote the magnitude of this unknown as  $c_1 \equiv \mathbb{P}_{X_2}^{X_1}$  so the component of the LSP parallel to the direction of the NLSP can be expressed as  $\vec{p}_{X_1}^{\parallel} = c_1 \hat{p}_{X_2}$ . Since the other side of the decay chain is subject to identical kinematic considerations, the 3-momentum of each LSP is given by Eq. [2.3.3]

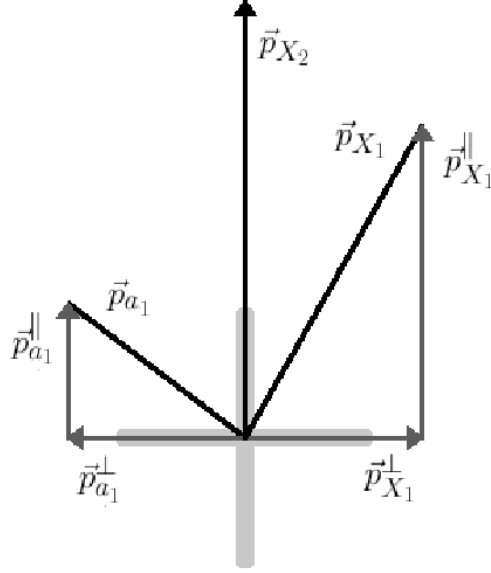


Figure 2.2: A decomposition of the final decay products into their components parallel and orthogonal to particle  $X_2$ . Note that the component of  $\vec{p}_{X_1}$  orthogonal to the direction of the NLSP, is equal in magnitude and opposite in direction to the component of  $\vec{p}_{a_1}$  orthogonal to the direction of the NLSP.

$$\vec{p}_{X_1} = (\mathbb{P}_{X_2}^{a_1} + c_1)\hat{p}_{X_2} - \vec{p}_{a_1} \quad \text{and} \quad \vec{p}_{Y_1} = (\mathbb{P}_{Y_2}^{b_1} + c_2)\hat{p}_{Y_2} - \vec{p}_{b_1} \quad (2.3.3)$$

Let  $\alpha = 1, 2$  be indices parameterizing a basis in the two-dimensional transverse plane. The experimentally measured missing transverse momentum  $\vec{\not{p}}_\alpha^T$  contains two degrees of freedom and is restricted to the transverse plane. Since by assumption, the missing transverse momentum in this scenario is taken from the vector sum of the 3-momenta of the two LSP's, it can be calculated as the sum of contributions from each LSP as in Eq. [2.3.4]

$$\vec{\not{p}}_\alpha^T = \vec{p}_\alpha^{X_1} + \vec{p}_\alpha^{Y_1} = (\mathbb{P}_{X_2}^{a_1} + c_1)\hat{p}_\alpha^{X_2} + (\mathbb{P}_{Y_2}^{b_1} + c_2)\hat{p}_\alpha^{Y_2} - \vec{p}_\alpha^{a_1} - \vec{p}_\alpha^{b_1} \quad (2.3.4)$$

These two equations can then be used to solve for  $c_1$  and  $c_2$  as in Eq. [2.3.5]

$$\begin{aligned} c_1 &= \frac{(p_\alpha^{a_1} p_\beta^{Y_2} + p_\alpha^{b_1} p_\beta^{Y_2} + \not{p}_\alpha p_\beta^{Y_2})\epsilon^{\alpha\beta}}{p_\alpha^{X_2} p_\beta^{Y_2} \epsilon^{\alpha\beta}} - \mathbb{P}_{X_2}^{a_1} \\ c_2 &= \frac{(p_\alpha^{a_1} p_\beta^{X_2} + p_\alpha^{b_1} p_\beta^{X_2} + \not{p}_\alpha p_\beta^{X_2})\epsilon^{\alpha\beta}}{p_\alpha^{Y_2} p_\beta^{X_2} \epsilon^{\alpha\beta}} - \mathbb{P}_{Y_2}^{b_1} \end{aligned} \quad (2.3.5)$$



Here  $\epsilon^{\alpha\beta}$  is the totally antisymmetric  $2 \times 2$  tensor. The key result here is that an accurate measurement of the missing transverse momentum will allow us to write down the 3-momentum of each LSP as a function of the direction of the NLSP 3-momenta by plugging Eq. [2.3.5] into Eq. [2.3.3]. The result is summarized by Eq. [2.3.6]

$$\begin{aligned}\vec{p}_{X_1} &\rightarrow \vec{p}_{X_1}(\hat{p}_{X_2}, \hat{p}_{Y_2}) \\ \vec{p}_{Y_1} &\rightarrow \vec{p}_{Y_1}(\hat{p}_{X_2}, \hat{p}_{Y_2})\end{aligned}\tag{2.3.6}$$

Let us denote the location of the two secondary vertices by 3-vectors in the Cartesian coordinates of the lab frame  $\vec{r}_X$  and  $\vec{r}_Y$ . Here the subscripts  $X$  and  $Y$  correspond to the location of the decays of particles  $X_2$  and  $Y_2$ . Note that given our assumptions  $|\vec{r}_X| = d_X$  is simply the distance traveled by particle  $X_2$  before decaying while  $|\vec{r}_Y| = d_Y$  is the distance traveled by particle  $Y_2$  before decaying, assuming all other decays are prompt. Now recall our initial assumption that the decay length of particles  $X_2$  and  $Y_2$  are the only decay lengths that are measurably large. Then subsequent to the initial collision, a cascade will occur on some microscopic length scale before the NLSP's travel a finite macroscopic distance and decay to a pair of invisible LSP's and a pair of visible SM particles. This implies that the direction of the NLSP 3-momentum is equal to the unit vector pointing in the direction of the secondary vertex. The exact relationship is  $\hat{p}_{X_2} = \vec{r}_X/|\vec{r}_X|$ . Therefore in actuality we have derived an expression for the LSP 3-momenta that depends only on the location of the secondary vertices as in Eq. [2.3.7]

$$\begin{aligned}\vec{p}_{X_1} &\rightarrow \vec{p}_{X_1}(\vec{r}_X, \vec{r}_Y) \\ \vec{p}_{Y_1} &\rightarrow \vec{p}_{Y_1}(\vec{r}_X, \vec{r}_Y)\end{aligned}\tag{2.3.7}$$

In some situations, the displaced vertices may not be directly measurable and only the trajectories of the displaced tracks may be extracted. However, it may be inferred that the displaced vertices must lie somewhere along the path of the displaced tracks. We may thus parameterize the location of the displaced vertices according to their location along the beam axis. Let  $z_X$  and  $z_Y$  denote the location along the z-axis of  $\vec{r}_X$  and  $\vec{r}_Y$  respectively and let us set the location of the primary vertex to be  $z = 0$ . Indeed if we denote the location of particle  $a_1$ 's collision with the tracker by  $\vec{r}_0 = (x_0, y_0, z_0)$ , then an exact functional form for  $\vec{r}_X(z_X)$  is given by Eq. [2.3.8]

$$\vec{r}_X(z_X) = \begin{pmatrix} x_0 + (p_x^{a_2}/p_z^{a_1})(z_X - z_0) \\ y_0 + (p_y^{a_2}/p_z^{a_1})(z_X - z_0) \\ z_X \end{pmatrix} \quad (2.3.8)$$

This will allow us to derive an expression for the LSP 3-momenta that depends only on the location of the secondary vertices along the beam axis as in Eq. [2.3.9]

$$\begin{aligned} \vec{p}_{X_1} &\rightarrow \vec{p}_{X_1}(z_X, z_Y) \\ \vec{p}_{Y_1} &\rightarrow \vec{p}_{Y_1}(z_X, z_Y) \end{aligned} \quad (2.3.9)$$

From this parameterization we can explicitly see the dependence of the 3-momentum of each missing particle on the locations of the displaced vertices or the trajectories of the displaced tracks. Now that it is clear how such measurements can be used to reduce the number of unknowns and further constrain the kinematics of this decay topology, we move on to some practical examples.

## 2.4 Examples with a Massless LSP

From the counting arguments given in the introduction, we found that for  $m$  events and  $k$  constraint equations, the total number of unknown quantities was equal to  $6m - 2km + k$ . In principle, the problem is simply a matter of solving for enough constraint equations to obtain a unique solution for all unknown quantities. In practice however, the constraint equations are highly nonlinear and generically contain multiple solutions. As a result, a confident mass measurement should really involve the analysis of a number of events greater than the minimum required to properly constrain the problem. We will now explore a few specific examples. For concreteness, we will start with an analysis of selected benchmark points for multi-lepton searches inspired by scenarios with general gauge mediated SUSY breaking (GMSB). In such scenarios, where the scale of SUSY breaking is sufficiently low, the LSP is an effectively massless gravitino. With the mass of the LSP set to zero,  $2m$  unknowns are removed from the problem resulting in a total number given by Eq. [2.4.1]

$$\text{Number of Unknowns for Massless LSP Scenario} = 4m - 2km + k \quad (2.4.1)$$

### 2.4.1 Measurable Displaced Vertices

If  $a_1$  and  $b_1$  each decay promptly to two or more visible particles, it will be possible to experimentally trace back the track of each decay product and reconstruct the position of the secondary vertex. The momenta  $p_{a_1}$  and  $p_{b_1}$  can then be computed through the sum of 4-momenta of their respective decay products, assuming none of them contribute to the missing transverse momentum. The situation is depicted in Figure [2.3]. In this case we can directly measure the quantities  $\hat{p}_{X_2} = \vec{r}_X/|\vec{r}_X|$  and  $\hat{p}_{Y_2} = \vec{r}_Y/|\vec{r}_Y|$  and thus completely solve for the 3-momenta of particles  $X_1$  and  $Y_1$ . Since these particles are massless by assumption, a measurement of the 3-momenta is equivalent to a measurement of the full 4-momenta. Therefore in situations where the LSP is massless, a simple measurement of the locations of the displaced vertices already recovers all of the information lost through missing energy. In terms of the unknowns we see that substituting one event  $m = 1$  into Eq. [2.4.1] gives us  $4 - k$ . A measurement of the displaced vertices removes exactly 4 unknowns, which means that the condition for total kinematic recovery is already met for  $k = 0$ . This example is thus trivial and will not be discussed further.

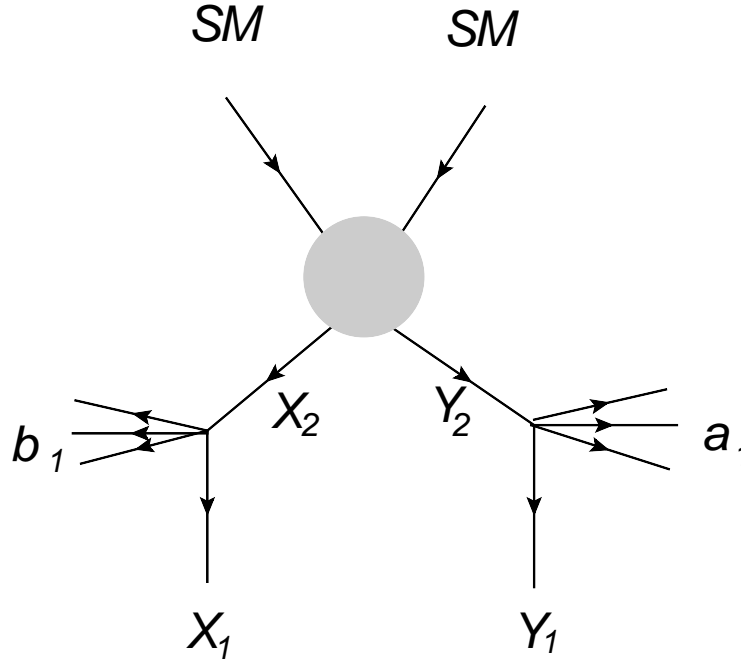


Figure 2.3: A dual cascade chain with prompt Standard Model particle decays. If the visible SM particle decays promptly and if all of its decay products are visible, then the trajectories of its decay products may be traced back to the displaced vertex.

### 2.4.2 Measurable Displaced Tracks

If  $a_1$  and  $b_1$  are stable and hit the detector, then  $p_{a_1}$  and  $p_{b_1}$  can be directly measured. In this scenario, the exact location of the secondary vertices cannot be measured but one can constrain their location to points along the displaced tracks of particles  $a_1$  and  $b_1$ . Parameterizing the 3-momentum  $\vec{p}_{X_1}$  by  $z_X$  and  $\vec{p}_{Y_1}$  by  $z_Y$  removes  $2m$  unknown quantities from Eq. [2.4.1] bringing the requirement for total kinematic recovery down to  $2m - 2km + k \leq 0$ . Achieving this with  $m = 1$  event requires that  $k \geq 2$  so we will use the fact that  $m_{X_3} = m_{Y_3}$  and  $m_{X_2} = m_{Y_2}$  in order to measure the particle masses. Our canonical example for this scenario, depicted in Figure [2.4], comes from GMSB. Here we consider the case where two partons collide resulting in the pair production of two right-handed squarks. Each squark decays to Bino-like neutralinos  $X_3$  and  $Y_3$ , emitting jets in the process. Each neutralino then decays to right-handed sleptons  $X_2$  and  $Y_2$ , emitting leptons  $a_2$  and  $b_2$  in the process. Finally the right-handed sleptons decay to the LSP gravitinos  $X_1$  and  $Y_1$ , emitting additional leptons  $a_1$  and  $b_1$  in the process. The relevant part of the spectrum is summarized in the following table:

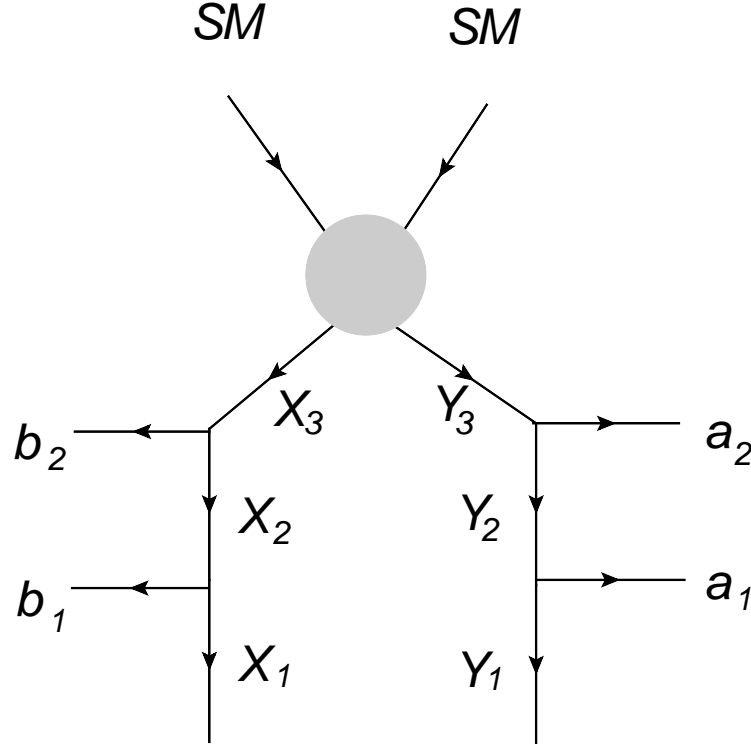


Figure 2.4: A dual cascade chain with two SM “legs”. This is the scenario where  $k = 3$  so the decay chain must have at least two SM legs in order for this technique to be effective.

| Particle             | Symbol        | Mass    |
|----------------------|---------------|---------|
| Bino                 | $\tilde{B}$   | 199 GeV |
| Right-handed Slepton | $\tilde{l}_R$ | 107 GeV |
| Gravitino            | $\tilde{G}$   | 0 GeV   |

Another point to keep in mind is that the further up we go in the decay chain, the higher the chance for combinatoric confusion among the visible particles, labeled in this example by  $a_1, a_2, b_1$  and  $b_2$ . In general it may not always be possible to identify the correct particle with its correct position within a given decay chain. If this is the case then all possibilities should be considered which will result in a larger multiplicity of solutions. A slightly larger data sample may then be required in order to make a definitive mass measurement by finding a common value for the masses. Since the visible SM particles are leptons, we will treat them as effectively massless. The relevant formulae are then given in Eq. [2.4.2] with the expressions for  $c_1$  and  $c_2$  given by Eq. [2.3.5].

$$\begin{aligned}
m_{X_3}^2 &= 2(E_{a_1} + E_{a_2})\sqrt{c_1^2 - (\mathbb{P}_{X_2}^{a_1})^2 + \bar{p}_{a_1}^2} - 2(c_1 + \mathbb{P}_{X_2}^{a_1})(\mathbb{P}_{X_2}^{a_1} + \mathbb{P}_{X_2}^{a_2}) + 2\bar{p}_{a_1}^2 + 2E_{a_1}E_{a_2} \\
m_{Y_3}^2 &= 2(E_{b_1} + E_{b_2})\sqrt{c_2^2 - (\mathbb{P}_{Y_2}^{b_1})^2 + \bar{p}_{b_1}^2} - 2(c_2 + \mathbb{P}_{Y_2}^{b_1})(\mathbb{P}_{Y_2}^{b_1} + \mathbb{P}_{Y_2}^{b_2}) + 2\bar{p}_{b_1}^2 + 2E_{b_1}E_{b_2} \\
m_{X_2}^2 &= 2E_{a_1}\sqrt{c_1^2 + \bar{p}_{a_1}^2 - (\mathbb{P}_{X_2}^{a_1})^2} - 2(\mathbb{P}_{X_2}^{a_1} + c_1)\mathbb{P}_{X_2}^{a_1} + 2\bar{p}_{a_1}^2 \\
m_{Y_2}^2 &= 2E_{b_1}\sqrt{c_2^2 + \bar{p}_{b_1}^2 - (\mathbb{P}_{Y_2}^{b_1})^2} - 2(\mathbb{P}_{Y_2}^{b_1} + c_2)\mathbb{P}_{Y_2}^{b_1} + 2\bar{p}_{b_1}^2
\end{aligned} \tag{2.4.2}$$

In practice, we are using two equations to solve for two unknowns  $m_{X_3}(z_X, z_Y) = m_{Y_3}(z_X, z_Y)$  and  $m_{X_2}(z_X, z_Y) = m_{Y_2}(z_X, z_Y)$ . The calculation of unknown particle masses  $m_{X_2}$  and  $m_{X_3}$  in this scenario is presented here in the table with incorrect and correct solutions separated by columns:

| Event | correct (Bino, Slepton) | wrong (Bino, Slepton)  |
|-------|-------------------------|------------------------|
| 1     | (202, 108)              | (467, 290)             |
| 2     | (199, 107)              | (191, 93)              |
| 3     | (205, 111)              | Null                   |
| 4     | (200, 109)              | (405, 346)             |
| 5     | (200, 108)              | (209, 123), (490, 254) |

Using  $\mathcal{O}(\text{few})$  events we see that the correct solutions can be separated from the incorrect solutions by their sheer multiplicity.

### 2.4.3 Can We Do Better?

It may be argued that the equality of masses following from the condition  $k = 2$  is too specific. Indeed if there was a way to measure the particle mass spectrum without demanding  $m_{X_3} = m_{Y_3}$ , these techniques would gain a lot in generality and become useful in a far wider range of possible new physics scenarios. Thus a natural next step would be to see if it would be possible, under any circumstances, to measure particle masses under the condition  $k = 1$  as depicted in Figure [2.5]. As demonstrated in the previous section, in scenarios with a massless LSP where the trajectories of the displaced tracks are known, the requirement for total kinematic recovery is  $2m - 2km + k \leq 0$ . Solving for  $k$  in terms of  $m$  gives the expression  $k \geq 2m/(2m - 1)$ . Clearly as  $m \rightarrow \infty$ ,  $k \rightarrow 1$  asymptotically but the condition  $k = 1$  cannot be satisfied for any value of  $m$ . Naively this implies that it would not be possible to measure the particle masses given this assumption. Here we present a technique that defies this apparent restriction and demonstrate a particle mass measurement technique using only the condition  $k = 1$ .

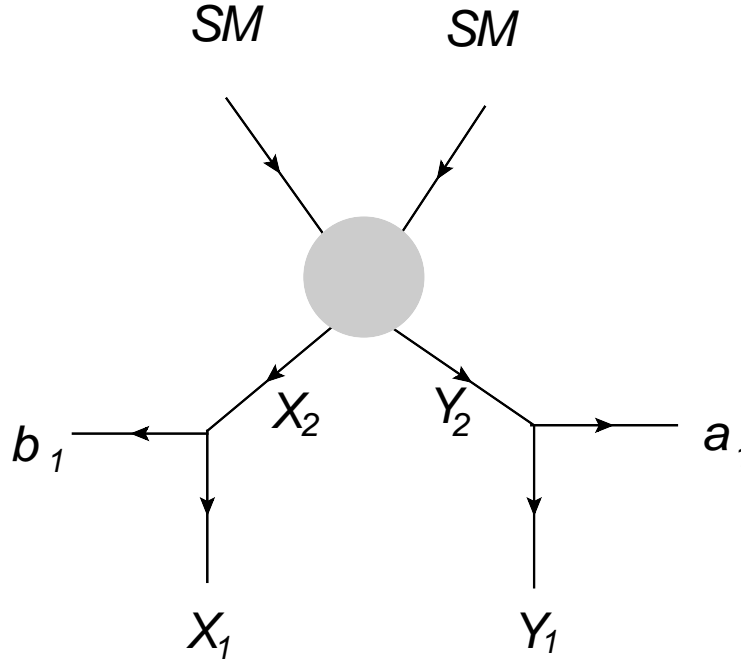


Figure 2.5: A dual cascade chain with one Standard Model “leg”. This is the most general possible scenario with the least amount of specificity. We only require that two equal mass NLSP’s exist in the decay chain.

For situations in which the number of unknown quantities is larger than the number of constraint equations available, there exists a novel and unorthodox method of extracting particle masses using a relatively small number of events. The idea behind this method utilizes the fact

that even in situations where the number of constraints is not large enough to specify a unique solution to all of the unknown quantities, it may be large enough to reduce the space of solutions down to a lower dimensional subspace where the solution may be inferred. Our toy model is taken again from a GMSB scenario. The process under consideration starts with the direct pair production of right-handed sleptons labeled here by  $X_2$  and  $Y_2$ . The sleptons then decay to LSP gravitinos  $X_1$  and  $Y_1$ , emitting a leptons  $a_1$  and  $b_1$  in the process. The relevant part of the mass spectrum is summarized in the following table:

| Particle             | Symbol        | Mass    |
|----------------------|---------------|---------|
| Right-handed Slepton | $\tilde{l}_R$ | 107 GeV |
| Gravitino            | $\tilde{G}$   | 0 GeV   |

The central challenge associated with this example is that there are two unknown quantities  $z_X$  and  $z_Y$  but only one mass constraint equation  $m_{X_2}(z_X, z_Y) = m_{Y_2}(z_X, z_Y)$ , which means that a unique solution cannot be obtained. However, this constraint allows us to express  $z_X$  as a function of  $z_Y$ , which we may then use to write down an expression for the mass of a particle in terms of one variable  $m_{X_2}(z_X)$ . With this one-to-one map from  $z_X$  to  $m_{X_2}$ , the space of possible solutions has been reduced to a one-dimensional subspace (i.e. a line) and the true value of  $m_{X_2}$  must exist as an element of this subspace.

Recall that all of the unknown quantities could be parameterized by the direction of the NLSP's  $\hat{p}_{X_2}$  and  $\hat{p}_{Y_2}$ . Recall further that the direction of an NLSP is given by the location of its secondary vertex  $\hat{p}_{X_2} = \vec{r}_X/|\vec{r}_X|$ , which is restricted to lie somewhere along the trajectory of the associated displaced track. Recall finally, that a secondary vertex can thus be parameterized by its location along the beam axis  $\vec{r}_X \rightarrow \vec{r}_X(z_X)$ . The powerful observation here is the fact that as the hypothesized location of the displaced vertex along the beam axis approaches infinity ( $z_X \rightarrow \infty$ ), the direction of the NLSP will asymptotically approach some fixed unit vector ( $\hat{p}_{X_2} \rightarrow \hat{p}_{const}$ ). This means that as  $z_X \rightarrow \infty$ , the corresponding value of  $m_{X_2}(z_X)$  will asymptotically approach some fixed number. In other words for the function  $m_{X_2}(z_X)$ , the domain  $z_X \in (-\infty, \infty)$  maps to a closed finite range for  $m_{X_2}$ , and the correct value of  $m_{X_2}$  will always be contained in this range. If we plot the elements of this range in a histogram over a small number of events, the histogram will peak around the correct solution since it is an element of every set and should thus have the highest multiplicity across events.

In principle, the correct values for  $z_X$  and  $z_Y$  can take on any arbitrary value. Since the decay distance of particles has the form of an exponentially decaying function, hypotheses for the location of the displaced vertex that are closer to the primary vertex should carry more

weight than ones that are farther away. In order to attenuate contributions from unlikely vertex locations and increase the efficiency of our analysis, we scan the trajectory of the displaced track and assign a weight to each point accordingly. The weighting function is given by Eq. [2.4.3]

$$f[l] = \frac{e^{-l/l_0}}{g(d_{\perp})} \quad (2.4.3)$$

Here  $l$  is the distance between the point on the displaced track and the primary vertex and  $l_0$  is the characteristic decay length of the NLSP. A more detailed discussion of this can be found in Appendix A. Note that we need as input only the rough order of this decay length which can be derived by looking at the distribution of displaced tracks as described in the Appendix B. The result of this weighted histogram is shown in Figure [2.6]. As we can see, this histogram quickly peaks at the value of the correct slepton mass of 107 GeV.

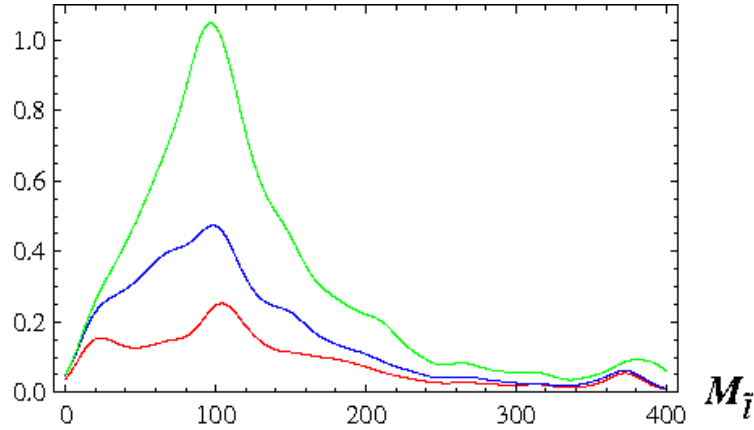


Figure 2.6: Results of the likelihood fit. The red curve indicates an example with 15 events. The blue curve indicates an example with 30 events. The green curve indicates an example with 60 events

## 2.5 Examples with a Massive LSP

Recall again from the introduction, that for  $m$  events and  $k$  constraint equations, the general scenario with a massive LSP resulted in a counting of unknown quantities given by Eq. [2.5.1]. In this section we will study such examples, that typically arise in the supersymmetric context when SUSY is broken at the Planck scale via gravity-mediation. The techniques described in this section will all be a straightforward demonstration of matching constraint equations with unknowns.



$$\text{Number of Unknowns for Massive LSP Scenario} = 6m - 2km + k \quad (2.5.1)$$

### 2.5.1 Measurable Displaced Vertices

Just as it was with the massless LSP, the requirement for measurable displaced vertices is that the final visible SM particles  $a_1$  and  $b_1$  must each decay promptly to two or more visible particles as depicted in Figure [2.3]. The measurement of displaced vertices will again provide us with a complete measurement of the LSP 3-momenta  $\vec{p}_{X_2}$  and  $\vec{p}_{Y_2}$ . The difference is that now the mass of the LSP remains an unknown quantity in the LSP 4-momenta.

In terms of our counting exercise, the measurement of displaced vertices subtracts  $4m$  unknown quantities from Eq. [2.5.1] bringing the total number of unknowns down to  $2m - 2km + k$ . If we are interested in solving for all masses on an event-by-event basis ( $m = 1$ ), the minimum number of constraint equations clearly implies  $k = 2$ . With the LSP's now massive we may take our two constraint equations to be  $m_{X_2} = m_{Y_2}$  and  $m_{X_1} = m_{Y_1}$ . Substituting the second expression into the first reduces the problem to solving one equation for one unknown  $m_{X_2}(m_{X_1}) = m_{Y_2}(m_{X_1})$ . Expressions for the masses are given by Eq. [2.5.2] with solutions for  $c_1$  and  $c_2$  given by Eq. [2.3.5].

$$\begin{aligned} m_{X_2}^2 &= m_{X_1}^2 + m_{a_1}^2 + 2E_{a_1} \sqrt{m_{X_1}^2 + c_1^2 + \vec{p}_{a_1}^2 - (\mathbb{P}_{X_2}^{a_1})^2} - 2(\mathbb{P}_{X_2}^{a_1} + c_1)\mathbb{P}_{X_2}^{a_1} + 2\vec{p}_{a_1}^2 \\ m_{Y_2}^2 &= m_{X_1}^2 + m_{b_1}^2 + 2E_{b_1} \sqrt{m_{X_1}^2 + c_2^2 + \vec{p}_{b_1}^2 - (\mathbb{P}_{Y_2}^{b_1})^2} - 2(\mathbb{P}_{Y_2}^{b_1} + c_2)\mathbb{P}_{Y_2}^{b_1} + 2\vec{p}_{b_1}^2 \end{aligned} \quad (2.5.2)$$

Here we assume that particles  $a_1$  and  $b_1$  are massive, as per our next example where we study a more general GMSB scenario with massive SM particles and a massive gravitino. The process under consideration will be one in which two partons collide to pair produce two right-handed squarks. The squarks then decay to Higgsino-like neutralinos, labeled by  $X_2$  and  $Y_2$ , emitting jets in the process. The neutralinos then decay to a  $Z$  bosons, corresponding to particles  $a_1$  and  $b_1$ , as well as a pair of massive gravitinos  $X_1$  and  $Y_1$  (30). We select events in which each  $Z$  boson decays promptly to two leptons so that the intersection of the lepton tracks gives the location of the displaced vertex. Because of the extreme precision with which the detectors can track leptons, this should be the scenario in which secondary vertices may be located with the highest degree of precision. The spectrum for our toy model is given by the following table:

| Particle  | Symbol      | Mass    |
|-----------|-------------|---------|
| Higgsino  | $\tilde{H}$ | 196 GeV |
| Gravitino | $\tilde{G}$ | 50 GeV  |

Although the constraint equation  $m_{X_2}^2 = m_{Y_2}^2$  is highly non-linear and may have multiple solutions, it can be solved relatively easily using numerical techniques. Unfortunately, the existence of multiple solutions may necessitate a larger data sample in order to perform a confident mass measurement. Once the equation has been solved, a numerical value for  $m_{X_1}$  can be extracted and used to solve for the exact value of  $m_{X_2}$ . Here we show a table of the solutions from 5 events with correct and erroneous solutions separated by columns:

| Event | correct (Gravitino, Higgsino) | wrong (Gravitino, Higgsino) |
|-------|-------------------------------|-----------------------------|
| 1     | (50, 196)                     | Null                        |
| 2     | (50, 196)                     | Null                        |
| 3     | (50, 196)                     | (120, 287)                  |
| 4     | (50, 196)                     | (24145, 24349)              |
| 5     | (50, 196)                     | Null                        |

Here we see that in this case, gravitino and slepton masses are determined precisely. Though some events evidently contain multiple solutions, the unphysical solutions are sufficiently dispersed about the parameter space so as not to cause confusion in the presence of multiple events when a unique common value can easily be determined by eye.

### 2.5.2 Measurable Displaced Tracks

The situation is more challenging if particles  $a_1$  and  $b_1$  are stable as in Figure [2.4]. If this is the case, then displaced vertices will not be measurable and only the trajectories of the displaced tracks may be observed. This will allow us to subtract only  $2m$  from Eq. [2.5.1], reducing the condition for total kinematic recovery to  $4m - 2km + k \leq 0$ . Solving for  $k$  in terms of  $m$  gives  $k = 4m/(2m - 1)$  so as  $m \rightarrow \infty$  we see that  $k \rightarrow 2$ . Thus the minimum number of constraint equations we can demand is  $k = 3$ , which can be solved using two  $m = 2$  events. The constraints  $m_{X_1} = m_{Y_1}$  and  $m_{X_2} = m_{Y_2}$  were combined in Eq. [2.5.2], so the one additional constraint we require for  $k = 3$  is the condition  $m_{X_3} = m_{Y_3}$ . The equations for these masses are given in Eq. [2.5.3]

$$m_{X_3}^2 = m_{X_1}^2 + m_{a_1}^2 + 2(E_{a_1} + E_{a_2})\sqrt{m_{X_1}^2 + c_1^2 - (\mathbb{P}_{X_2}^{a_1})^2 + \vec{p}_{a_1}^2}$$

$$\begin{aligned}
& -2(c_1 + \mathbb{P}_{X_2}^{a_1})(\mathbb{P}_{X_2}^{a_1} + \mathbb{P}_{X_2}^{a_2}) + 2\bar{p}_{a_1}^2 + 2E_{a_1}E_{a_2} \\
m_{Y_3}^2 = & m_{Y_1}^2 + m_{b_1}^2 + 2(E_{b_1} + E_{b_2})\sqrt{m_{Y_1}^2 + c_2^2 - (\mathbb{P}_{Y_2}^{b_1})^2 + \bar{p}_{b_1}^2} \\
& -2(c_2 + \mathbb{P}_{Y_2}^{b_1})(\mathbb{P}_{Y_2}^{b_1} + \mathbb{P}_{Y_2}^{b_2}) + 2\bar{p}_{b_1}^2 + 2E_{b_1}E_{b_2}
\end{aligned} \tag{2.5.3}$$

These equations are again calculated assuming massive  $a_1$  and  $b_1$  as per our example, though the assumption of massless particles  $a_2$  and  $b_2$  is still taken for simplicity. It should be noted however, that all equations generalize easily to arbitrary massive SM particles. From the above equations we see that it is possible to construct expressions for  $m_{X_2}$ ,  $m_{Y_2}$ ,  $m_{X_3}$  and  $m_{Y_3}$  in terms of three unknown quantities  $z_X$ ,  $z_Y$  and  $m_{X_1}$ . For each event we have two constraint equations  $m_{X_1} = m_{Y_1}$  and  $m_{X_2} = m_{Y_2}$  with which to solve them. First notice that since the LSP 4-momenta can be calculated in terms of  $z_X$ ,  $z_Y$  and  $m_{X_1}$ , we can explicitly express  $m_{X_2}$  and  $m_{X_3}$  in terms of these variables. This means that we can apply a change of variables and parameterize the three unknown quantities instead as  $m_{X_1}$ ,  $m_{X_2}$  and  $m_{X_3}$ . The fact that there are two constraint equations means that the solution for each event is a curve in parameter space, which in this case is just  $\mathbb{R}^3$  with axes labeled  $(m_{X_1}, m_{X_2}, m_{X_3})$ . Since the trajectories of the displaced tracks are unique for each event, curves generated by different events will be unique but will always traverse the correct answer. Thus in principle, the correct value for the masses will exist at the intersection of the curves, which is clearly equivalent to the condition of matching particle masses from different events.

Put another way, every hypothesis for the value of  $m_{X_1}$  is equivalent to a hypothesis for the values of  $z_X$  and  $z_Y$ . It is thus also equivalent to a hypothesis for the values of  $m_{X_2}$  and  $m_{X_3}$ . By considering a range of hypotheses for  $m_{X_1}$  over a few events, the correct values of  $m_{X_2}$  and  $m_{X_3}$  will be the unique intersection of all hypotheses. A demonstration of this scenario has been performed with the following mass spectrum (the Bino and Slepton masses are the same as before but the Gravitino mass is now set to 50 GeV):

| Particle             | Symbol        | Mass    |
|----------------------|---------------|---------|
| Bino                 | $\tilde{B}$   | 199 GeV |
| Right-handed Slepton | $\tilde{l}_R$ | 107 GeV |
| Gravitino            | $\tilde{G}$   | 50 GeV  |

As explained, the parameter space for this scenario is  $\mathbb{R}^3$  with axes labeled  $(m_{\tilde{B}}, m_{\tilde{l}}, m_{\tilde{G}})$ . Analyzing three events, we scan values of the gravitino mass from 0 to 100 GeV. As expected, this scan produces a curve in parameter space for each event with the correct answer lying at the intersection of the curves as shown in Figure [2.7]. For reasons given earlier, in practice we

do not expect an exact intersection, but rather a localized region in parameter space where the density of such lines achieves a maximum. The optimal method of mass extraction should then involve searching for the slice in the  $m_{\tilde{G}}$  plane where the density of solutions for  $m_{\tilde{B}}$  and  $m_{\tilde{L}}$  achieves a maximum. To this end we compute a probability sum on each slice of equal  $m_{\tilde{G}}$  using the Gaussian distribution in Eq. [2.5.4] as our probability distribution function with  $\sigma = 10$  GeV.

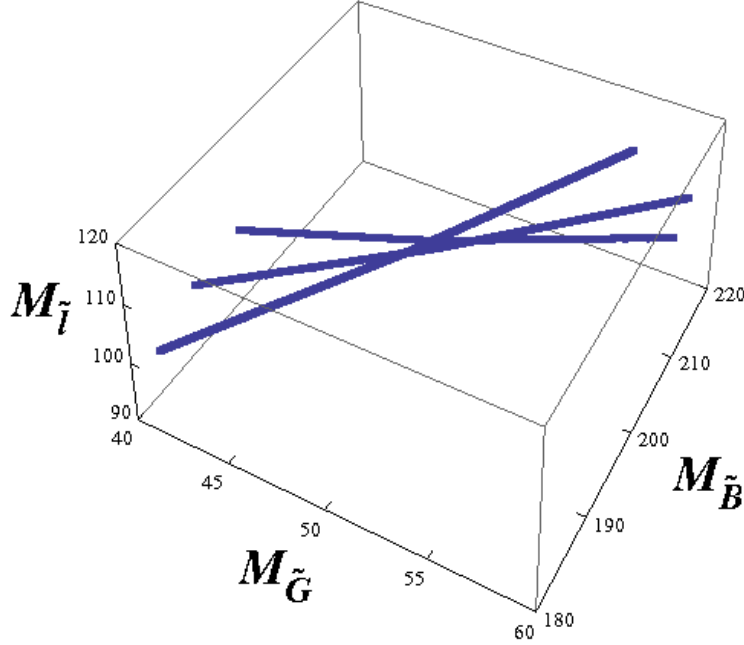


Figure 2.7: With three unknowns ( $m_{\tilde{B}}$ ,  $m_{\tilde{L}}$ ,  $m_{\tilde{G}}$ ) and two equations, the solutions are curves in three dimensional Euclidean space. The intersection of solutions should occur at the correct value of the masses as can be seen in this plot using 3 events as an example.

$$F[m_{\tilde{B},0}, m_{\tilde{L},0}] = \frac{1}{(2\pi\sigma)^2} \sum_i \exp\left(-\frac{(m_{\tilde{B},i} - m_{\tilde{B},0})^2 + (m_{\tilde{L},i} - m_{\tilde{L},0})^2}{2\sigma^2}\right) \quad (2.5.4)$$

Slices of equal  $m_{\tilde{G}}$  give a plane parameterized by  $m_{\tilde{B}}$  and  $m_{\tilde{L}}$ . The function in Eq. [2.5.4] is defined at each point on this plane ( $m_{\tilde{B},0}$ ,  $m_{\tilde{L},0}$ ) and the sum over  $i$  takes a contribution from each data point ( $m_{\tilde{B},i}$ ,  $m_{\tilde{L},i}$ ), which is just given by the intersection of each line with the equal  $m_{\tilde{G}}$  slice. Therefore, Eq. [2.5.4] should be maximized at the point in the plane with the highest density of solutions. Furthermore, the maximum height in each plane should achieve its largest absolute magnitude on the slice corresponding to the correct value of  $m_{\tilde{G}}$ , since it is on this plane that the highest density of solutions resides. Using a sample of 25 events, the probability sum on the correct  $m_{\tilde{G}}$  slice is depicted in Figure [2.8] and we can observe a clear

maximum at the correct solution for  $m_{\tilde{B}}$  and  $m_{\tilde{t}}$ . The maximum height for each  $m_{\tilde{G}}$  is then plotted as a function of the  $m_{\tilde{G}}$  in Figure [2.9]. As expected, the largest absolute magnitude for the probability sum is achieved at the correct value of  $m_{\tilde{G}} = 50$  GeV.

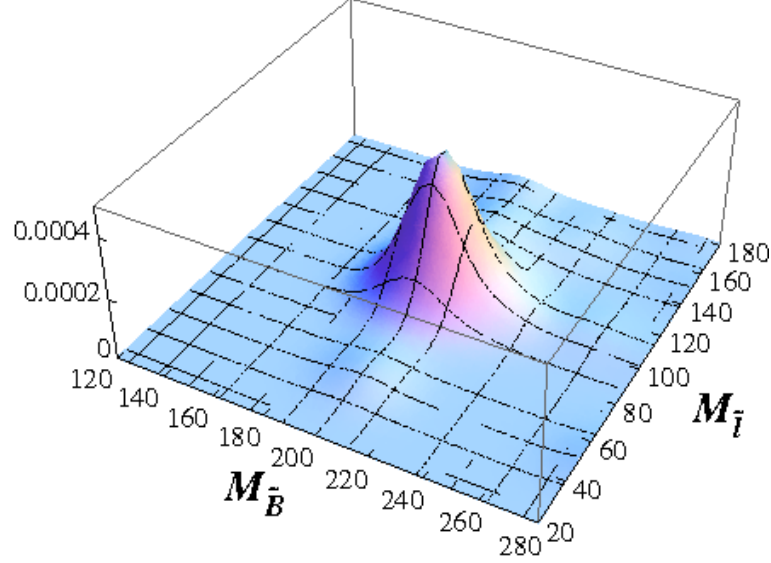


Figure 2.8: The probability sum on the  $m_{\tilde{G}} = 50$  GeV slice. We see that it peaks at the correct value of  $m_{\tilde{B}}$  and  $m_{\tilde{t}}$

### 2.5.3 Can We Do Better?

As we saw in the previous section, as the number of events  $m \rightarrow \infty$ , the minimum number of constraint equations needed  $k \rightarrow 2$ . Thus naively it would seem impossible to solve for all particle masses using the condition  $k = 2$ , with a topology given in Figure [2.5]. Previously we saw that it was still possible to measure the masses in situations where the unknown quantities outnumbered the constraints, using a very small number of events, by employing the trick of section 4.3. It is thus sensible to ask the question of whether or not it would be possible to perform an analogous measurement on cascade decays with a massive LSP. The spectrum used for this example was as follows:

| Particle             | Symbol        | Mass    |
|----------------------|---------------|---------|
| Right-handed Slepton | $\tilde{l}_R$ | 107 GeV |
| Gravitino            | $\tilde{G}$   | 50 GeV  |

As usual, with a massive LSP we have 4 unknowns which we may take to be  $z_X$ ,  $z_Y$ ,  $m_{X_1}$  and  $m_{Y_1}$ . Since we are assuming  $k = 2$ , the available kinematic equations can only remove

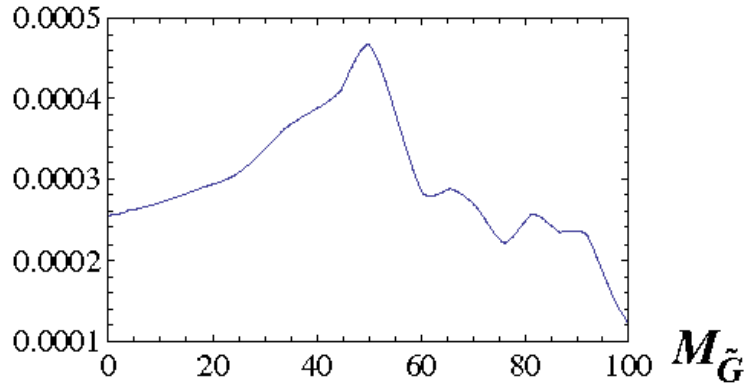


Figure 2.9: A plot of the absolute height of the probability sum as a function of  $m_{\tilde{G}}$ . We see that it peaks at the correct value.

two unknowns. In analogy with the massless LSP scenario, we choose to eliminate the two LSP masses and can derive an expression for the mass of the NLSP  $m_{X_2} \rightarrow m_{X_2}(z_X, z_Y)$ . We now scan all possible values for  $m_{\tilde{G}}$  and play the same trick that was used in the previous section, but in one higher dimension. The result is depicted in Figure [2.10]. Unfortunately, this “probability-double-sum” produces a ridge-like structure rather than a peak at the correct solution. This result implies that these techniques cannot be used to extract a unique solution for  $m_{\tilde{G}}$  when it is non-zero, and can only be used to provide a relation between two mass parameters.

## 2.6 Conclusions

In this paper we studied scenarios in which heavy new particle states were pair produced and cascaded down to some non-interacting stable particle states generating visible SM particles along the way. Here we assumed the decay length of the last decay was measurable, which resulted in a signature of displaced vertices or tracks. We finally assumed that the LSP’s were the only particles that contributed to the transverse missing momentum. Given these assumptions, we described a number of novel techniques for extracting the spectrum of the intermediary particles in the cascade decay that were effective even in the low statistics limit. They would therefore be useful for very early discovery level searches at the LHC.

It should be obvious by now that although this procedure is completely model independent, it was inspired by the phenomenology of supersymmetric models. For any supersymmetric theory on which these methods may be applied, the following conditions must hold:

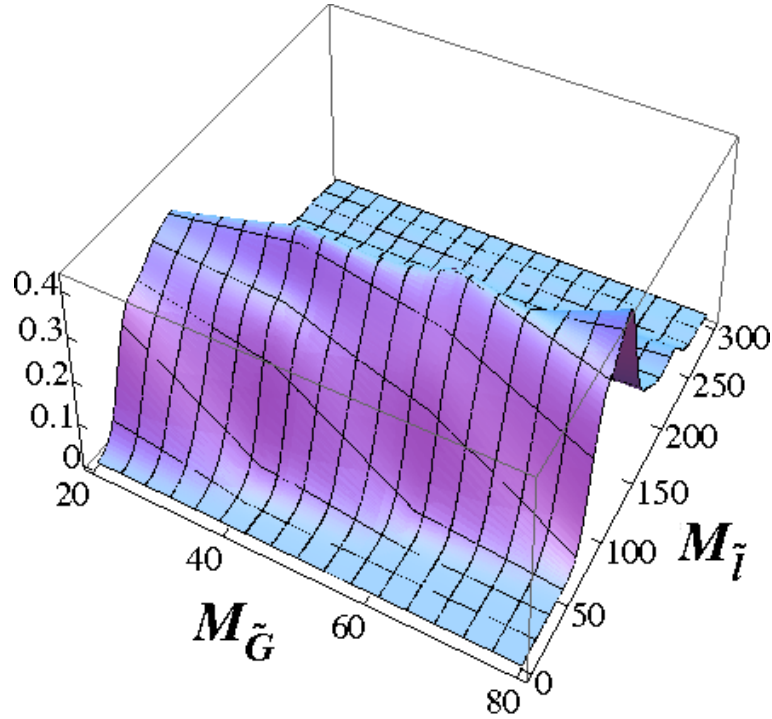


Figure 2.10: The probability double sum for the massive LSP case where unknowns outnumber constraints. The ridge-like structure suggests that no unique solutions exists for the correct value of  $m_{\tilde{G}}$  using this technique

1. R-parity must be (approximately) preserved guaranteeing the stability of the LSP
2. Decays to the LSP must occur before the cascade reaches the detector
3. The 4-momentum of the NLSP must be traceable back to the primary vertex
4. The LSP's must be the sole source of missing transverse momentum
5. The decay length of the NLSP must be finite and measurable

The first four assumptions are very generic for SUSY models though the fifth assumption is rather specific. Despite this fact it can be generically realized in many models, providing us with additional handles on the kinematics of these events. In our paper, we focus on the scenario in which the final step of decay happens at a reasonable finite distance but before the NLSP hits the detector. In scenarios with gauge-mediated SUSY breaking, the decay length of the NLSP is directly related to NLSP mass and the SUSY breaking scale via the relation  $(c\tau)_{NLSP} \sim (\sqrt{F})^4/m_{X_2}^5$ . Since all of the techniques presented in this paper also provide a direct measurement of the decay length of the NLSP, if SUSY is realized in nature they could also be used to extract a very early measurement of the SUSY-breaking scale.

Recently there has been a lot of talk about optimizing search strategies for very early discovery level analyses at the LHC. A central theme in these discussions has been the idea of “searching under the lamp post”. The principle behind this theme is that at the very early stages of a new physics search, especially when data is sparse and statistics are low, it may be a better strategy to search for that which is easiest to see rather than that which you think is most likely to be true. If new physics manifests itself through the presence of missing energy and dual displaced tracks, with  $\mathcal{O}(few)$  events these techniques provide the possibility of

1. Providing convincing evidence for the existence of dual cascade decay topologies
2. Measuring the masses of all new particle states participating in the cascade decay
3. Constructing accurate distributions illuminating the spin-structure of the particles
4. Calculating the SUSY breaking scale if nature is supersymmetric

Clearly the methods described in this paper allow for a very large return from a very small investment. In particular, they allow one to extract an enormous amount of information from signatures that would otherwise be left to very late post-discovery analyses to elucidate completely. As such, they present an extremely bright lamp post under which to search in the coming months.

## 2.7 Appendix A

Here we give some details about how to prepare the MC information and how we derive the weighting factor.

We first took the lhe file from a fixed SUSY spectrum, where the 4-momenta of gravitino, slepton and lepton are accessible. The information of the beginning and ending points of displaced tracks are missing. We take the proper decay length of slepton to be half of detector radius and impose the location of 2nd vertex according to the exponential decay distribution. With all those information, we can calculate the beginning and ending points of displaced tracks for each event. Since displaced tracks are assumed to be measurable in experiments, but 4-momenta of gravitino and slepton are not, we would use the track information and forget the momenta information for the later analysis. Also, the transverse missing energy is assumed to be only coming from two gravitinos, thus it can be calculated when we prepare the MC information. One needs to be very careful on what information is accessible and what is not. We summarize the accessible information as following: the location of primary vertex, the



beginning and ending points of the two displaced tracks for each event, the 4-momenta of each displaced track, and transverse missing energy. Except for those, all other information will be treated as inaccessible.

After we finish the preparation of MC information, we proceed the scanning in possible location of 2nd vertex along one of the displaced tracks. The scanning we do is taking a constant step along the track. The calculation of weighting factor for each scanning point is a little tricky, because part of the information of exponential decay has already been included in the distribution of displaced tracks. Thus the uniform step of scanning along each tracks in many events is not giving us a uniform distribution of points in space. To gain the correct weighting factor, one has to first include a weighting factor of each displaced track. This factor is described more precisely in the following Appendix, then an exponential decay factor can be applied. Thus the weighting factor for each point takes the form in Eq. [2.4.3]

## 2.8 Appendix B

Here we give a detailed discussion on how to extract a rough estimate of the decay length from the observation of a few displaced tracks. This can be done by looking at the distribution of perpendicular distances from the primary vertex to the point of closest approach for all displaced tracks  $d_{\perp}$ . Suppose  $X_2$  travels a distance  $l$  before decaying, as in Figure [2.11]. Let  $\theta$  be the angle between PS and CS. Then we have

$$d_{\perp} = l \sin \theta$$

Let  $l_0$  be the characteristic decay length of particle  $X_2$ . Since the measured decay distance for an event  $l$  must an exponentially decaying distribution, the properly normalized probability distribution is:

$$\frac{\partial P(l, \theta, \phi)}{\partial l} \Big|_{\theta, \phi} = \frac{1}{l_0} e^{-l/l_0} F(\theta, \phi)$$

Also, we know that the decay of particle  $X_2$  is isotropic in its rest frame. Since the mass of  $X_2$  is  $O(100 GeV)$ , the boost from lab frame to the rest frame of  $X_2$  is not large. We can thus approximate the angular distribution in lab frame to be isotropic:

$$\frac{\partial^2 P(l, \theta, \phi)}{\partial(\cos \theta) \partial \phi} \Big|_l = \frac{1}{4\pi} G(l)$$

Since  $l$ ,  $\theta$  and  $\phi$  are independent variables, we :

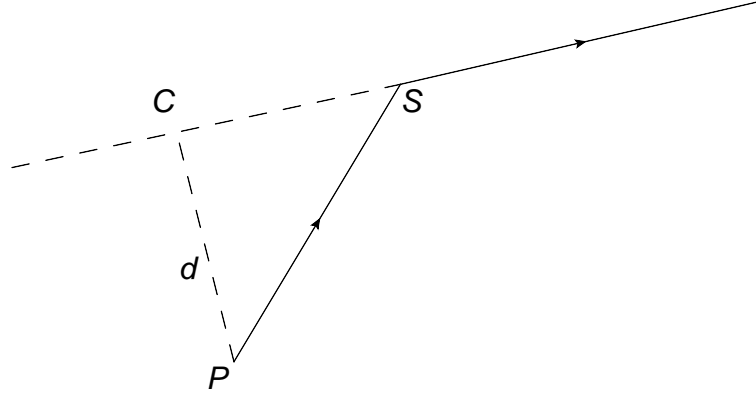


Figure 2.11: The kinematics of a displaced track. Here  $d$  is distance of closest approach between the primary vertex and the displaced track,  $C$  is the point of closest approach,  $l$  is the distance between the primary vertex and the hypothetical point of decay on the displaced track and  $l_0$  is the characteristic decay length of the NLSP.

$$\frac{\partial^3 P(l, \theta, \phi)}{\partial l \partial (\cos \theta) \partial \phi} = \frac{1}{4\pi l_0} e^{-l/l_0}$$

From the relation between  $d_\perp$  and  $(l, \theta)$ , we have

$$\frac{\partial d_\perp}{\partial (\cos \theta)}|_l = -l \sqrt{\frac{l^2}{d_\perp^2} - 1}$$

Finally, we get

$$g(d_\perp) = \frac{dP}{d(d_\perp)} = \int_{d_\perp}^{\infty} \frac{dl}{2l_0} \frac{d_\perp e^{-l/l_0}}{l \sqrt{l^2 - d_\perp^2}}$$

Though this integral is not easy to solve, one can cut the integral at very large values and get the distribution numerically. Thus, with just a couple of displaced tracks from a few events, one can extract the rough value of the decay length of  $X_2$ .

## Bibliography

- [1] I. Hinchliffe, F. E. Paige, M. D. Shapiro, J. Soderqvist and W. Yao, Phys. Rev. D **55**, 5520 (1997) [arXiv:hep-ph/9610544].
- [2] C. G. Lester and D. J. Summers, Phys. Lett. B **463**, 99 (1999) [arXiv:hep-ph/9906349].
- [3] A. Barr, C. Lester and P. Stephens, J. Phys. G **29**, 2343 (2003) [arXiv:hep-ph/0304226].
- [4] D. R. Tovey, JHEP **0804**, 034 (2008). [arXiv:0802.2879 [hep-ph]].
- [5] K. T. Matchev, M. Park, [arXiv:0910.1584 [hep-ph]].
- [6] P. Konar, K. Kong, K. T. Matchev *et al.*, [arXiv:1006.0653 [hep-ph]].
- [7] K. Kawagoe, T. Kobayashi, M. M. Nojiri *et al.*, Phys. Rev. **D69**, 035003 (2004). [hep-ph/0309031].
- [8] P. Meade, M. Reece and D. Shih, JHEP **1010**, 067 (2010) [arXiv:1006.4575 [hep-ph]].
- [9] I. -W. Kim, Phys. Rev. Lett. **104**, 081601 (2010). [arXiv:0910.1149 [hep-ph]].
- [10] H. Bachacou, I. Hinchliffe and F. E. Paige, Phys. Rev. D **62**, 015009 (2000) [arXiv:hep-ph/9907518].
- [11] M. G. Jackson, JHEP **0109**, 004 (2001) [arXiv:hep-th/0103217].
- [12] L. Covi, H. B. Kim, J. E. Kim and L. Roszkowski, JHEP **0105**, 033 (2001) [arXiv:hep-ph/0101009].
- [13] B. C. Allanach, C. G. Lester, M. A. Parker and B. R. Webber, “Measuring sparticle masses in non-universal string inspired models at the JHEP **0009**, 004 (2000) [arXiv:hep-ph/0007009].
- [14] B. K. Gjelsten, D. J. . Miller and P. Osland, JHEP **0412**, 003 (2004) [arXiv:hep-ph/0410303].
- [15] K. Kawagoe, M. M. Nojiri and G. Polesello, Phys. Rev. D **71**, 035008 (2005) [arXiv:hep-ph/0410160].

- [16] C. G. Lester, M. A. Parker and M. J. . White, “Determining SUSY model parameters and masses at the LHC using JHEP **0601**, 080 (2006) [arXiv:hep-ph/0508143].
- [17] N. Arkani-Hamed, G. L. Kane, J. Thaler and L. T. Wang, JHEP **0608**, 070 (2006) [arXiv:hep-ph/0512190].
- [18] M. Baumgart, T. Hartman, C. Kilic *et al.*, JHEP **0711**, 084 (2007). [hep-ph/0608172].
- [19] J. M. Butterworth, J. R. Ellis and A. R. Raklev, JHEP **0705**, 033 (2007) [arXiv:hep-ph/0702150].
- [20] H. -C. Cheng, J. F. Gunion, Z. Han *et al.*, JHEP **0712**, 076 (2007). [arXiv:0707.0030 [hep-ph]].
- [21] M. M. Nojiri, G. Polesello, D. R. Tovey, JHEP **0805**, 014 (2008). [arXiv:0712.2718 [hep-ph]].
- [22] R. Horsky, M. Kramer, 1, A. Muck *et al.*, Phys. Rev. **D78**, 035004 (2008). [arXiv:0803.2603 [hep-ph]].
- [23] A. J. Barr, C. Gwenlan, Phys. Rev. **D80**, 074007 (2009). [arXiv:0907.2713 [hep-ph]].
- [24] T. Cohen, E. Kuflik, K. M. Zurek, JHEP **1011**, 008 (2010). [arXiv:1003.2204 [hep-ph]].
- [25] M. Park and S. Thomas, “Extracting Particle Masses from Missing Energy Signatures Without Using Missing Energy,” to appear.
- [26] A. J. Barr and C. G. Lester, J. Phys. G **37**, 123001 (2010) [arXiv:1004.2732 [hep-ph]].
- [27] H. C. Cheng, D. Engelhardt, J. F. Gunion, Z. Han and B. McElrath, Phys. Rev. Lett. **100**, 252001 (2008) [arXiv:0802.4290 [hep-ph]].
- [28] H. -C. Cheng, J. F. Gunion, Z. Han *et al.*, Phys. Rev. **D80**, 035020 (2009). [arXiv:0905.1344 [hep-ph]].
- [29] B. Webber, JHEP **0909**, 124 (2009). [arXiv:0907.5307 [hep-ph]].
- [30] P. Meade, M. Reece, D. Shih, JHEP **1005**, 105 (2010). [arXiv:0911.4130 [hep-]

## Chapter 3

# Diagnosing the Top-quark Angular Asymmetry Using LHC Intrinsic Charge Asymmetries

### 3.1 Introduction

The most peculiar among the Standard Model fermions, the top quark has challenged the high energy physics community, both on the experimental and theoretical level, since its discovery in 1995. From the theoretical viewpoint, its exceptional mass suggests that it might play a special role in the mechanism of electroweak symmetry breaking. This occurs in a number of proposed theories, including Little Higgs and Top-color Assisted Technicolor, and even within many supersymmetric models. On the experimental side, the predictions of the Standard Model (SM) for the top quark are still not fully tested. At the Tevatron, the high production threshold limited the number of  $t\bar{t}$  events, and only now at the LHC will it be possible to perform precision measurements of the top quark's properties.

While most aspects of the top quark agree so far with SM predictions, both the CDF (1; 3) and D0 (2; 4) collaborations have reported an anomalous forward-backward asymmetry for  $t\bar{t}$  pairs at intermediate to high invariant mass, much larger than expected from SM calculations (5; 6; 7; 8; 9; 10). This result, which relies upon “forward” being defined relative to the Tevatron's proton beam, cannot be immediately checked at a proton-proton collider such as the LHC. However, it is well-known that forward-backward asymmetries at a proton-antiproton machine lead to differential charge asymmetries at a proton-proton machine, and indeed, a differential charge asymmetry in  $t\bar{t}$  production, as a function of the  $t$  quark's rapidity, should be observable. This quantity has been discussed by theorists, for instance in (15; 16; 17; 18; 54; 76), and has been measured at the LHC experiments (12; 13; 14). The statistical errors on this measurement are still rather large, however, and meanwhile the LHC's higher energy allows its experiments to probe for related phenomena in other ways.

No significant problems with the SM calculation or the experimental measurements of the anomalously large asymmetry have been found. Meanwhile, a variety of models have been proposed to explain it. Most of these produce the asymmetry through the exchange of a

new particle, either an  $s$ -channel mediator with axial couplings to both top and light quarks (19; 20; 21; 22; 23; 24; 25; 26; 27; 28; 29; 30; 31; 32; 34; 33; 35; 36; 37; 38; 39), or a  $t$ -channel (or  $u$ -channel) mediator (40; 41; 42; 43; 44; 45; 46; 47; 48; 49; 50; 51; 52; 53; 54; 55; 56; 57; 58; 59) with flavor-violating couplings that convert a light quark or antiquark to a top quark. Both processes are illustrated in Fig. 3.1. In (60; 61; 62; 63; 64; 65; 66; 67; 68; 69; 70; 71), comparisons between different models are carried out, and study of those models or measurements in the LHC context can be found in (72; 74; 73; 75; 76; 77; 78; 79; 80; 81; 82; 83; 84).

Charge asymmetries at the LHC are known to be powerful tools for searching for and studying new physics, and recently this has been put to use in the context of models for the  $t\bar{t}$  asymmetry. In (52) a large overall charge asymmetry was used to argue the Shelton-Zurek model (48) was most likely excluded; a similar method was then applied for a different model in (85). Here, we focus on models with  $t$ - or  $u$ -channel mediators, which, as we will see, often generate large charge asymmetries in  $t\bar{t}j$  (top plus antitop plus a jet) at the LHC. These asymmetries, a smoking gun of this type of model, will be crucial for a convincing discovery or exclusion of this class of models. Note these asymmetries are *not* directly related to the Tevatron forward-backward asymmetry in  $t\bar{t}$  events, which translate at the LHC into the differential charge asymmetry in  $t$  production mentioned above. The asymmetry in  $t\bar{t}j$  that we study here stems from a completely different source; see below.

Any of the models with a  $t$ - or  $u$ -channel mediator has a coupling between a light quark or antiquark, a top quark, and a new particle  $X$ , as in Fig. 3.1(b). It follows that the  $X$  can be produced from an off-shell quark or antiquark in association with a  $t$  or  $\bar{t}$ , as shown in Fig. 3.2. Consequently, as has been pointed out by many authors (42; 44; 47; 72; 68; 81), it is important at the LHC to look for the process  $pp \rightarrow Xt$  (and the conjugate process  $pp \rightarrow \bar{X}\bar{t}$ ), where  $X$  in turn decays to  $\bar{t}$  plus a jet. A straightforward search for a  $t$ +jet resonance can be carried out, though it suffers from the poor resolution for reconstructing the resonance, large intrinsic backgrounds whose shape may peak near the resonance mass, and combinatoric backgrounds in the reconstruction. Alternatively, one could attempt a cut-and-count experiment; with appropriate cuts one can obtain samples in which the  $X$  production contributes a statistically significant excess to the  $t\bar{t}j$  rate. But the  $t\bar{t}j$  background is not simple to model or measure, and systematic errors may be problematic.

Fortunately, the process shown in Fig. 3.2 has a large charge asymmetry. The difference between quark and antiquark pdfs assures that the rate for  $X$  production is different from that of  $\bar{X}$  production. (If  $X$  is self-conjugate, same-sign top-quark production results, and is readily excluded (90; 89); we therefore assume that  $\bar{X} \neq X$ .) Our approach in this work will be to

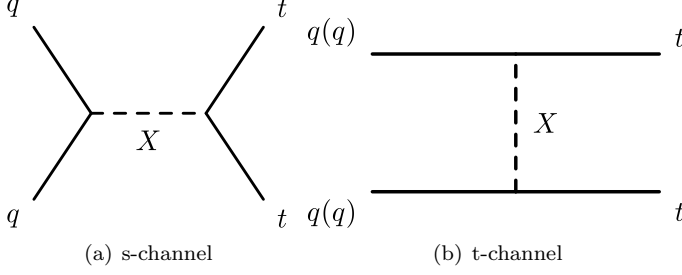


Figure 3.1: Diagrams that can lead to a forward-backward asymmetry at the Tevatron in  $t\bar{t}$  production. The  $X$  is exchanged either (not both) in the  $s$ - or  $t$ -/ $u$ -channel.  $q$  may be  $u$  or  $d$ .

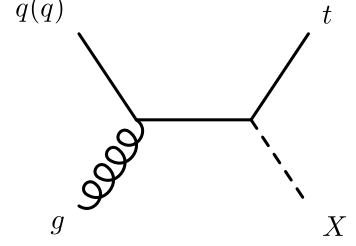


Figure 3.2: For a  $t$ - or  $u$ -channel mediator  $X$ , direct production of  $tX$  (followed by  $X \rightarrow \bar{t} + q$  or  $\bar{q}$ ) is always possible.

suggest something a bit more sophisticated than a simple resonance search, using the charge asymmetries of these models to reduce systematic errors at a limited price in statistics. We will also propose other charge-asymmetric variables that can serve as a cross-check. As a by-product, should any discovery occur, the asymmetry itself can serve as a diagnostic to distinguish certain classes of models from one other.

### 3.2 Benchmark Models

As our benchmark model, we take a typical model with a  $t$ -channel mediator, a colorless charged spin-one particle which we call a  $W'$ . We will assume the  $W'$  couples a right-handed  $d$  quark to a  $t$  quark. While a theory with only these couplings would be inconsistent, we will assume this coupling generates the largest observable effects. One may say that we choose a “simplified model”, or “model fragment”, in which this coupling is the only one that plays an experimentally relevant role. We will see this point is not generally essential.<sup>1</sup> The Lagrangian we take for our simplified model is simply

$$\mathcal{L} = -g_R W'_\mu{}^+ \bar{t} \gamma^\mu P_R d + h.c. \quad (3.2.1)$$

where  $P_R = (1 + \gamma^5)/2$ .

We are interested in the process in which the  $W'$  contributes to a  $t\bar{t}j$  final state. One contribution comes from  $dg \rightarrow tW'^-$  and its conjugate  $\bar{d}g \rightarrow \bar{t}W'^+$ , following which the  $W'^-$  decays to  $\bar{t}d$  and the  $W'^+$  decays to  $t\bar{d}$ . We will refer to this as “ $s$ -channel production” (see Fig. 3.3). The  $W'$  also contributes to  $dg \rightarrow t\bar{t}d$ , and similar processes, through  $t$ -channel exchange (see Fig. 3.4).

<sup>1</sup>Attempts to make consistent models with a  $W'$  include (88). There are also attempts to include the coupling of a  $W'$  with a  $u$  and  $b$  quark (48), but such couplings lead to a large charge asymmetry in single top production (52), now excluded by LHC data (86; 87).

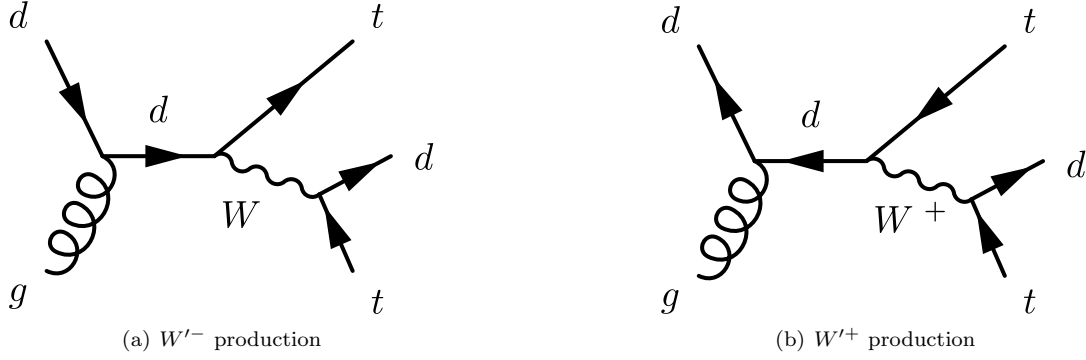


Figure 3.3: Dominant production mode for the  $W'$ . The cross-section for  $W'^-$  is much larger than for  $W'^+$ .

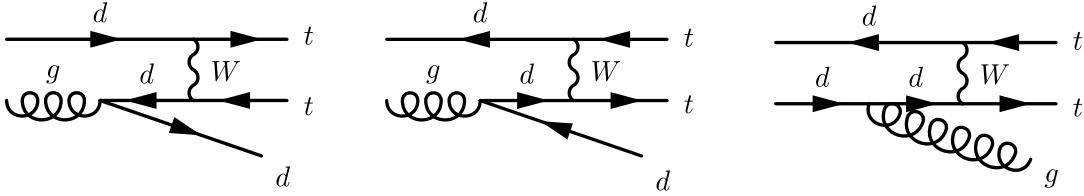


Figure 3.4: Characteristic examples of diagrams that contribute to  $t\bar{t}j$  production involving the  $W'$  in  $t$ -channel exchange.

The cornerstone of our analysis is the observation that *in the  $s$ -channel process, the negatively charged  $W'$  is produced more abundantly than the positively charged  $W'$* , because the negative  $W'$  can be produced from a valence quark, while a positive  $W'$  requires a sea antiquark in the initial state. (See Fig. 3.3.)

The processes in Figs. 3.3 and 3.4 can in principle have non-trivial interference with the Standard Model background — a point which considerably complicates background simulation. But we have found that interference is not numerically important for certain observables, at least with current and near-term integrated luminosities. *All results in this paper therefore ignore interference; however, with larger data sets, or when studying other models and/or using other variables, one must confirm on a case-by-case basis that this approximation is sufficiently accurate for the analysis at hand.*

In (47), the authors studied this model and fitted it to the  $t\bar{t}$  asymmetry and total cross-section in CDF. (This was done prior to the DZero result that shows a smaller asymmetry with less energy dependence.) Based on this work, we will take six benchmark points shown in Table 3.1, with three values of the  $W'$  mass and two values of  $g_R$  for each mass, a larger value that would reproduce the CDF measurement and a value  $\sqrt{2}$  smaller that would give a Tevatron asymmetry (and also an  $W'$  width and  $tW'$  production rate) of about half the size. The cross-sections at these benchmark points (including all the processes shown in Figs. 3.3



| Mass (GeV) | $g_R$                  | cross-section (pb) |
|------------|------------------------|--------------------|
| 400        | 1.5                    | 32.2               |
| 400        | $\frac{1.5}{\sqrt{2}}$ | 12.9               |
| 600        | 2                      | 18.2               |
| 600        | $\sqrt{2}$             | 6.3                |
| 800        | 2                      | 6.5                |
| 800        | $\sqrt{2}$             | 2.1                |

Table 3.1: 7 TeV LHC tree-level cross-sections for the processes shown in Figs. 3.3 and 3.4, for the various benchmark points. No K-factor is included in these numbers, but we do apply one later in our analysis; for a discussion of the simulations and the K-factor, we refer the reader to Sec. 3.4.

and 3.4) are also given in Table 3.1.

The  $W'$  also contributes to  $t\bar{t}$  production through  $t$ -channel exchange, and thus to the differential charge asymmetry in  $t$  rapidity at the LHC (not to be confused with the asymmetries in  $t\bar{t}j$  that are the subject of this paper.) ATLAS and CMS measurements of this quantity (with respectively 0.7 and 1.1 fb<sup>-1</sup> of data) (12; 14) may somewhat disfavor the benchmark points with the larger values of  $g_R$ , which (at parton-level, not accounting for  $t$  reconstruction efficiencies) give a differential charge asymmetry in the 8–9% range. But the situation is ambiguous, since event mis-reconstruction and detector resolution produce a large dilution factor, which may make this charge asymmetry consistent with the current measurements. Our benchmarks with larger couplings thus probably represent the outer edge of what might still be allowed by the data. By considering also an intermediate coupling that still could explain the Tevatron  $t\bar{t}$  asymmetry, we cover most of the interesting territory, and permit the reader to interpolate to other values of the couplings.

### 3.3 A mass variable

Among the charge-asymmetric observables discussed in this paper, we will devote most of our attention to one motivated by the resonance structure of the  $W'$ , which we will refer to as the mass variable  $M_{j1bW}$  in later content. This variable is applicable universally to a wide range of  $W'$  masses and couplings, and to most other models with  $tX$  production. We discuss this mass variable in great detail in this section. In Sec. 3.6, we will discuss the azimuthal angle between the hardest jet and the lepton (which we refer to as the “angle variable”.) A third class of potentially useful variables (“ $P_T$  variables”), including the  $P_T$  difference between the hadronic and the leptonic top quarks or  $W$ -bosons, is briefly discussed in Appendix 3.10.

We will consider only the semi-leptonic  $t\bar{t}j$  events (where one top decays hadronically and

the other leptonically), resulting in a final state of 5 jets, a lepton and missing energy. All-hadronic decays are not useful for a charge asymmetry, as  $t$  and  $\bar{t}$  cannot be distinguished in this case, while the fully leptonic decay, though probably useful, has a low branching fraction.

Since it is the  $s$ -channel process in Fig. 3.3, where the  $W'$  appears as a resonance, that is charge-asymmetric, we will focus our attention there. In our later analysis we will impose an  $S_T$  cut<sup>2</sup> to improve the signal-to-background ratio. If we put that cut at 700 GeV, the fraction of negatively charged  $W'$ s for the 400, 600 and 800 GeV  $W'$  is 0.84, 0.87 and 0.86 respectively. Such an enormous charge asymmetry in production can be put to good use.

Note, however, that since every event (following the  $W'$  decay) has a  $t$  and a  $\bar{t}$ , either of which may produce the lepton, *the total numbers of events with positively and negatively charged leptons are expected to be roughly equal*, up to edge effects produced by cuts and detector acceptance. But since negative  $W'$ s are produced more abundantly, *a negatively charged lepton is more likely to come from the  $W'$  decay, while positive leptons tend to originate from the decay of the spectator top quark or antiquark*. Kinematic features, such as the invariant mass and transverse mass of various final-state objects, differ for events with negatively and positively charged leptons. For instance, a simple bump hunt aimed at reconstructing the  $W'$  resonance would find a much larger bump in negatively charged leptons than in positively charged ones. Here, we will consider the  $W'$  reconstructed mass distribution more completely, noting that *the signal remains asymmetric even away from the  $W'$  mass bump*, since the total asymmetry must integrate to (almost) zero.

Another useful kinematical feature is that the hardest jet in  $tW' \rightarrow t\bar{t}d$  production commonly originates from the  $d$ -quark, because of the large energy released in the  $W'$  decay and the dissipation of the top quarks' energies into their three daughters. At leading order and at parton-level, and with an  $S_T$  cut of 700 GeV, the fraction of events where the hardest parton is the  $d$ -quark (or antiquark) from the  $W'$  is 0.71, 0.82 and 0.82 for a  $W'$  of mass 400, 600 and 800 GeV respectively. (Note neither ISR/FSR, hadronization, nor jet reconstruction are accounted for in these numbers, which are for illustration only.) We have designed our variables to maximally exploit these two kinematic features.

One conceptually simple approach to seeking the  $W'$  would involve fully reconstructing the  $t$  and  $\bar{t}$  in each event, and searching for a resonance in either  $tj$  or  $\bar{t}j$ . This has been discussed in (42; 44; 47; 72; 68; 81). The challenge is that the combinatoric background is large and hard to model, and often peaks in a region not far from the resonance. Charge-asymmetries

---

<sup>2</sup>For our definition of  $S_T$ , see equation (3.4.1) in Sec. 3.4.

are useful here, because the positive-charge lepton events are dominated by the combinatoric background, while the negative-charge lepton events have similar combinatorics but a much larger resonance. Comparison of the two samples would allow for the elimination of a significant amount of systematic error.

However, full event reconstruction in events with five jets will have low efficiency, and moreover we are neither confident in our ability to model it nor certain it is the most effective method. Here we will instead focus on variables that require only partial event reconstruction. Of course the experimental groups should explore whether full event reconstruction is preferable to the methods we attempt here.

We will focus on the mass variable  $M_{j1bW}$ : the invariant mass of the hardest jet in the event, a  $b$ -tagged jet (chosen as described below), and a  $W$ -candidate reconstructed from the observed lepton and the missing transverse momentum (MET).<sup>3</sup> It involves only a partial reconstruction of the event to form a candidate for the  $W'$ , assuming it has decayed to a lepton.<sup>4</sup> In signal events where the hardest jet in the event is a  $d$  (or  $\bar{d}$ ) from the  $W'$  decay, and the  $\bar{t}$  (or  $t$ ) from the  $W'$  produces a lepton  $\ell$ ,  $M_{j1bW}$  often reconstructs the  $W'$  resonance. The events with an  $\ell^-$  typically exhibit a resonance at the  $W'$  mass, while those with an  $\ell^+$ , in which the  $W'$  is most often not reconstructed correctly, have a smoother distribution. This effect, and the resulting charge asymmetry — with a negative asymmetry near the  $W'$  mass and positive asymmetry elsewhere — are shown for  $m_{W'} = 600$  GeV in Fig. 3.5. Both the asymmetric  $s$ -channel and the almost symmetric  $t$ -channel are included in what we call “signal.”

In constructing  $M_{j1bW}$ , we reduce the combinatorial background by rejecting  $b$ -jets that are inconsistent with forming a top quark with the lepton and the MET ( $M_{bl} < 155$  GeV and  $M_{bl\nu}^T < 175$  GeV.) When multiple  $b$ -jets satisfy these criteria, we select the  $b$ -quark for which the quantity  $|M_{bl} - 155 \text{ GeV}| + |M_{bl\nu}^T - 175 \text{ GeV}|$  is smallest. The combined efficiency of the  $W$  reconstruction and the  $b$  selection is about 45%.

Meanwhile, we will give evidence in Sec. 3.5.1 that the SM background to this process shows no charge asymmetry in this variable, to a sufficiently good approximation. It is crucial for the use of this variable that this is true.

There are other invariant-mass and transverse-mass variables that have their merits. Some

---

<sup>3</sup>We solve for the neutrino four-momentum in the usual way. Complex solutions are discarded for simplicity. When two real solutions exist, the most central  $W$  candidate is selected.

<sup>4</sup>Were one to fully reconstruct the  $t\bar{t}j$  events, one could also study the invariant mass of the *hadronically*-decaying top and the hardest jet, which will also differ for positive- and negative-charge lepton events. We neglect this variable here because the reconstruction of the hadronic top has low efficiency, but we encourage our experimental colleagues to consider if they can increase their sensitivity by including it.

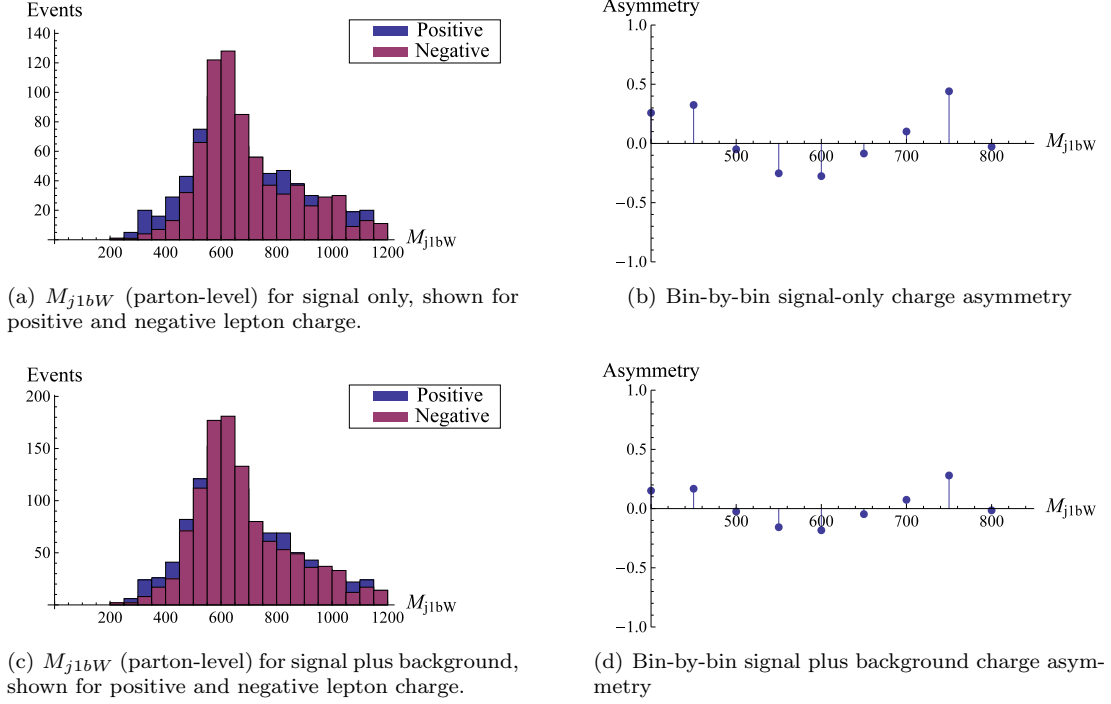


Figure 3.5: Parton-level charge asymmetry in the  $M_{j1bW}$  variable for a 600 GeV  $W'$  with  $g_R = 2$  and an  $S_T$  cut at 700 GeV. The leptonic  $W$  boson was reconstructed from its decay products,  $j_1$  was taken to be the hardest non- $b$  parton. ISR/FSR and  $b$ -quark selection effects were not accounted for here. The sample corresponds to  $1.5 \text{ fb}^{-1}$ .

require no event reconstruction, including the invariant mass of the hardest jet and the lepton ( $M_{j1l}$ ) and the invariant mass of the hardest jet, a  $b$ -tagged jet and the lepton ( $M_{j1bl}$ ). For quantities that include the MET in the event, one could consider the transverse mass of two or more objects. (See also the footnote above concerning the hadronically decaying top in fully reconstructed events.) These variables and their charge asymmetries are strongly correlated, but one might still obtain additional sensitivity by combining them. But here, for simplicity, having found that the most sensitive variable on its own is  $M_{j1bW}$ , we will focus on it exclusively below.

### 3.4 Event selection and processing

We mentioned earlier that the  $t\bar{t}j$  background and the  $W'$  signal do interfere with each other. However we have explicitly checked that interference effects do not alter the differential asymmetry in the  $M_{j1bW}$  mass variable by a significant amount (given currently expected statistical uncertainties). The effect on the total number of events is also small. Thus it is relatively safe for us — and for the early searches at the LHC — to neglect interference in the study of the

mass variable, at least for the  $W'$  model. (We have not studied whether this is true for all similar models with  $tX$  production.) At some point, higher-precision study with much larger data samples ( $\gg 10 \text{ fb}^{-1}$ ) may require the full set of interfering diagrams, and a special-purpose background-plus-signal simulation. Here we simulate background and signal independently.

On the other hand,  $t$ -channel  $W'$  exchange (Fig. 3.4) makes an important contribution to the cross-section and should always be included when generating the signal sample. (This is not uniformly the case in the literature.) For the variables we are studying, the  $t$ -channel process does not contribute much to the asymmetry, and effectively acts as an additional background.

A background sample and the signal samples for our benchmark points were generated with Madgraph 4.4.32 (91) and showered with PYTHIA 6.4.22 (92). We performed a fast detector simulation with DELPHES 1.9 (94). (For our parton-level studies the decays of the top and the antitop were simulated with BRIDGE 2.24 (93)). We used the anti- $k_T$  jet-clustering algorithm (with  $R = 0.5$ ) to reconstruct jets. The isolation of leptons and jets is described in Appendix 3.9.1. The  $b$ -tagging was modeled after the SV050 tagger of the ATLAS collaboration (95). We account for the rising  $P_T$ -dependence of the  $b$ -tagging efficiency, which reaches up to 60% in the kinematic regime of interest. The dependence of the  $b$  tagging efficiency on the pseudo-rapidity is assumed to be negligible within the  $\eta$  reach of the tracker ( $|\eta| < 2.4$ ), with the tagging rate taken to be zero outside the tracker. The  $c$ -tag efficiency was assumed a factor of 5 smaller and the mistag rate is taken to be 1%. We do not account for the falloff in efficiency and the rise in mistag rates at higher  $P_T$ , since measurements of these effects are not publicly available; our tagging might therefore be optimistic, though the issue affects both signal and background efficiency.

We impose the following criteria for our event selection:<sup>5</sup>

- At least 5 jets with  $P_T^{jet} > 30 \text{ GeV}$  and  $|\eta| < 5$
- At least one of these jets is  $b$ -tagged
- One isolated lepton ( $e^\pm$  or  $\mu^\pm$ ) with  $P_T^\ell > 30 \text{ GeV}$  and  $|\eta| < 2.5$
- $\text{MET} > 30 \text{ GeV}$ .

where  $\eta$  stands for pseudo-rapidity as usual. We also impose a cut on  $S_T$ , which is defined as

$$S_T = \sum P_T^{jet} + P_T^\ell + \text{MET} \quad (3.4.1)$$

---

<sup>5</sup>Our cuts may be optimistic in the rapidly changing LHC environment. Raising the jet  $P_T$  cut to 40 GeV results in a loss of sensitivity of order 10–20%. If one restricts jets to those with  $|\eta| < 2.5$ , signal is reduced by about 10%, and background by about 15%. An increase in the electron  $P_T$  cut to 45 GeV reduces signal by 20–25% and background by about 30%.

where the sum runs over all the jets with  $P_T^{jet} > 30$  GeV. The  $S_T$  cut will be at a high enough scale (typically 600-800 GeV) that our events will pass the trigger with high efficiency.

The SM background simulation requires a matched sample for

$$p + p \rightarrow t + \bar{t}$$

$$p + p \rightarrow t + \bar{t} + j$$

where we use the MLM scheme (96), with QCUT= 30 and xqcut= 20. The renormalization and factorization scales are set to  $m_T$ , where  $m_T^2$  is the geometric mean of  $m_t^2 + p_T^2$  for the top and antitop.

One might wonder whether it is necessary to include  $pp \rightarrow t\bar{t}jj$  as well. But we are requiring 5 hard jets, and the mass and angle variables we will study are not sensitive to soft radiated jets, as they involve the hardest jet and a  $b$ -tagged jet. It is sufficient, therefore, for us to truncate our matched sample with one jet, and allow PYTHIA to generate any additional radiation. In total, we generated 3 million background events before matching. After matching, we find an inclusive  $t\bar{t}$  LO cross-section of about 90 pb, so we include a K-factor of 1.7 to match with the NLO+NNLL QCD calculation (97; 98). The number of events we generated for background corresponds to about  $14 \text{ fb}^{-1}$ , large enough to provide smooth distributions for the variables we study.

There are a number of SM processes whose *total cross-sections* for producing a lepton are intrinsically charge-asymmetric. These include single-top production and  $W$ -plus-jets, for which an  $\ell^+$  is more likely than an  $\ell^-$ . However, these have small rates for 5 jets and a lepton, especially with a  $b$  tag required and with a hard  $S_T$  cut. Moreover, asymmetries from any such process would be quite different from the signal, being both structureless and everywhere positive. We foresee no problem with such backgrounds.

For each value of the  $W'$  mass and coupling constant, we generated a signal sample with 750,000 events. No matching was used; extra ISR/FSR jets were generated by PYTHIA. These samples are large enough to suppress statistical fluctuations when we later use them to study the expected shape and magnitude of the asymmetry. In our studies, we have chosen to scale all LO signal cross-sections, for all six benchmark points, by a K-factor of 1.7, the same as for the  $t\bar{t}$  background.<sup>6</sup> Note that this K-factor can always be absorbed in  $g_R$ , as long as the width of the  $W'$  is smaller than the resolution.

---

<sup>6</sup>We note that the K-factor for the process  $bg \rightarrow tW$  is in this range (11), suggesting our choice is not unreasonable.

### 3.5 Analysis and results

Although the parton-level charge asymmetries described in Sec. 3.3 are large, the experimentally observable asymmetries are significantly diluted by the detector resolution and misreconstructions. Fig. 3.6 shows our estimate of the asymmetry structure that can be obtained at the detector level; compare this with Fig. 3.5. Note, however, that the basic structure of a negative asymmetry at the  $W'$  peak, with a positive asymmetry to either side, remains intact.

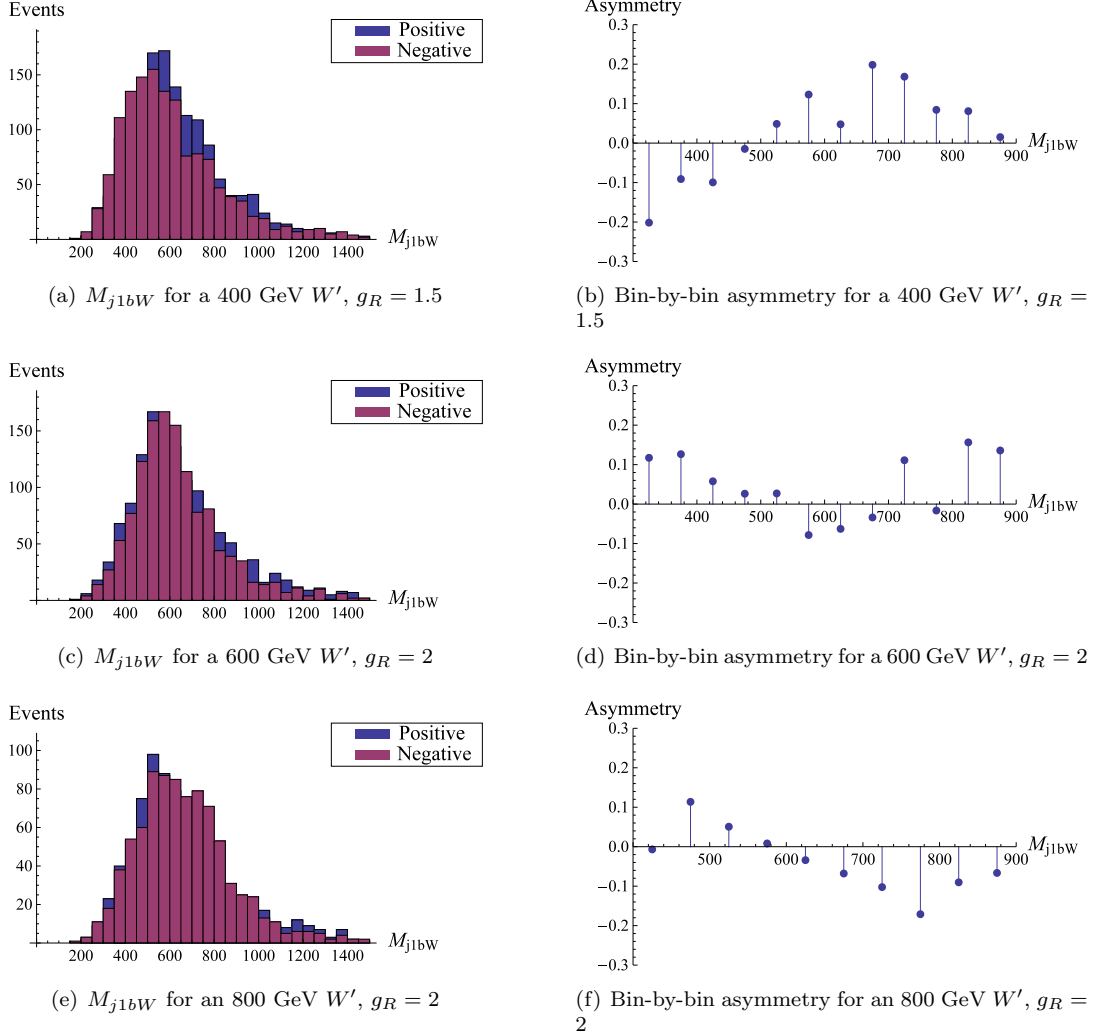


Figure 3.6: As in Fig. 3.5, but after accounting for detector effects, and with an  $S_T$  cut of 700 GeV, for three different  $W'$  masses. All plots show signal plus background. The samples correspond to an integrated luminosity of  $5 \text{ fb}^{-1}$ .

As always, one needs to obtain a prediction for both the Standard Model-only assumption (SM) and the Standard Model plus new physics assumption (NP), and assign a degree of belief to one or the other using a suitable statistical procedure, given the observed data. We will

argue below that the SM prediction for the asymmetry in  $M_{j1bW}$  is essentially zero, within the statistical uncertainties of the measurement. However, to predict the asymmetry in the presence of a signal requires a prediction of its dilution by the background. The background is also needed in order to predict the size of the fluctuations of the SM asymmetry around zero.

Direct use of Monte Carlo simulation to model the SM background distribution would be a source of large systematic errors, as NLO corrections are not known, and since we impose a hard cut on  $S_T$ . We therefore propose a (partially) data-driven method, minimizing this systematic error while keeping the statistical errors under control. The result can then be combined with a signal Monte Carlo to predict the differential asymmetry in  $M_{j1bW}$ . The search for a signal will then involve fitting this expectation to the data.

Our first task is to discuss how to obtain the prediction (which we will refer to as a “template”) for the differential asymmetry in  $M_{j1bW}$ , under both the SM and NP assumptions. We will begin by arguing that the SM asymmetry template is zero to a sufficiently good approximation. Next we will make a proposal for a partially data-driven method to determine the template for a given NP assumption, with low systematic uncertainty. Finally, we will estimate the sensitivity of our variables, using a simplified statistical analysis based in part on our proposed method. Along the way we will find the preferred value of the  $S_T$  cut.

### 3.5.1 The SM Template: Essentially Zero

It is crucial for our measurement that the asymmetry in the SM background be known, so that the presence of a signal can be detected. It would be even better if the SM asymmetry is very small. Here we give evidence that this is indeed the case.

It is essential to recognize that the SM background to the  $t\bar{t}j$  process is very different from the SM background to the  $t\bar{t}$  process. In  $t\bar{t}$ , all asymmetries are zero at LO. The non-vanishing SM asymmetry in  $t\bar{t}$  therefore arises from an NLO effect, involving both virtual corrections to  $t\bar{t}$  and real emission, that is,  $t\bar{t}j$ . The asymmetry therefore cannot be studied at all with a leading-order event generator, and in a matched sample (which contains  $t\bar{t}j$  but not the virtual correction to  $t\bar{t}$ ) it would actually have the wrong sign.

However, for  $t\bar{t}j$  itself, differential charge asymmetries at LO are *not* zero. The correction to these asymmetries from NLO corrections to  $t\bar{t}j$  are subleading in general. Therefore we can ask the following question of an LO generator: although the generic observable in  $t\bar{t}j$  events will show a charge asymmetry, is this the case for the  $M_{j1bW}$  variable, or is any asymmetry washed out?



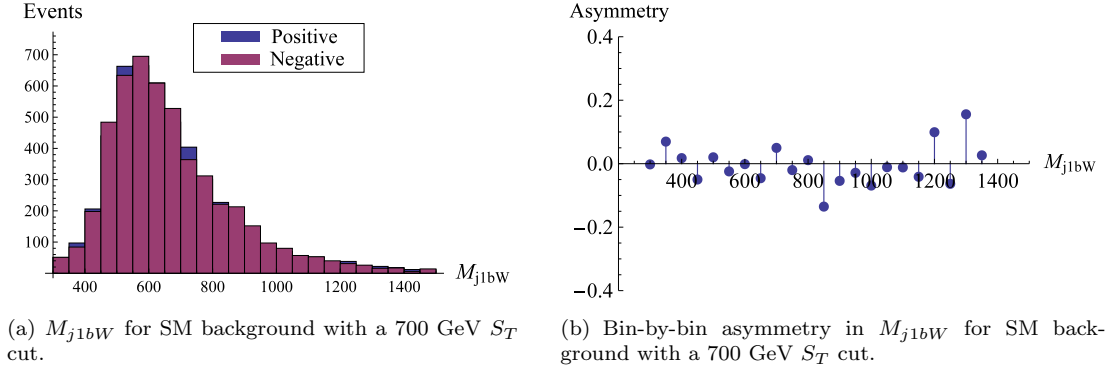


Figure 3.7: A parton-level study of the SM background asymmetry for the mass variable with a 700 GeV  $S_T$  cut, corresponding to  $12 \text{ fb}^{-1}$  luminosity. Other simulations confirm that the asymmetry appearing at 1200 – 1400 GeV is a statistical fluctuation.

We find that the asymmetry in the mass variable is consistent with zero, as one can see in Fig. 3.7. This also turns out to be true for the angle variable which we will discuss later. We emphasize that this was not guaranteed to be the case. One can find variables that, at LO and at parton-level, exhibit asymmetries. An example is the asymmetry between the  $P_T$  of the  $t$  and that of the  $\bar{t}$ , which is of order 4% at parton-level. The fact that  $qg \rightarrow t\bar{t}j$  has rather small asymmetries, and that the symmetric  $gg$  initial state contributes significantly to  $t\bar{t}j$ , helps to reduce the size of any observable asymmetries. After reconstruction and detector effects, nothing measurable remains.

We know of no reason why NLO corrections would change this conclusion. Neither virtual corrections nor real jet emission have any reason to strongly affect  $M_{j1bW}$ . For this reason we will treat the SM background as purely symmetric.

No argument of this type is airtight. Fortunately, the experiments do not need to rely entirely upon it. As we see in Fig. 3.6, the asymmetry in the signal has a characteristic kinematic structure. Moreover, related asymmetries will show up in several mass variables in a correlated way, due to the  $W'$ , and one would not expect similar correlations in the background. Finally, a signal is likely also to appear in the angle variable discussed in Sec. 3.6. The existence of these multiple cross-checks should allay any concerns that a measurement of a non-zero asymmetry might be uninterpretable.

### 3.5.2 Obtaining NP Templates and Accounting for Fluctuations

We now discuss how to obtain the NP template that is needed for each benchmark point. In addition one needs to be able to estimate the fluctuations that can occur under both the SM

and NP assumptions. We emphasize the possibility of data-driven approaches.

We will find it useful to introduce some notation (summarized in Table 3.2) in which  $S_i^\pm$  and  $B_i^\pm$  represent, for a signal-only and background-only Monte Carlo sample, the number of events in bin  $i$  with a positively- or negatively-charged lepton  $\ell^\pm$ .  $D_i^\pm$  denotes the similar quantity in data (and is thus not generally equal to the expected result  $S_i^\pm + B_i^\pm$ .) At some point we will need a smoothed version of the data, which we denote via  $[D_i^\pm]$ . The differential charge asymmetry predicted by the template for a particular benchmark point, or by the SM itself, we denote by  $\hat{A}_i$ . Meanwhile, we call the observed asymmetry in the data  $A_i$ .

Let us first focus on the statistical fluctuations around the template for the SM, which as we argued above in Sec. 3.5.1 can be taken to be zero. Whenever one needs this template, it is under the assumption that the data is pure SM. Even without signal, there will be plenty of data with  $\geq 5 \text{ fb}^{-1}$  and an  $S_T$  cut of order 700 GeV. It therefore appears that rather than obtain the fluctuations around zero using a Monte Carlo sample  $B_i$ , one would have much smaller systematic errors using the data  $D_i = D_i^+ + D_i^-$  itself. One could probably do even better using a fit  $[D_i]$  to the data, smoothing the bin-by-bin fluctuations in the numbers of events. We believe that the remaining statistical uncertainties that come with this method of modeling background will be smaller than the systematic uncertainties on an LO Monte Carlo for  $B_i$ . From this data-driven model, one may determine the expected size of the fluctuations on  $\hat{A}_i$  by performing a series of pseudo-experiments.

Next let us consider how to determine the template  $\hat{A}^i$  for a particular NP hypothesis. We could of course simply compute it from large Monte Carlo samples, with Monte Carlo integrated luminosity  $\mathcal{L}_{MC}$  much larger than the integrated luminosity in data  $\mathcal{L}_{data}$ , for  $S_i$  and  $B_i$ .

$$\hat{A}_i \equiv \frac{S_i^+ - S_i^-}{S_i^+ + S_i^- + B_i^+ + B_i^-} \quad (3.5.1)$$

|                     |   |
|---------------------|---|
| $B_i^+ (B_i^-)$     | Number of positive (negative) lepton events in $i^{th}$ bin, for background-only Monte Carlo.       |
| $S_i^+ (S_i^-)$     | As above, for signal-only Monte Carlo.  |
| $D_i^+ (D_i^-)$     | As above, in observed data.   |
| $[D_i^+] ([D_i^-])$ | As above, in a fit to the observed data.  |
| $\hat{A}_i$         | Predicted charge asymmetry the $i^{th}$ bin for a particular hypothesis.                            |
| $A_i$               | Charge asymmetry in $i^{th}$ bin as observed in data.   |
| $c_n$               | Amplitude for best fit of an NP template to the $n^{th}$ pseudo-experiment under the SM hypothesis. |
| $\tilde{c}$         | Amplitude for best fit of an NP template to the asymmetry observed in the data.                     |
| $\sigma_c$          | Standard deviation of the $c_n$ .   |

Table 3.2: Notation used throughout Sec. 3.5.

(Recall we are ignoring interference for now.<sup>7</sup>) Here the  $B_i^\pm$  cancel in the numerator, since the asymmetry in the SM background is assumed to be zero. With this approach statistical errors can be made arbitrarily small, but systematic errors on the SM background prediction could be very substantial. The process  $t\bar{t}j$  has never previously been measured at these energies, and after the  $S_T$  cut it is difficult to estimate how large the systematic errors might be. Moreover we know of no way to extract the  $t\bar{t}j$  background reliably, in the presence of signal, without the potential for signal contamination.

An alternative purely data-driven approach would be to use the suitably-fitted charge-symmetric data  $[D_i^+ + D_i^-]$  in the denominator of (3.5.1). For the numerator one may take a large Monte Carlo sample for  $S_i$ , and scale it to the luminosity of the data sample, giving

$$\hat{A}_i \equiv \frac{(S_i^+ - S_i^-) \frac{\mathcal{L}_{data}}{\mathcal{L}_{MC}}}{[D_i^+ + D_i^-]} \quad (3.5.2)$$

where again  $\mathcal{L}_{data}$  and  $\mathcal{L}_{MC}$  are the luminosities of the data and the signal Monte Carlo sample. This method introduces correlations between the prediction of the template  $\hat{A}^i$  and the measurement  $A^i$  which would have to be studied and accounted for. However, the systematic error introduced by these correlations may in many cases be much smaller than those introduced by relying on a Monte Carlo simulation for the denominator, as in (3.5.1). In addition, statistical errors that arise from the finite amount of data, which would be absent with a large Monte Carlo sample, are negligible, as can be seen as follows. The statistical error on the *predicted asymmetry*  $\hat{A}_i$  is dominated by fluctuations of the denominator of (3.5.2), since the statistical error on the *numerator* of (3.5.2) can be made arbitrarily small by increasing  $\mathcal{L}_{MC}$ :

$$\frac{\sigma(\hat{A}_i)}{\hat{A}_i} = \frac{1}{[D_i^+ + D_i^-]^{1/2}}. \quad (3.5.3)$$

However, for the *measured asymmetry*  $A_i$ , defined as  $A_i \equiv \frac{D_i^+ - D_i^-}{D_i^+ + D_i^-}$ , the error is always (for these models) dominated by the numerator:

$$\frac{\sigma(A_i)}{A_i} = \frac{1}{(D_i^+ + D_i^-)^{1/2}} \sqrt{\frac{1}{A_i^2} - 1}. \quad (3.5.4)$$

More precisely, since the largest observed asymmetries per bin will be of the order of 0.15, the statistical error on the observed asymmetry is always larger than the statistical error on the template —  $\sigma(A_i) \gg \sigma(\hat{A}_i)$ . And again we emphasize that this data-driven method reduces systematic uncertainties from what is often the largest source: the lack of confidence that the

---

<sup>7</sup>If interference cannot be neglected, as might happen with very large data sets or perhaps with other models that we have not explored in detail, then our separation of  $S_i$  and  $B_i$  is naive. What must then appear in the numerator is the difference of positive and negative lepton events in the combined signal and background. Systematic errors will then presumably be somewhat larger.

$t\bar{t}j$  background is correctly modeled. This comes at the relatively low cost of mild correlations between prediction and data, and some additional minor statistical uncertainty.

Partially data-driven approaches are also possible. Even if one uses  $[D_i]$ , the choice of fitting function could be determined in part with the use of Monte Carlos for  $B_i$  and  $S_i$ . Interestingly, the distribution in the variable  $M_{j1bW}$  is quite similar in signal and background, so the presence of signal, though it affects the overall rate, does not strongly affect the overall shape away from the  $W'$  resonance.

Since the pros and cons of these methods are luminosity-dependent, and dependent upon the details of the analysis, the only way to choose among these options is to do a study at the time that the measurement is to be made. We therefore do not attempt any optimization here. Whatever method is used, the last step in the process in obtaining the NP template is to fit the  $\hat{A}_i$  to a smooth function, which then serves as the template for the asymmetry in this particular benchmark point. (The size of the fluctuations around this template can again be obtained from  $[D_i]$ , as we suggested for the SM template.) After repeating this process for a grid of benchmark points, one may then compare the data to the SM null template or to any one of the NP templates. In the next subsection we will carry out a simplified version of this study, to investigate the effectiveness of our methods.

### 3.5.3 Effectiveness of Our Method: A Rough Test

A full evaluation of our method, carrying out precisely the same analysis that the experimentalists will need to pursue, would require more firepower than we have available. Instead we will carry out a somewhat simplified analysis, asking the following question:

*If the NP hypothesis for a certain benchmark point is realized in the data, what is the average confidence level at which we can reject the SM hypothesis?*

The answer to this question will serve two purposes. First, it will give a measure of how sensitive a complete analysis will be for distinguishing the SM from various NP scenarios. (More precisely, it will be slightly optimistic, as we will discuss, but not overly so.) Second, it will allow us to estimate what value of the  $S_T$  cut is optimal for different benchmark points.

We have not yet said much about the  $S_T$  cut, so let us remark on it now. Without such a cut, the signal to background ratio in the  $t\bar{t}j$  sample is small, as small as 1:45 for  $m_{W'} = 800$  GeV with  $g_R = \sqrt{2}$ . However, the situation can be much improved using the fact that the signal  $S_T$  distribution tends (especially for heavy  $W'$ s) to sit at much larger values for signal than for the SM background. (See Fig. 3.8; note these plots show the  $S_T$  distributions for our

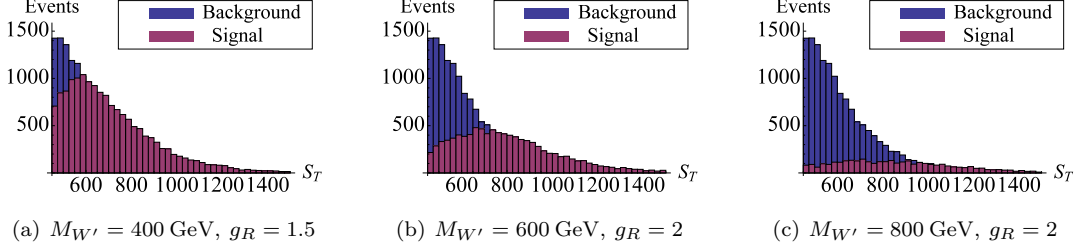


Figure 3.8:  $S_T$  distributions of signal and background, for various benchmark points. For computational reasons we did not simulate events with  $S_T < 450 \text{ GeV}$ . The samples correspond to  $8 \text{ fb}^{-1}$ .

large- $g_R$  benchmark points. From this one can see that a simple counting experiment would not be trivial.) The optimal value of the  $S_T$  cut depends on the model, the analysis method and the luminosity. For most of our purposes an  $S_T$  cut of the order of 700 GeV is suitable, as we will see later.

Answering the italicized question posed above is equivalent to evaluating the probability for fluctuations about the SM assumption to create a differential asymmetry  $A_i$  that resembles the pattern predicted by the NP assumption  $\hat{A}_i$ . For this we need (a) the template  $\hat{A}_i$  for the NP assumption and (b) an estimate of the size of the fluctuations that can occur under the SM assumption.

We have discussed above how to obtain these things from the data at the LHC. But since the actual data  $D_i$  are not yet available, we obtain our NP template  $\hat{A}_i$  from large  $S_i$  and  $B_i$  Monte Carlo samples, using formula (3.5.1). Obtaining the fluctuations under the SM assumption is a bit subtle. Since in this section we are *assuming* the data itself contains a signal, our background model must be obtained, according to our data-driven strategy, from our simulation of  $S_i + B_i$  (and not from  $B_i$  alone!) We take the expected numbers of positive- and negative-charge lepton events to both be equal to half of  $S_i + B_i$ . We then study the fluctuations around this background model by performing 50 000 Poisson-fluctuating pseudo-experiments, for positive- and negative-lepton events independently, and computing the differential asymmetry for each one.

Finally, to address our italicized question, we must then ask: what is the probability for fluctuations of the asymmetry around zero, given this background model, to resemble the “data”? This is done as follows: For each pseudo-experiment, we fit the differential asymmetry to the NP template  $\hat{A}_i$  of our benchmark point, *keeping the shape of the NP template fixed but allowing the amplitude to float*. The best-fit amplitude we denote by  $c_n$ , where the index  $n$  labels the pseudo-experiment. For illustration, some examples for a couple of pseudo-experiments are

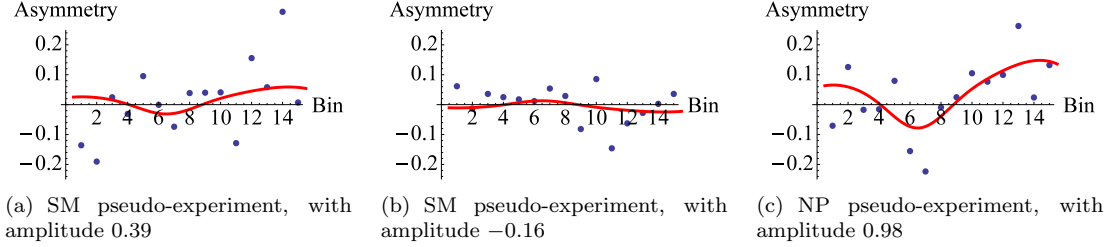


Figure 3.9: Two examples of possible fluctuations of the differential charge asymmetry under the SM hypothesis, and one example under the NP hypothesis. The red line is the best fit of the amplitude of the NP template to the pseudo-experiment, with the shape held fixed. The NP template that was chosen corresponds to the 600 GeV  $W'$  with  $g_R = 2$  and  $S_T > 700$  GeV. The fluctuations are representative for a  $5 \text{ fb}^{-1}$  sample.

shown in Figs. 3.9(a) and 3.9(b).

Under the SM assumption (zero asymmetry), the expectation value of the  $c_n$  is zero. (Similarly, under the correct NP assumption, the expectation would be 1.) The  $c_n$  follow a Gaussian distribution, whose width gives the standard deviation  $\sigma_c$  of the  $c_n$  around zero. If an amplitude of size  $\tilde{c}$  were observed in the data, the  $p$ -value (chance of a fluctuation on the SM hypothesis to produce a structure with amplitude  $\tilde{c}$  or larger) is then:

$$P[X > \tilde{c}] = \frac{1}{\sqrt{2\pi}\sigma_c} \int_{\tilde{c}}^{+\infty} dc e^{-\frac{1}{2}(c/\sigma_c)^2}. \quad (3.5.5)$$

To get a measure of typical significance, we compute  $P[X > 1]$ , the probability for the SM to produce an  $A_i$  resembling the template  $\hat{A}_i$  with an amplitude  $\tilde{c}$  exceeding 1. (Recall that  $\tilde{c} = 1$  would be the expected value given that nature has chosen this benchmark point.) The results of this procedure for our benchmark points, after conversion to standard deviations on a Gaussian, are displayed in Table 3.3, for two integrated luminosities and for the optimal  $S_T$ -cut (see below.) In Appendix 3.8, we also present contour plots of the significance as a function of the integrated luminosity and the  $S_T$  cut; see Figs. 3.12 and 3.13.

The amount by which the *observed* significance tends to fluctuate around the *expected* significance depends on the luminosity and the  $S_T$  cut. By running a different set of pseudo-experiments based on the NP hypothesis, we can obtain the Gaussian distribution of the amplitude of the fit. (An example of such a pseudo-experiment is shown in Fig. 3.9(c).) Values for the width of this distribution give us the statistical error bar on the expected significance, and are included in Table 3.3.

Our simplified analysis is imperfect in various ways. One important weakness is that we assume that nature matches one of our benchmark points, and we do not consider the effect of using the wrong benchmark point in obtaining the exclusion of the SM. In particular, the mass

| $M_{W'}$<br>(GeV) | $g_R$                  | $S_T^{\text{cut}}$<br>(GeV) | Significance        |                     |
|-------------------|------------------------|-----------------------------|---------------------|---------------------|
|                   |                        |                             | $5 \text{ fb}^{-1}$ | $8 \text{ fb}^{-1}$ |
| 400               | 1.5                    | 750                         | $6.27 \pm 0.92$     | $7.49 \pm 0.75$     |
| 400               | $\frac{1.5}{\sqrt{2}}$ | 750                         | $3.38 \pm 0.95$     | $4.24 \pm 0.95$     |
| 600               | 2                      | 700                         | $3.42 \pm 0.92$     | $4.08 \pm 0.95$     |
| 600               | $\sqrt{2}$             | 700                         | $1.79 \pm 0.83$     | $2.15 \pm 0.86$     |
| 800               | 2                      | 700                         | $2.37 \pm 0.87$     | $3.12 \pm 0.92$     |
| 800               | $\sqrt{2}$             | 700                         | $1.60 \pm 0.82$     | $2.01 \pm 0.85$     |

Table 3.3: Expected significance and statistical error for SM exclusion at our benchmark points, given selected luminosities and optimal  $S_T$  cuts. For the correct interpretation of these numbers, please refer to the text.

of the  $W'$  we used to obtain the NP template matches the mass of the  $W'$  in our “data”. A finer grid in  $W'$  mass would address this. (In general, the coupling  $g_R$  for the template will also differ from the real coupling, but except for its effect on the  $W'$  width, often smaller than the experimental resolution, a change in the coupling affects the amplitude, but not the shape, of the corresponding template.) Also, our simplified procedure to fit only for the amplitude of the template and to keep the shape fixed does not always capture all the features of the asymmetry distribution, as is illustrated in Fig. 3.9(c), where the central dip in the asymmetry is deeper than our fit function can capture. In a more detailed study one might choose to let multiple parameters float to obtain a better fit. We further note that we are not accounting for the look-elsewhere effect. And finally, although the use of asymmetries and a data-driven method reduces systematic errors, we have not considered the remaining systematic errors here.

On the other hand, there are important features of the signal that we are not using in our analysis, and including those would enhance the sensitivity. The use of several (correlated) mass variables, and the angle variable discussed in the next section, would give some improvements. Moreover, while the charge asymmetry we focus on here has low systematic errors but is statistically limited, other observables with higher systematics but lower statistical errors, such as the differential cross-section with respect to  $S_T$ , are obviously useful as well. In any search for this type of models multiple approaches should be combined.

### 3.6 An angle variable

In this section we discuss another charge-asymmetric variable, the azimuthal angle between the hardest jet without a  $b$ -tag ( $j_1$ ) and the lepton  $\ell$ :

$$\Delta\phi_{j_1,\ell} = \text{Min}\left[|\phi_{j_1} - \phi_\ell|, 2\pi - |\phi_{j_1} - \phi_\ell|\right]. \quad (3.6.1)$$

With a low  $S_T$  cut, the angle between the hardest jet and an  $\ell^-$  tends to be larger than the angle between the hardest jet and an  $\ell^+$  [Figs. 3.10(a) and 3.10(b)]. The reason is as follows: The  $W'$  is produced near threshold, so the recoiling top quark or antiquark is not highly boosted. The top from the  $W'$  decay, on the other hand, will recoil back-to-back against the  $d$  or  $\bar{d}$  (which is usually the source of the hardest jet). Moreover, this top will be somewhat boosted since  $m_{W'} \gg m_t$ , so if it decays leptonically, the lepton's momentum tends also to be back-to-back to the  $d$  or  $\bar{d}$ . This results in a large opening angle between the hardest jet and the lepton. However, if it is the other top quark that decays leptonically, the angle of its lepton with the hardest jet is more randomly distributed. Since the negatively charged  $W'$  is produced more abundantly, this variable will exhibit a charge asymmetry.

For a high  $S_T$  cut the picture reverses. The  $W'$  and the top from which it recoils are now both boosted and typically back-to-back with one other. The decay products from the  $W'$  tend to be aligned with each other. In other words, a cluster of four objects (from the  $W'$ ) is now recoiling against a cluster of three objects (the top). The hardest jet is typically still the down quark from the  $W'$  decay. If the lepton's parent is the top from the  $W'$ ,  $\Delta\phi_{j_1\ell}$  tends to be small, while the opposite is true if the lepton comes from the recoiling top. (See Figs. 3.10(c) and 3.10(d).)

This reversing structure in the asymmetry as a function of the  $S_T$  cut is useful, as it potentially provides a very strong hint of new physics. However, there is an intermediate  $S_T$  cut where the asymmetry is essentially zero, so in that range the variable is not useful. For this reason, we recommend studying this variable *as a function of the  $S_T$  cut*.

We explicitly checked that the standard model will not introduce a large asymmetry in this angle variable, for any  $S_T$  cut. A particular case is shown in Fig. 3.11. Our reasoning for trusting a LO Monte Carlo is the same as was described in Sec. 3.5.1 for the mass variable.

An interesting feature of this angle variable in the  $W'$  model (though whether this is true in other models has not yet been studied) is that the point where the number of positive and negative lepton events is roughly equal is insensitive to  $m_{W'}$  and  $g_R$ . For all our benchmark points we find  $\Delta\phi_{j_1,\ell} \approx 2$  to be a suitable place to break the signal into two bins. The detector-level asymmetries in both bins are given in Table 3.4. To estimate the significance, we follow a strategy similar to the one mentioned for the mass variable. However instead of fitting for the amplitude of a previously obtained template, we compute the difference of the asymmetry of the two superbins and establish the Gaussian probability distribution for this variable using pseudo-experiments on the SM hypothesis. Plots of the resulting significance of this observable as a function of  $S_T$  cut and luminosity can be found in Figs. 3.14 and 3.15 in Appendix 3.8.



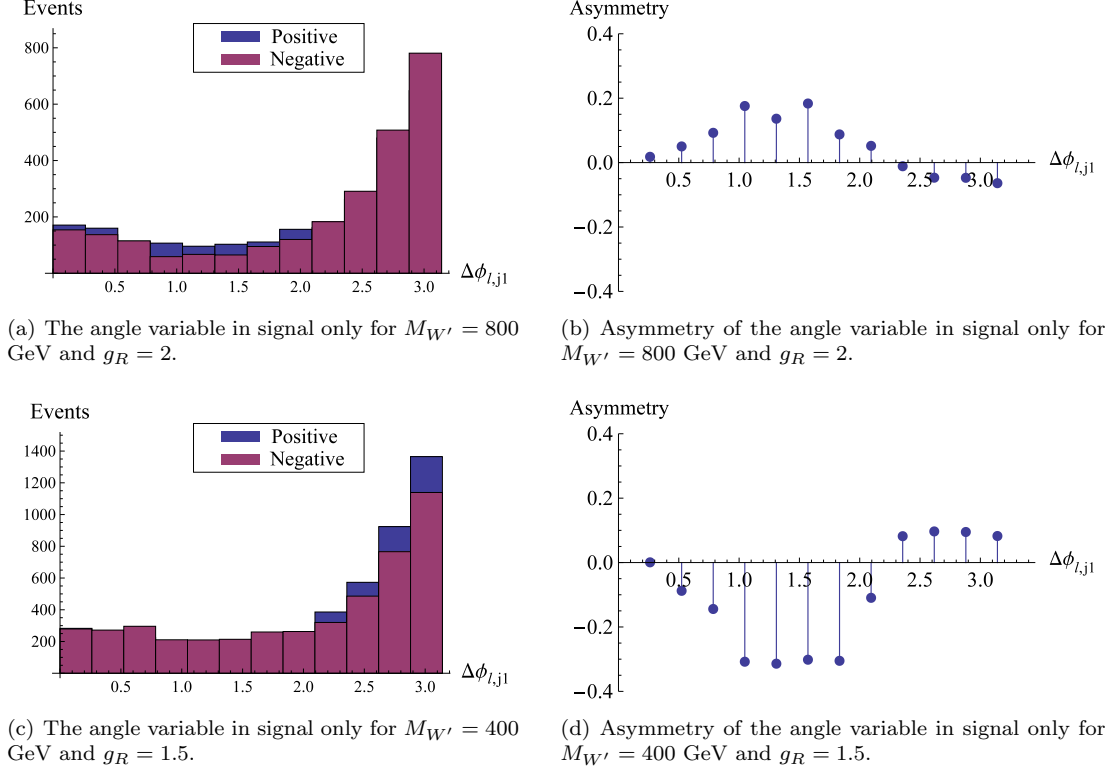


Figure 3.10: Angle difference between the lepton and the hardest jet at parton-level signal-only, for  $W'$ 's of mass 800 and 400 GeV with an  $S_T$  cut at 700 GeV. The samples correspond to  $5 \text{ fb}^{-1}$ .

The greatest merit of the angle variable is its simplicity. Both the hardest jet and the lepton are well-measured, and in contrast to the mass variables no (partial) event reconstruction is needed. Unfortunately the angle variable is more sensitive than  $M_{j1bW}$  to interference effects between signal and background. Whether the contribution from interference is positive or negative depends on the mass of new particle, the  $S_T$  cut and the model we study. The effect, however, appears to be only moderate. We find that, for a  $W'$  mass of 800 GeV and an  $S_T$  cut of 700 GeV, the asymmetry for the two bins after interference is included is reduced by about 15%. A more detailed study including interference is advisable to give a precise estimate of its effects, especially for other models where interference might be more important.

### 3.7 Final Remarks

At the LHC, models that attempt to explain the Tevatron  $t\bar{t}$  forward-backward asymmetry with the exchange of a particle  $X$  in the  $t$ - or  $u$ -channel generate a charge-asymmetric signal in  $tX$  production. This leads to observable charge asymmetries in certain variables within  $t\bar{t}j$

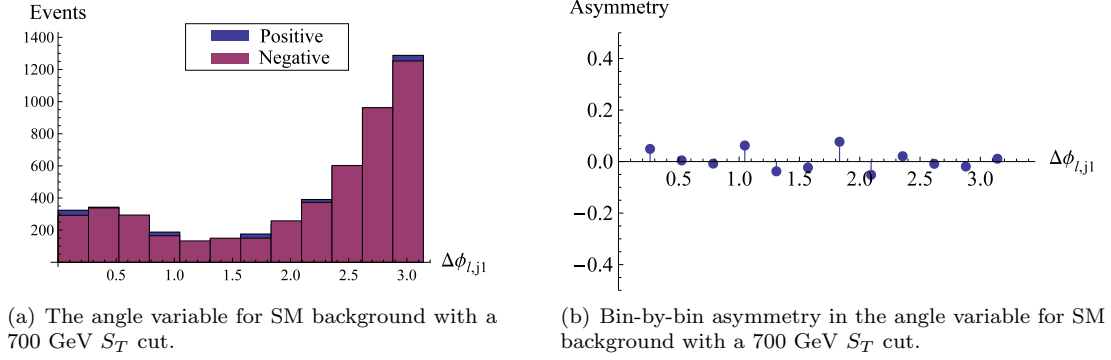


Figure 3.11: A parton-level study on SM background asymmetry for the angle variable with a 700 GeV  $S_T$  cut, corresponding to  $12 \text{ fb}^{-1}$  luminosity.

| $M_{W'}$<br>(GeV) | $g_R$                  | $S_T$ cut<br>(GeV) | Asymmetry (%)       |                     |
|-------------------|------------------------|--------------------|---------------------|---------------------|
|                   |                        |                    | 1 <sup>st</sup> bin | 2 <sup>th</sup> bin |
| 400               | 1.5                    | 800                | -13.7               | 10.2                |
| 400               | $\frac{1.5}{\sqrt{2}}$ | 800                | -9.3                | 7.0                 |
| 600               | 2                      | 1200               | -9.6                | 12                  |
| 600               | $\sqrt{2}$             | 1200               | -6.8                | 8.7                 |
| 800               | 2                      | 700                | 3.8                 | -2.4                |
| 800               | $\sqrt{2}$             | 700                | 2.4                 | -1.7                |

Table 3.4: Expected asymmetry at detector-level in the angle variable for each superbin, for our benchmark points using the optimal  $S_T$  cut.

samples. Among interesting observables are mass variables involving various final state objects including the hardest jet and/or the lepton (Secs. 3.3 and 3.5), the azimuthal angle between the lepton and the hardest jet (Sec. 3.6) and the  $P_T$  difference between the tops and  $W$  bosons (Appendix 3.10). Of these variables, the invariant mass of the hardest jet, the leptonic  $W$  and a  $b$ -tagged jet appears to be the most powerful and the most universal, since it tends to reconstruct the  $W'$  mass resonance. The charge asymmetry of this variable exhibits a negative asymmetry in the region of the  $W'$  mass, and a positive asymmetry elsewhere. We have proposed a data-driven method to extract a statistical significance from this asymmetry structure.

One could of course go further by fully reconstructing the events, and directly observe that  $W'^-$  production is larger than  $W'^+$  production. However demanding full reconstruction would lead to a considerable loss of efficiency. Since we cannot realistically estimate this efficiency loss, we cannot evaluate the pros and cons of this approach, but clearly the experiments should do so.

We have described this asymmetry measurement on its own, without discussing the fact that

simultaneously the experiments will be measuring charge-symmetric variables, such as the cross-section for  $t\bar{t}j$  as a function of  $S_T$ . Of course these variables are complementary, and we do not in any way mean to suggest that one should do one instead of the other. Charge-symmetric variables may often have lower statistical uncertainties, but in most cases background-subtraction is necessary, so there will be large systematic errors. The combination of the two types of measurements will help clarify the situation far better than either one could in isolation. Additional information will come from the differential charge asymmetry in  $t\bar{t}$  events at the LHC, which is a direct test of the Tevatron measurement of the  $t\bar{t}$  forward-backward asymmetry, and is sensitive to any growth of the effect with energy.

A very important aspect of our approach is that the asymmetry is a diagnostic for models. An  $s$ -channel mediator will not generate a peak for either lepton charge, and so even if an asymmetry in  $t\bar{t}j$  were generated, it would be largely washed out in the variable  $M_{j1bW}$ . Among models with  $t$ - or  $u$ -channel mediators  $X$ , *some will produce a negative asymmetry at  $M_{j1bW} = m_X$ , while others will produce a positive asymmetry.* For example, models that replace the  $W'$  by a color triplet or color sextet scalar  $X$  (67; 68; 69; 70) that couples to  $u_R$  and  $t_R$  (and has charge  $4/3$ ) will have the opposite sign, because the process  $ug \rightarrow \bar{t}X^+$  will be larger than  $\bar{u}g \rightarrow tX^-$ . The approach we use will still apply, but the asymmetry will be positive in the neighborhood of the  $X$  mass peak, rather than negative as it is for the  $W'$ . For this reason, *even if it turns out that the asymmetry measurement is not needed for a discovery of the  $X$  particle, it will still be an essential ingredient in determining its quantum numbers and couplings.*

What seems clear from our results is that the data already available (or soon to be available) at the 7 TeV LHC should be sufficient to allow for an informative measurement of charge-asymmetric observables in  $t\bar{t}j$  to be carried out. We look forward to seeing studies of  $t\bar{t}j$  from ATLAS and CMS, and we hope that measurements of charge asymmetries will be among them.

### 3.8 Appendix A: Additional Results

#### 3.8.1 Contour plots for the mass variable

As can be seen in Figs. 3.12 and 3.13, we find that the optimal  $S_T$ -cut for the mass variable does not vary greatly with luminosity, or even with the  $W'$  mass: it lies around 700 GeV for the 600 GeV and 800 GeV  $W'$  and is slightly higher for the 400 GeV  $W'$ . At lower  $S_T$  cuts, reduced signal-to-background ratio worsens the significance. The reason a large  $S_T$  cut works well even for low  $W'$  mass is that the distribution for the charge-symmetric component of the signal (mainly  $t$ -channel  $W'$  exchange) peaks at low  $S_T$  for a lighter  $W'$ . Meanwhile, for an overly high  $S_T$  cut the remaining signal is too small. But we should mention that our binning procedure makes our results too pessimistic here.

When producing these contour plots, we choose a fixed binsize of 50 GeV everywhere except in the upper and lower tails of the distribution, where we use a superbin. The superbins are sized so that that no bin ever contains fewer than 50 events. For higher  $S_T$ , there are very few bins between the two superbins, and this makes the peak-valley-peak structure weak, ruining the significance of the measurement. Within the white region in the upper left of the plots, the number of events is so small that no bin with more than 50 events exists, and our binning strategy gives a null result. However, for a high  $S_T$  cut one could choose a more sophisticated binning strategy. We have verified in a few particular cases that larger bins for higher  $S_T$  cuts can restore some of the significance of the measurement. All of this is to say that sophisticated treatment of the data may lead to a somewhat better result than our simple-minded binning strategy would suggest.

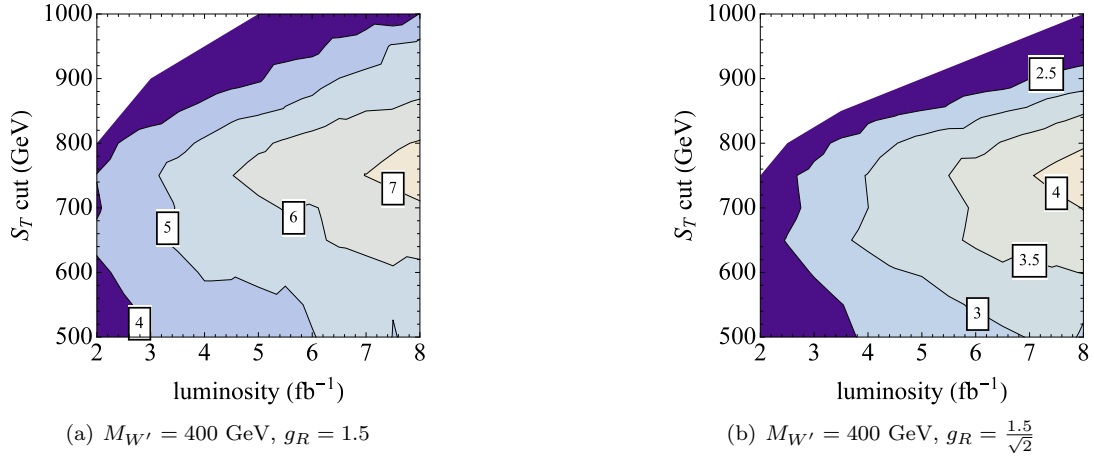


Figure 3.12: Expected significance of the  $M_{j1bW}$  variable for a 400 GeV  $W'$ , as a function of luminosity and  $S_T$  cut.

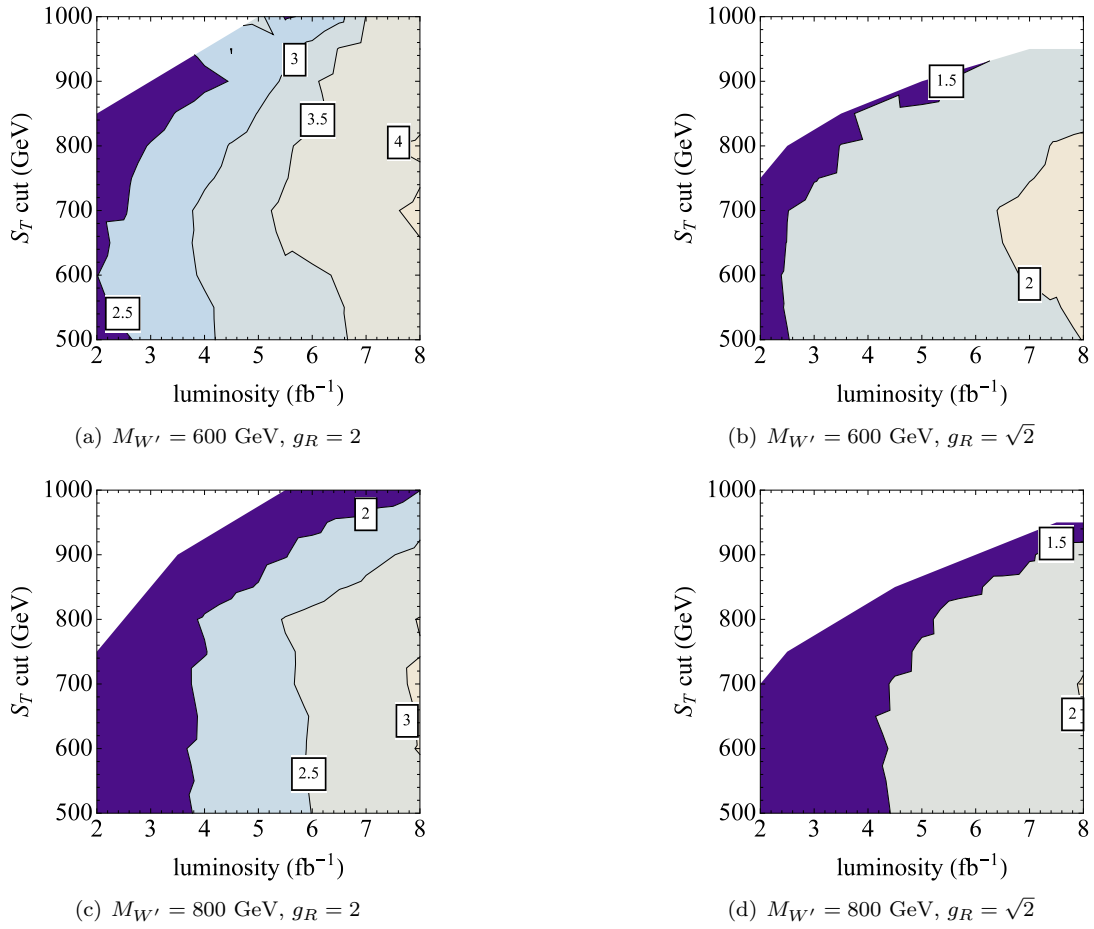


Figure 3.13: Expected significance of the  $M_{j1bW}$  variable for a 600 GeV and an 800 GeV  $W'$ , as a function of luminosity and  $S_T$  cut.

### 3.8.2 Contour plots for the angle variable

The plots below show the significance for exclusion of the SM hypothesis using the angle variable, along the lines of our method used for the mass variable. Note the band of low significance for the  $W'$  with mass of 600 GeV, caused by the shifting structure that we emphasized in Sec. 3.6; for an  $S_T$  cut of around 700 GeV, the asymmetry shifts from one sign to the other. A study exploiting this dependence of the asymmetry on the  $S_T$  cut would have larger significance, but we have not explored this option here.

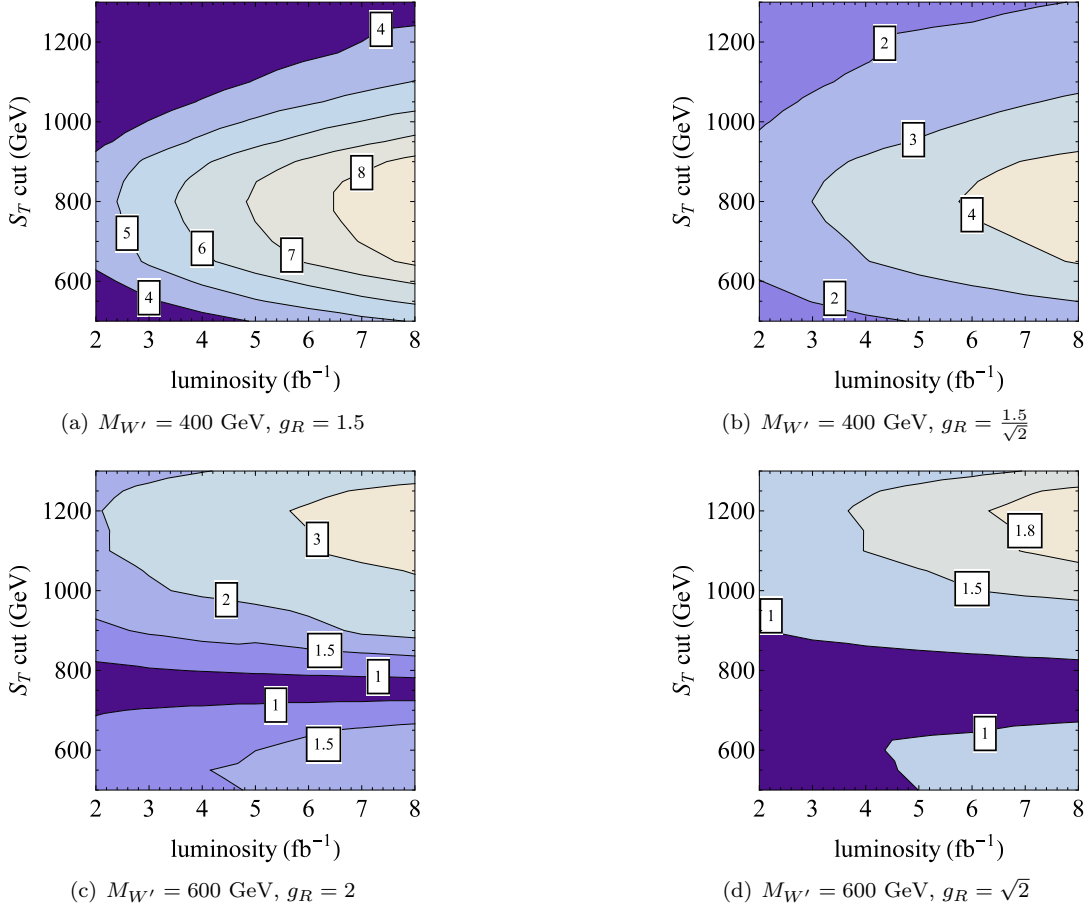


Figure 3.14: Expected significance of  $\Delta\phi_{j1,\ell}$  for a 400 GeV and a 600 GeV  $W'$ , as a function of luminosity and  $S_T$  cut. For the 600 GeV  $W'$  the dark band corresponds to the range of  $S_T$  cuts where the asymmetry is changing sign, which results in a much reduced sensitivity. Interference between signal and background is not accounted for.

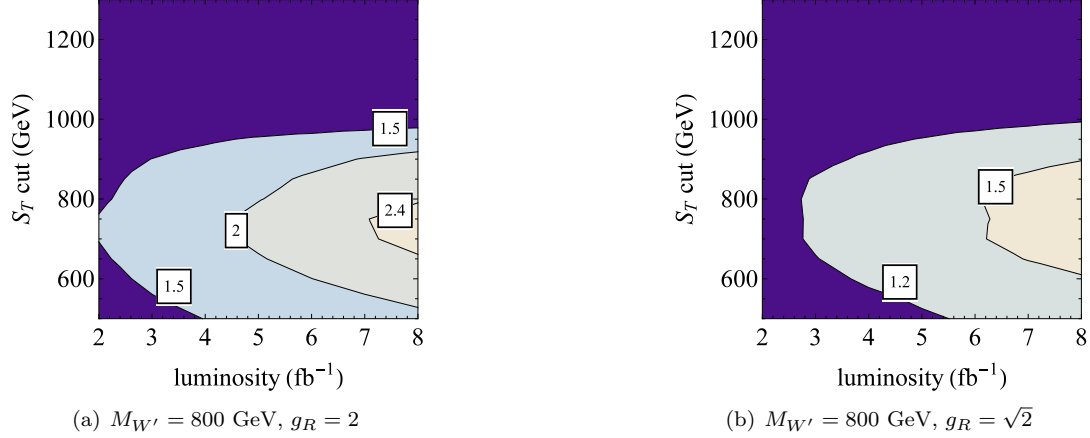


Figure 3.15: Expected significance of  $\Delta\phi_{j1,\ell}$  for an 800 GeV  $W'$ , as a function of luminosity and  $S_T$  cut. Interference between signal and background is not accounted for.

### 3.9 Appendix B: Strategy Details

#### 3.9.1 Isolation Procedure

The detector simulation DELPHES produces particle candidates and requires the user to impose the isolation criteria of his or her choice. Hence for each lepton candidate in the DELPHES output there will be a corresponding jet candidate, and it is up to the user to decide which one to include in the analysis. To facilitate this choice, DELPHES provides the user with the following variables for each lepton:

- $\Sigma P_T$ : The sum of the  $P_T$  of all the tracks with  $P_T > 0.9$  GeV in a cone of  $\Delta R = 0.3$  around the leading track, excluding that track.
- $\rho_l$ : The sum of the energy deposited in a  $3 \times 3$  calorimeter grid around the leading track, divided by the  $P_T$  of that track.

Here we lay out the isolation criteria we imposed on the various particle candidates. An isolated electron is defined as an electron candidate for which  $\Sigma P_T < 10$  GeV,  $\Sigma P_T < 0.15 P_T^e$  and  $\rho_e < 1.15$ . For isolated muons we require  $\Sigma P_T < 10$  GeV,  $\Sigma P_T < 0.15 P_T^\mu$  and  $\rho_\mu < 0.15$ . Finally jet candidates are retained if no isolated leptons are found in a cone of radius 0.3. When a previously isolated lepton is found in a 0.3 cone, the jet candidate is identified with the lepton and therefore removed from the event. We hereby impose two consistency conditions:

- No more than 1 isolated lepton is found in a 0.3 cone
- When one isolated lepton is found, the  $P_T$  of the jet candidate can differ by no more than 10% from the  $P_T$  of the isolated electron.

When one of these criteria is not met, we are unable to carry out a consistent isolation procedure and the entire event is thrown out. The efficiency of our isolation procedure is 97%, both for signal and background samples.

### 3.10 Appendix C: The $P_T$ -difference variables

Among other variables that show charge-asymmetries, ones of possible further interest include the difference in  $P_T$  between the  $t$  and the  $\bar{t}$ , or between the positive and negative  $W$  bosons.

Since one top quark is recoiling against the  $W'$ , while the other top quark is a decay product of the  $W'$ , one would expect their kinematics to differ. The  $P_T$  difference between the  $t$  and  $\bar{t}$  is a variable in which this feature of the signal will manifest itself. The same is true for the  $W$  bosons from the  $t$  and  $\bar{t}$  decays. For each event, we can calculate

$$\Delta P_{T,W} = \frac{P_{T,W^+} - P_{T,W^-}}{P_{T,W^+} + P_{T,W^-}} \quad \text{and} \quad \Delta P_{T,t} = \frac{P_{T,t} - P_{T,\bar{t}}}{P_{T,t} + P_{T,\bar{t}}}. \quad (3.10.1)$$

The charge asymmetry at parton-level for these variables can be seen (for pure signal) in Figs. 3.16(a) and 3.16(b).

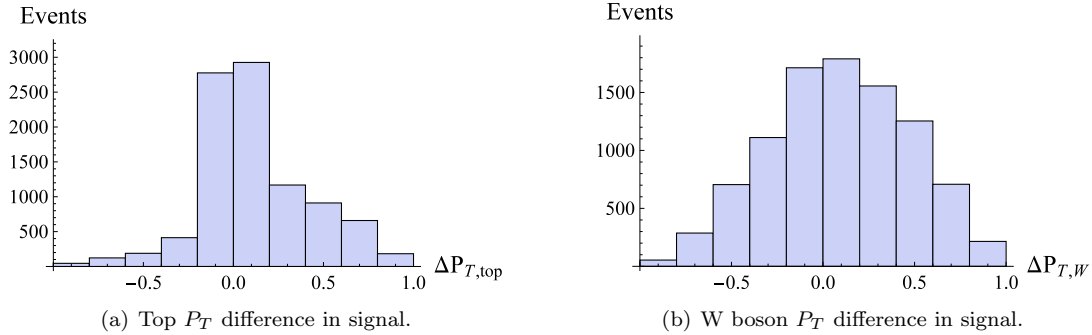


Figure 3.16: Top quark and W boson  $P_T$  difference at parton-level in signal with a 400 GeV  $W'$  with  $S_T$  cut at 700 GeV. The sample is corresponding to a luminosity of  $5 \text{ fb}^{-1}$ .

Although spectacular at parton-level, we find that the  $P_T$  difference between the top quarks gets washed out a lot at detector-level by resolution effects and mis-reconstructions. Nevertheless we encourage experimental colleagues to take this variable in consideration, since state-of-the-art top reconstruction methods might alleviate this problem. The  $P_T$  difference between the  $W$  bosons is less pronounced at parton-level, but does survive our detector simulation and the reconstruction of the hadronic  $W$ . We find it is particularly useful for a low mass  $W'$ . Like the angle variable, it changes sign as a function of the  $S_T$  cut.

We have not studied the effect of interference on these  $P_T$  variables. Whether the asymmetry from the SM  $t\bar{t}j$  background is important also requires further study.



## Bibliography

- [1] CDF Collaboration , Phys. Rev. **D83**, 112003 (2011). [arXiv:1101.0034 [hep-ex]].
- [2] D0 Collaboration, [arXiv:1107.4995 [hep-ex]].
- [3] CDF Collaboration, CDF Note No. 10436
- [4] D0 Collaboration, Phys. Rev. Lett. **100**, 142002 (2008). [arXiv:0712.0851 [hep-ex]].
- [5] J. H. Kuhn, G. Rodrigo, Phys. Rev. Lett. **81**, 49-52 (1998). [arXiv:9802268 [hep-ph]].
- [6] J. H. Kuhn, G. Rodrigo, Phys. Rev. **D59**, 054017 (1999). [arXiv:9807420 [hep-ph]].
- [7] M. T. Bowen, S. D. Ellis, D. Rainwater, Phys. Rev. **D73**, 014008 (2006). [arXiv:0509267 [hep-ph]].
- [8] L. G. Almeida, G. F. Sterman, W. Vogelsang, Phys. Rev. **D78**, 014008 (2008). [arXiv:0805.1885 [hep-ph]].
- [9] V. Ahrens, A. Ferroglia, M. Neubert, B. D. Pecjak, L. L. Yang, [arXiv:1106.6051 [hep-ph]].
- [10] J. H. Kuhn and G. Rodrigo, [arXiv:1109.6830 [hep-ph]].
- [11] N. Kidonakis, PoSDIS **2010**, 196 (2010) [arXiv:1005.3330 [hep-ph]].
- [12] ATLAS Collaboration, Technical Report ATLAS-CONF-2011-106, CERN, Geneva, Aug 2011
- [13] CMS Collaboration, CMS-PAS-TOP-10-010, CERN, Geneva, 2010.
- [14] CMS Collaboration, CMS-PAS-TOP-11-014, CERN, Geneva, 2011.
- [15] P. Langacker, R. W. Robinett, and J. L. Rosner, Phys. Rev. D30, 1470 (1984).
- [16] M. Dittmar, Phys. Rev. D **55**, 161 (1997) [arXiv:9606002 [hep-ex]].
- [17] Y. Li, F. Petriello and S. Quackenbush, Phys. Rev. D **80**, 055018 (2009) [arXiv:0906.4132 [hep-ph]].

- [18] Y. -K. Wang, B. Xiao, S. -H. Zhu, Phys. Rev. **D83**, 015002 (2011). [arXiv:1011.1428 [hep-ph]].
- [19] L. M. Sehgal, M. Wanninger, Phys. Lett. **B200**, 211 (1988).
- [20] J. Bagger, C. Schmidt, S. King, Phys. Rev. **D37**, 1188 (1988).
- [21] A. Djouadi, G. Moreau, F. Richard, R. K. Singh, Phys. Rev. **D82**, 071702 (2010), [arXiv:0906.0604 [hep-ph]].
- [22] P. Ferrario, G. Rodrigo, Phys. Rev. **D80**, 051701 (2009), [arXiv:0906.5541 [hep-ph]].
- [23] P. H. Frampton, J. Shu, K. Wang, Phys. Lett. **B683**, 294-297 (2010), [arXiv:0911.2955 [hep-ph]].
- [24] R. S. Chivukula, E. H. Simmons, C. -P. Yuan, Phys. Rev. **D82**, 094009 (2010), [arXiv:1007.0260 [hep-ph]].
- [25] M. Bauer, F. Goertz, U. Haisch, T. Pfoh, S. Westhoff, JHEP **1011**, 039 (2010), [arXiv:1008.0742 [hep-ph]].
- [26] C. -H. Chen, G. Cvetič, C. S. Kim, Phys. Lett. **B694**, 393-397 (2011), [arXiv:1009.4165 [hep-ph]].
- [27] E. Alvarez, L. Da Rold, A. Szyrkman, JHEP **1105**, 070 (2011), [arXiv:1011.6557 [hep-ph]].
- [28] C. Delaunay, O. Gedalia, S. J. Lee, G. Perez and E. Ponton, Phys. Lett. B **703**, 486 (2011) [arXiv:1101.2902 [hep-ph]].
- [29] Y. Bai, J. L. Hewett, J. Kaplan, T. G. Rizzo, JHEP **1103** (2011) 003. [arXiv:1101.5203 [hep-ph]].
- [30] E. R. Barreto, Y. A. Coutinho, J. Sa Borges, Phys. Rev. **D83**, 054006 (2011), [arXiv:1103.1266 [hep-ph]].
- [31] R. Foot, Phys. Rev. D **83**, 114013 (2011) [arXiv:1103.1940 [hep-ph]].
- [32] A. R. Zerwekh, Phys. Lett. B **704**, 62 (2011) [arXiv:1103.0956 [hep-ph]].
- [33] R. Barcelo, A. Carmona, M. Masip, J. Santiago, Phys. Rev. **D84**, 014024 (2011). [arXiv:1105.3333 [hep-ph]].
- [34] U. Haisch and S. Westhoff, JHEP **1108**, 088 (2011) [arXiv:1106.0529 [hep-ph]].

- [35] R. Barcelo, A. Carmona, M. Masip, J. Santiago, [arXiv:1106.4054 [hep-ph]].
- [36] E. Gabrielli and M. Raidal, Phys. Rev. D **84**, 054017 (2011) [arXiv:1106.4553 [hep-ph]].
- [37] G. M. Tavares and M. Schmaltz, Phys. Rev. D **84**, 054008 (2011) [arXiv:1107.0978 [hep-ph]].
- [38] E. Alvarez, L. Da Rold, J. I. S. Vietto and A. Szyrkman, JHEP **1109**, 007 (2011) [arXiv:1107.1473 [hep-ph]].
- [39] J. A. Aguilar-Saavedra, M. Perez-Victoria, [arXiv:1107.2120 [hep-ph]].
- [40] S. Jung, H. Murayama, A. Pierce, J. D. Wells, Phys. Rev. **D81**, 015004 (2010), [arXiv:0907.4112 [hep-ph]].
- [41] K. Cheung, W. -Y. Keung, T. -C. Yuan, Phys. Lett. **B682**, 287-290 (2009), [arXiv:0908.2589 [hep-ph]].
- [42] J. Shu, T. M. P. Tait, K. Wang, Phys. Rev. **D81**, 034012 (2010), [arXiv:0911.3237 [hep-ph]].
- [43] A. Arhrib, R. Benbrik, C. -H. Chen, Phys. Rev. **D82**, 034034 (2010), [arXiv:0911.4875 [hep-ph]].
- [44] I. Dorsner, S. Fajfer, J. F. Kamenik, N. Kosnik, Phys. Rev. **D81**, 055009 (2010), [arXiv:0912.0972 [hep-ph]].
- [45] V. Barger, W. -Y. Keung, C. -T. Yu, Phys. Rev. **D81**, 113009 (2010), [arXiv:1002.1048 [hep-ph]].
- [46] B. Xiao, Y. -K. Wang, S. -H. Zhu, Phys. Rev. **D82**, 034026 (2010), [arXiv:1006.2510 [hep-ph]].
- [47] K. Cheung, T. -C. Yuan, Phys. Rev. **D83**, 074006 (2011), [arXiv:1101.1445 [hep-ph]].
- [48] J. Shelton, K. M. Zurek, Phys. Rev. **D83**, 091701 (2011), [arXiv:1101.5392 [hep-ph]].
- [49] E. L. Berger, Q. -H. Cao, C. -R. Chen, C. S. Li, H. Zhang, Phys. Rev. Lett. **106**, 201801 (2011), [arXiv:1101.5625 [hep-ph]].
- [50] B. Grinstein, A. L. Kagan, M. Trott, J. Zupan, Phys. Rev. Lett. **107**, 012002 (2011), [arXiv:1102.3374 [hep-ph]].
- [51] K. M. Patel, P. Sharma, JHEP **1104**, 085 (2011). [arXiv:1102.4736 [hep-ph]].

- [52] N. Craig, C. Kilic and M. J. Strassler, Phys. Rev. D **84**, 035012 (2011) [arXiv:1103.2127 [hep-ph]].
- [53] Z. Ligeti, G. M. Tavares, M. Schmaltz, JHEP **1106**, 109 (2011). [arXiv:1103.2757 [hep-ph]].
- [54] S. Jung, A. Pierce, J. D. Wells, Phys. Rev. **D83**, 114039 (2011), [arXiv:1103.4835 [hep-ph]].
- [55] M. R. Buckley, D. Hooper, J. Kopp and E. Neil, Phys. Rev. D **83**, 115013 (2011) [arXiv:1103.6035 [hep-ph]].
- [56] A. E. Nelson, T. Okui, T. S. Roy, [arXiv:1104.2030 [hep-ph]].
- [57] M. Duraissamy, A. Rashed and A. Datta, Phys. Rev. D **84**, 054018 (2011) [arXiv:1106.5982 [hep-ph]].
- [58] J. Cao, K. Hikasa, L. Wang, L. Wu and J. M. Yang, [arXiv:1109.6543 [hep-ph]].
- [59] D. C. Stone and P. Uttayarat, [arXiv:1111.2050 [hep-ph]].
- [60] D. -W. Jung, P. Ko, J. S. Lee, S. -H. Nam, Phys. Lett. **B691**, 238-242 (2010), [arXiv:0912.1105 [hep-ph]].
- [61] J. Cao, Z. Heng, L. Wu, J. M. Yang, Phys. Rev. **D81**, 014016 (2010), [arXiv:0912.1447 [hep-ph]].
- [62] Q. -H. Cao, D. McKeen, J. L. Rosner, G. Shaughnessy, C. E. M. Wagner, Phys. Rev. **D81**, 114004 (2010), [arXiv:1003.3461 [hep-ph]].
- [63] D. -W. Jung, P. Ko, J. S. Lee, Phys. Lett. **B701**, 248-254 (2011), [arXiv:1011.5976 [hep-ph]].
- [64] D. -W. Jung, P. Ko, J. S. Lee and S. H. Nam, PoS **ICHEP2010**, 397 (2010) [arXiv:1012.0102 [hep-ph]].
- [65] D. Choudhury, R. M. Godbole, S. D. Rindani and P. Saha, Phys. Rev. D **84**, 014023 (2011) [arXiv:1012.4750 [hep-ph]].
- [66] C. Delaunay, O. Gedalia, Y. Hochberg, G. Perez and Y. Soreq, JHEP **1108**, 031 (2011) [arXiv:1103.2297 [hep-ph]].
- [67] M. I. Gresham, I. -W. Kim, K. M. Zurek, Phys. Rev. **D83**, 114027 (2011), [arXiv:1103.3501 [hep-ph]].
- [68] J. Shu, K. Wang, G. Zhu, [arXiv:1104.0083 [hep-ph]].

- [69] M. I. Gresham, I. W. Kim and K. M. Zurek, [arXiv:1107.4364 [hep-ph]].
- [70] S. Westhoff, [arXiv:1108.3341 [hep-ph]].
- [71] Edmond L. Berger, Qing-Hong Cao, Chuan-Ren Chen, Jiang-Hao Yu, Hao Zhang [arXiv:1111.3641 [hep-ph]].
- [72] M. I. Gresham, I. W. Kim and K. M. Zurek, Phys. Rev. D **84**, 034025 (2011) [arXiv:1102.0018 [hep-ph]].
- [73] J. Cao, L. Wang, L. Wu and J. M. Yang, Phys. Rev. D **84**, 074001 (2011) [arXiv:1101.4456 [hep-ph]].
- [74] K. Blum *et al.*, Phys. Lett. B **702**, 364 (2011) [arXiv:1102.3133 [hep-ph]].
- [75] J. A. Aguilar-Saavedra, M. Perez-Victoria, JHEP **1105**, 034 (2011), [arXiv:1103.2765 [hep-ph]].
- [76] J. L. Hewett, J. Shelton, M. Spannowsky, T. M. P. Tait and M. Takeuchi, Phys. Rev. D **84**, 054005 (2011) [arXiv:1103.4618 [hep-ph]].
- [77] J. A. Aguilar-Saavedra, M. Perez-Victoria, [arXiv:1105.4606 [hep-ph]].
- [78] J. A. Aguilar-Saavedra and M. Perez-Victoria, JHEP **1109**, 097 (2011) [arXiv:1107.0841 [hep-ph]].
- [79] S. Jung, A. Pierce and J. D. Wells, [arXiv:1108.1802 [hep-ph]].
- [80] D. Kahawala, D. Krohn and M. J. Strassler, [arXiv:1108.3301 [hep-ph]].
- [81] E. L. Berger, Q. H. Cao, J. H. Yu and C. P. Yuan, [arXiv:1108.3613 [hep-ph]].
- [82] B. Grinstein, A. L. Kagan, J. Zupan and M. Trott, JHEP **1110**, 072 (2011) [arXiv:1108.4027 [hep-ph]].
- [83] E. L. Berger, [arXiv:1109.3202 [hep-ph]].
- [84] A. Falkowski, G. Perez and M. Schmaltz, [arXiv:1110.3796 [hep-ph]].
- [85] A. Rajaraman, Z. Surujon and T. M. P. Tait, [arXiv:1104.0947 [hep-ph]].
- [86] ATLAS Collaboration, Technical Report ATLAS-CONF-2011-118, CERN, Geneva, Aug 2011.
- [87] CMS Collaboration, Phys. Rev. Lett. **107**, 091802 (2011) [arXiv:1106.3052 [hep-ex]].

- [88] V. Barger, W. Y. Keung and C. T. Yu, Phys. Lett. B **698**, 243 (2011) [arXiv:1102.0279 [hep-ph]].
- [89] CMS Collaboration, JHEP **1108**, 005 (2011) [arXiv:1106.2142 [hep-ex]].
- [90] ATLAS Collaboration, Technical Report ATLAS-CONF-2011-139, CERN, Geneva, Sep 2011.
- [91] J. Alwall *et al.*, JHEP **0709**, 028 (2007) [arXiv:0706.2334 [hep-ph]].
- [92] T. Sjostrand, S. Mrenna and P. Z. Skands, JHEP **0605**, 026 (2006) [arXiv:0603175 [hep-ph]].
- [93] P. Meade and M. Reece, [arXiv:0703031 [hep-ph]].
- [94] S. Olyn, X. Rouby and V. Lemaitre, [arXiv:0903.2225 [hep-ph]].
- [95] ATLAS Collaboration, ATLAS-CONF-2011-089, CERN, Geneva, Jun, 2011.
- [96] F. Caravaglios, M. L. Mangano, M. Moretti, R. Pittau, Nucl. Phys. **B539**, 215-232 (1999). [arXiv:9807570 [hep-ph]].
- [97] V. Ahrens, A. Ferroglia, M. Neubert, B. D. Pecjak and L. L. Yang, [arXiv:1103.0550 [hep-ph]].
- [98] Nikolaos Kidonakis. Phys. Rev. D, 82:114030, Dec 2010.

## Chapter 4

### Multi-Lepton GMSB Scenarios for Early LHC Running

#### 4.1 Introduction

In this note, we will outline several simple MSSM scenarios where a slepton is the next-to-lightest superpartner (NLSP) (1; 2; 3) within the context of General Gauge Mediation (GGM) (4; 5) including the special case of Gauge Mediation with Split Messengers. The slepton NLSP decays to its partner leptons plus a gravitino

$$\tilde{\ell} \rightarrow \ell + \tilde{G} \tag{4.1.1}$$

These scenarios can be used to explore the discovery potential of searches for multiple leptons in early LHC running.

In General Gauge Mediation, the MSSM soft parameters are essentially free at the messenger scale, subject to the following requirements: flavor universality, two sum rules for the sfermion masses, zero  $A$  terms, and gravitino LSP. In particular, there is not necessarily a hierarchy between colored states (squarks, gluinos) and uncolored states (wino, bino, higgsinos, sleptons). Thus there is no theoretical constraint on how light the colored states can be. So within GGM, relatively large production cross sections from compressed spectra provide the possibility of discovery even with very early LHC data. This should be contrasted with the more restrictive framework of Minimal Gauge Mediation (MGM) where colored states are always much heavier than the uncolored states, and therefore largely out of reach in early LHC running.

A simple framework in which light colored states and compressed spectra can arise is Gauge Mediation with Split Messengers (GMSM). In this straightforward generalization of MGM, the superpartner spectra are generally grouped in mass roughly into strongly and weakly interacting sets of superpartners. Over much of the parameter space the masses of both these groups can be comparable, yielding relatively compressed spectra with colored states not much heavier than weakly interacting states.

Given that final states with multiple high- $p_T$  leptons are generally clean discovery modes

for new physics, it is of special interest to investigate the possibilities for producing such signatures within the context of GGM and GSM. Multi-lepton final states arise most naturally in the subset of GGM and GSM parameter spaces where the right-handed sleptons are flavor-degenerate and at the bottom of the MSSM spectrum. These ‘slepton co-NLSPs decay 100% of the time to massless gravitino plus lepton, and so all events with MSSM production contain at least two high- $p_T$  leptons. Depending on the details of the heavier states in the spectrum, these leptons can be same sign or opposite sign, and there can be additional energetic leptons in the event (2; 3). In the case that a Bino-like neutralino is the next heavier superpartner above the slepton co-NLSP’s at least 4 leptons arise in each event (2; 3).

For the slepton co-NLSP scenario there is an huge multi-dimensional parameter space characterizing the remainder of the superpartner spectrum. Defining useable benchmarks within tractable parameter spaces therefore requires additional simplifying assumptions. The main motivation and focus here for early LHC searches is on compressed spectra with significant production cross section from strongly interacting superpartners. In the following sections, we will describe various interesting benchmark scenarios of this type. Scripts to generate the benchmarks defined here (as well as a wider class of generalizations) are described in section 4.3.

## 4.2 Benchmark Parameter Spaces

### 4.2.1 GSM Inspired Benchmark

For early LHC searches it is useful to utilize simple parameter spaces that reproduce the important features of superpartner spectra that arise from simple underlying models. Here we formulate a benchmark of this type inspired by GSM.

The GSM inspired scenario described here is defined to be right handed slepton co-NLSP, a gluino and (nearly) degenerate squarks, the Bino, Wino, and left handed sleptons. The Wino and gluino masses given by  $M_2$  and  $M_3$  respectively may be taken to be independent masses for a two parameter parameterization of this benchmark. The squark soft masses are taken to be degenerate with value  $m_{\tilde{q}}$  related to the gluino mass by

$$m_{\tilde{q}} = 0.8 M_3$$

The left-handed slepton masses, Bino, and right-handed slepton co-NLSP masses are related to the Wino mass by

$$m_{\tilde{\ell}_L} = 0.8 M_2$$



$$M_1 = 0.5 M_2$$

$$m_{\tilde{\ell}_R} = 0.3 M_2$$

All these ratios are close to those of GMSM with  $N = 5$  messenger generations. The squark and slepton mixings are defined to vanish. This approximates the small mixing that is obtained in most theories of low scale gauge mediation. All other soft parameters may be set to some large value such as 1.5 TeV. With both squarks and gluinos in the spectrum, the dominant strong production modes at the LHC are  $pp \rightarrow \tilde{q}\tilde{q}, \tilde{q}\tilde{g}$  with a smaller fraction of  $\tilde{g}\tilde{g}$ .

The inclusion of all these states with the relations given above gives a two-parameter space benchmark that interpolates between weak and strong production - this feature allows a comparison between existing Tevatron bounds (which are based on weak production) and early reach at the LHC from strong production. Starting from either weak or strong production, all cascade decays pass through the Bino and then the slepton co-NLSPs

$$\tilde{B} \rightarrow \ell^\pm \ell_R^\mp \rightarrow \ell^\pm \ell^\mp + \tilde{G} \quad (4.2.1)$$

So all supersymmetric events contain at least four leptons and missing energy

$$pp \rightarrow \ell^\pm \ell^\mp \ell'^\pm \ell'^\mp + X + MET \quad (4.2.2)$$

Starting from strong production  $X$  always includes jets. Some decay modes that pass through the Wino and left-handed sleptons include additional leptons. Promising search channels include tri-leptons  $+MET$  and four or more multi-leptons.

#### 4.2.2 Minimal Benchmark

For inclusive early LHC searches, it is also useful to formulate the minimal parameter space necessary for producing the signature of interest. For slepton co-NLSPs, this minimal parameter space consists of the slepton co-NLSP and the gluino, with all other superpartners decoupled. For convenience, we do not decouple the bino, but rather leave it intermediate between the sleptons and the gluino. Otherwise, the gluino decays are 4-body. We emphasize that this minimal parameter space also arises in physical models, since the entire GGM parameter space was covered by a perturbative messenger model in (5).

In more detail, we have:

- $\tilde{g}$ : the **gluino**. Gluino pair production provides the production mode, with rate set by the gluino mass. More generally, we could consider any configuration of colored sparticles, with an effective colored cross section. Any proposed search should be inclusive enough so as to be insensitive to the precise nature of these colored states.

- $\tilde{B}$ : the **bino**. The bino mass determines the amount of hadronic energy in the event, because, as discussed below, the gluino decays to the bino plus jets. We emphasize that a light bino is not necessary, but has the effect of drastically simplifying the branching fractions, while preserving most of the interesting physics.
- $\tilde{e}_R, \tilde{\mu}_R, \tilde{\tau}_1$ : the **slepton co-NLSPs**. These are the lightest states in the MSSM spectrum. They decay 100% of the time to their SM lepton superpartner plus massless gravitino.

With this simplified spectrum, the relevant parameters are the three masses:  $M_{\tilde{g}}$ ,  $M_{\tilde{B}}$ , and  $M_{\tilde{\ell}_R}$ . The branching fractions are not free parameters; we have

$$\tilde{g} \rightarrow \tilde{B} + jets \quad (4.2.3)$$

and

$$\tilde{B} \rightarrow (\tilde{e}_R^\pm, e^\mp), (\tilde{\mu}_R^\pm, \mu^\mp), (\tilde{\tau}_1^\pm, \tau^\mp) \quad (4.2.4)$$

with equal branching ratios (so 1/6 per final state). Finally, the slepton co-NLSPs always decay as:

$$\tilde{\ell}_R^\pm \rightarrow \ell^\pm + \tilde{G} \quad (4.2.5)$$

So with gluino pair production, the final states contain jets, two OSSF dilepton pairs (so, 4 leptons total, net charge zero), and missing energy from the gravitinos. Promising search channels should include same-sign dileptons+jets+ $MET$  and three or four leptons+jets+ $MET$ . We show the limit from the Tevatron (6) and the estimated reach at the early LHC within this minimal space.

### 4.3 Monte Carlo Simulations

Monte Carlo event simulation can be performed using PYTHIA in conjunction with a SUSY Les Houches Accord file containing a mass spectrum and decay table. Before generating events, the user needs to specify that PYTHIA should read information in from a SUSY Les Houches Accord file by setting the switch `IMSS(1)=11` and by pointing `IMSS(21-22)` to the relevant file. Additionally, for the GMSB scenario it is absolutely crucial that the user turns on gauge mediation and specifies the gravitino mass using the following PYTHIA switches:

$$\text{IMSS}(11)=1$$

$$\text{RMSS}(21)=m_{\tilde{G}}$$

where  $m_{\tilde{G}}$  is the gravitino mass in units of eV. For a prompt decay of the NLSP to the gravitino and its partner particle a canonical value of the supersymmetry breaking scale is 30 TeV which is equivalent to a gravitino mass of 0.2 eV. Setting `IMSS(11)=1` instructs PYTHIA that the lightest neutralino  $\tilde{\chi}_1^0$  should be taken to be the NLSP and that the gravitino  $\tilde{G}$  should be taken to be the LSP.

To generate a mass spectrum and decay table in SUSY Les Houches Accord format for the benchmark scenarios described above, we have included a package containing scripts that run a modified ISAJET kernel to calculate branching fractions. The package can be downloaded from the following location

`http://www.physics.rutgers.edu/~q1park/ISAGMSB.tar.gz`

Once the package has been downloaded, the user should unzip the package by typing the following into the command line:

`tar -zxvf ISAGMSB.tar.gz`

The user should then enter the folder `/ISAGMSB/` and type `make` into the command line. This will produce all of the machinery necessary to generate the SUSY Les Houches Accord files.

Included in the package is a script called `GMSBneut` which interactively takes user inputs, runs the ISAJET kernel, then saves the information in SUSY Les Houches Accord format. To run the script, the user should simply enter the `/ISAGMSB/` directory and type:

`./GMSBneut`

The user will first be prompted to enter a file name for the SUSY Les Houches Accord file. Five more input lines will then prompt the user to enter the Bino, Wino, and Gluino masses; the Higgsino mass  $\mu$ -parameter and  $\tan\beta$ ; the first and second generation slepton and squark masses; the third generation slepton and squark masses; and finally the gravitino mass. General neutralino and chargino mixing is calculated based on the input parameters. All masses should be entered in units of GeV, and multiple entries after an input prompt should be separated by a single space. All right and left handed sleptons and squark soft parameters are set equal to the input slepton and squark masses respectively internally in the script. Left-Right mixing for third generation sleptons and squarks is fixed internally to vanish. This feature allows a smooth decoupling of the Higgsino mass  $\mu$ -parameter while leaving squark and slepton spectra unaffected. With these assumptions all right handed sleptons are degenerate as are all left

handed sleptons, and all squarks are effectively degenerated except for the top squarks which have a mass squared given by  $m_t^2 = m_{\tilde{q}}^2 + m_{\tilde{t}}^2$ . From these inputs and the assumptions detailed above, an slha output file is then created in /ISAGMSB/ for use with PYTHIA.

The following is an example of the command line prompts and how the commands should be formatted:

```
./GMSBneut
```

Input the name of the slha file to be generated, followed by [ENTER]:

```
testfile
```

Input M1, M2, M3 (Bino, Wino and Gluino masses) separated by single space, followed by [ENTER]:

```
120 240 500
```

Input Mu (Higgsino mass) and TANBETA, separated by single space, followed by [ENTER]:

```
1000 2
```

Input MeR, MeL, and MQ (Right and Left Handed Slepton and Squark Masses) separated by single space, followed by [ENTER]:

```
156 1000 650
```

Input MtauR, MtauL, MBR, MTR, MQ3 (Right and Left Handed Stau, Right handed Sbottom and Stop, and Sbottom-Stop doublet masses) separated by single spaces, followed by [ENTER]:

```
156 1000 650 650 650
```

Input MGRAV (Gravitino Mass in units of GeV in 1E-9 notation) separated by single spaces, followed by [ENTER]:

```
1E-9
```

This will produce a file called `testfile.slha` according to all of the above inputs.

## Bibliography

- [1] S. Dimopoulos, M. Dine, S. Raby and S. D. Thomas, “Experimental Signatures of Low Energy Gauge Mediated Supersymmetry Breaking,” *Phys. Rev. Lett.* **76**, 3494 (1996) [arXiv:hep-ph/9601367].
- [2] S. Dimopoulos, S. D. Thomas and J. D. Wells, *Nucl. Phys. B* **488**, 39 (1997) [arXiv:hep-ph/9609434].
- [3] R. L. Culbertson *et al.* [SUSY Working Group Collaboration], “Low scale and gauge mediated supersymmetry breaking at the Fermilab Tevatron Run II,” arXiv:hep-ph/0008070.
- [4] P. Meade, N. Seiberg and D. Shih, “General Gauge Mediation,” *Prog. Theor. Phys. Suppl.* **177**, 143 (2009) [arXiv:0801.3278 [hep-ph]].
- [5] M. Buican, P. Meade, N. Seiberg and D. Shih, “Exploring General Gauge Mediation,” *JHEP* **0903**, 016 (2009) [arXiv:0812.3668 [hep-ph]].
- [6] J. T. Ruderman and D. Shih, “Slepton co-NLSPs at the Tevatron,” arXiv:1009.1665 [hep-ph].

## Chapter 5

### Entropic Force And its Fluctuation in Euclidian Quantum Gravity

#### 5.1 Introduction

The thermodynamics of black hole has been studied for several decades since the discover of Hawking radiation (2). It reveals a deep connection between the structure and dynamics of space-time and laws of thermodynamics(3; 4; 5; 6; 7). And more recently, the work by Jacobson shows an explicit derivation from laws of thermodynamics to Einstein equation(8). The attempts to explain gravity as an emergent phenomena is based on the holographic principle (9; 10) . And AdS/CFT correspondence provides strong support and explicit examples on how thermodynamics of space-time can be related to thermodynamics of the dual system living on holographic screen(11; 12; 13; 14).

Recently, Verlinde (1) proposed a conjecture that the origin of gravity can be interpreted as entropy changing on the holographic screen, which can be explicitly expressed as

$$F\Delta x = T\Delta S \quad (5.1.1)$$

There are several assumptions required to realize his idea. Firstly, one imposes how entropy on elements of holographic screen changes when one moves the particle  $\Delta x$

$$\Delta S = 2\pi k_B \frac{mc}{\hbar} \Delta x \quad (5.1.2)$$

where the distance between particle and screen element should be smaller than the Compton wavelength of the particle. And this will imply the Unruh-like relation between temperature and acceleration

$$k_B T = \frac{1}{2\pi} \frac{\hbar a}{c} \quad (5.1.3)$$

Then to relate energy and temperature of the system, one imposes the equipartition of energy, see also (15)

$$E = \frac{1}{2} N k_B T \quad (5.1.4)$$

where  $N$  is the number of degree of freedom on the holographic screen as

$$N = \frac{Ac^3}{G\hbar} \quad (5.1.5)$$

With identifying the total energy  $E$  of the system living on holographic screen with the bulk energy inside the screen, one can derive the Newton gravitational force and Einstein equation.

There has been many papers following this conjecture(18; 19; 20; 21; 22; 23; 24; 25; 26; 27; 28; 29), and some other papers apply this idea into cosmology(30; 31; 32; 33), especially, (34) studies possible fluctuation seeds induced by thermal fluctuation on holographic screen during inflation.

(5.1.1) is the equation showing the most important point of the whole idea, one interprets the origin of gravitational force as the change of entropy on the holographic screen. However, to derive the correct expression for gravitational force or equation, one needs to impose several other conditions. How far can those imposed conditions go? In what circumstance do those conditions fail to work? Is the interpretation of gravity always correct or just a coincidence in some particular cases?

In section 2, we apply some basic concepts and relations obtained from AdS/CFT to study the entropic interpretation of gravity, leaving those potentially unsafe conditions along, one finds that only by imposing (5.1.1), one can obtain the correct expression of gravitational force for generic static spherically symmetric metric background. The derivation in this section is an analog to the calculation in polymer molecule system, which is used to motive entropic force in Verlinde's paper.

In section 3, we consider our method to derive entropic force in more details, and we find it has a good interpretation from gravitational side alone, without correspondence between gravity and field theory. The point of this section is following: if one interprets the derivation from gravity side along, the whole calculation is just generalized Euler-Lagrange equation. However, if one gives thermodynamic interpretation ( as quantities on holographic screen ) to each step during derivation as we did in section 2, one will automatically draw the conclusion that gravity as entropic force. Together the analysis in section 2, it provides a solid base for entropic force interpretation. Moreover, since our derivation can be done in a quite generic metric background, it could be a clue to find more explicit connections and understanding on thermodynamics of two systems.

In section 4, since the force can be interpreted as a quantity in thermodynamics, we go further step to study its thermal fluctuation. We find the thermal fluctuation  $\overline{F^2 - \bar{F}^2}$  is always positive. And for a point-like particle, the fluctuation is never larger than the real force. The

metrics of black hole in asymptotic flat and AdS space are taken as examples in this section.

## 5.2 Entropic Force in gauge/gravity duality

One of the main ideas in Verlinde's paper is to interpret the origin of gravity as the change of the entropy in the dual theory on holographic plane. Gauge/gravity correspondence provides us a natural and very-well understood place to test this idea. The change of entropy in field theory on the holographic screen of the bulk space should give the correct expression for gravitational force experienced by particles in bulk space.

In gauge/gravity duality, one has the identification between Euclidian action of the field theory and the Euclidian action from gravity. And this will be our starting point to see how change of entropy causes gravity.

Firstly, we consider the simplest case, one point-like particle moving in a fixed geometric background with black hole. And we need to assume that the gravity set-up has a dual theory on field theory side. The temperature of black hole in gravity side should be identified as the temperature of the field theory.

Suppose there is an external force acting on the point particle holding it fixed. From the boundary point of view, the black hole plays the role of heat bath, the point particle should be interpreted as a perturbation away from equilibrium in the bath. If there is no external force acting on the particle, the particle will fall into black hole, which is analog to the process that the perturbation is erased and gets equilibrium with heat bath. When there is force holding particle fixed outside horizon, this corresponds to an effective force keeping perturbation away from thermal equilibrium with the bath.

Now let us applying the similar analysis used in section 2 in Verlinde's paper (1) for polymer molecule system. We choose to use micro-canonical ensemble. Thus, the entropy of the whole system can be written as  $S(E + F_{ext}r_0, r_0)$ , where  $E$  is the total energy of black hole and particle (heat bath and molecule chain). Since in micro-canonical ensemble one has

$$\frac{d}{dr_0} S(E + F_{ext}r_0, r_0) = 0 \quad (5.2.1)$$

which implies

$$\frac{F_{ext}}{T} - \frac{\partial S}{\partial r_0} = 0 \quad (5.2.2)$$

The next thing to do is to find the expression for entropy from our gravitational set-up. To achieve that, one recalls that in gauge/gravity duality, the Euclidean action calculated from



gravity is identified as entropy of the dual field theory if one treats the system as micro-canonical ensemble. That provides a solid way to calculate entropy in (5.2.1). The Euclidean action of our gravitational set-up can be written as

$$I = I_{Grav} + I_{part} + I_{int} \quad (5.2.3)$$

where  $I_{Grav}$  is the Euclidean Einstein-Hilbert action of background metric.  $I_{part}$  is the contribution from the static particle outside black hole. And  $I_{int}$  is from the interaction which keeps particle fixed. One can easily see that, in micro-canonical ensemble,  $I_{int}$  will contribute the first term in (5.2.2), and  $(I_{Grav} + I_{part})$  contribute to the second term. So to calculate the expression for external force, one needs to do derivative on  $(I_{BG} + I_{part})$  respect to  $r_0$ .

The action of a point particle in general geometric background is proportional to the proper mass times the integral of its proper time

$$I_{part} = im \int d\lambda \quad (5.2.4)$$

We want to consider the particle fixed at some point. So one can write the coordinates of the particle as  $X^\mu = \{t, r_0, \theta_0, \phi_0\}$ .

Since we need the Euclidian action, so we take  $\lambda \rightarrow i\tau$ . And one has to give the correct range where Euclidian proper time  $\tau$  runs.

To find the range of  $\tau$ , one firstly recalls how temperature relates to the metric. Suppose one has a static spherically symmetric metric

$$ds^2 = -g_{tt}(r)dt^2 + g_{rr}(r)dr^2 + \dots \quad (5.2.5)$$

Here  $g_{tt}$  and  $g_{rr}$  are only functions of  $r$ , and  $\dots$  just the normal angular parts of the metric. After taking  $t \rightarrow it$ , one finds  $t$  has to have period as

$$\beta = \frac{1}{T} = \frac{4\pi}{\sqrt{g'_{tt}(r)(\frac{1}{g_{rr}(r)})'|_{r=r_h}}}$$

where we set  $k_B$  to 1,  $T$  is identified as temperature of the system, and  $r_h$  is the position of horizon.

This is the period of coordinate time  $t$ , and it differs with particle's proper time  $\tau$  by a factor of  $\sqrt{g_{tt}}$ . Thus one has

$$I_{part} = -m \frac{\sqrt{g_{tt}}}{T} \quad (5.2.6)$$

Here we neglect the back reaction from the particle to background metric. This is corresponding to treat the heat bath, where the perturbation sits, infinitely large, and the small

variation of the perturbation is infinitesimal respect to whole system. Then  $I_{Grav}$  actually has no dependence on the position of particle. Now one can study how entropy changes respect to  $r_0$

$$\Delta S = \frac{\partial I_{part}}{\partial r_0} \Delta r_0 = -\frac{m}{2} \frac{\partial_{r_0} g_{tt}}{\sqrt{g_{tt}} T} \Delta r_0 \quad (5.2.7)$$

Now applying Verlinde's conjecture, taking the origin of gravitational force as the change of entropy in dual theory, one has, in a covariant form,

$$F_a = T \nabla_a S \quad (5.2.8)$$

Before going into calculation, several points needs to be clear. The definitions of work and force need to be clarified. There are two sets of coordinates describing the system, so one needs to choose the coordinates very carefully.

To motivate our choices of coordinates, let us briefly review the definition of work and force in special relativity. In special relativity, one also has two sets of coordinates, the proper  $(\tau, \vec{l})$  and observer  $(t, \vec{x})$  coordinates. One defines work as

$$W = \int_{x_0}^{x_1} \vec{F} \cdot d\vec{x} \quad (5.2.9)$$

and force is defined as

$$F^i = \frac{dp^i}{dt} = \sqrt{g_{tt}} \frac{d}{d\tau} (m_0 \frac{dx^i}{d\tau}) \quad (5.2.10)$$

Notice according to definition, force showed up here is *not* a 4-vector, and the upper subscript  $i$  on  $F$  is coming from  $x^i$ . Now one can write the generalized definition for work in a general background metric.

With background metric, one also has two sets of coordinates, one set is used to describe the field theory side  $(\tau, \vec{l})$  which should be interpreted as proper coordinates, another set is used in gravity theory side  $(t, \vec{x})$ , which is analog to observer coordinates in special relativity. Thus one can write down the definition of work in general background metric as

$$W = \int_{x_0}^{x_1} F_i dx^i = \int_{x_0}^{x_1} g_{ij} F^i dx^j \quad (5.2.11)$$

And in our case, we only care the radial component, thus we have

$$\Delta W = F_r \Delta r = g_{rr} F^r \Delta r = g_{rr} \sqrt{g_{tt}} \frac{d}{d\tau} (m_0 \frac{dr}{d\tau}) \Delta r \quad (5.2.12)$$

Now we can plug (5.2.7) and (5.2.12) into (5.2.8) and find the expression of the force as

$$m_0 \frac{d^2 r}{d\tau^2} = -\frac{m_0}{2} \frac{1}{g_{tt} g_{rr}} \partial_{r_0} g_{tt} \quad (5.2.13)$$

Since the particle is static, the external force should be balanced by gravitational force. And from (5.2.2), this force emerges from the changing of entropy of the dual system on holographic screen. If the entropic force interpretation is correct, one should get the same answer as one gets from geodesic equation. From the  $r$  component of geodesic equations, one has

$$\frac{d^2 r}{d\tau^2} + \frac{1}{2} \Gamma_{\mu\nu}^r \frac{dX^\mu}{d\tau} \frac{dX^\nu}{d\tau} = F_{ext} \quad (5.2.14)$$

$F_{ext}$ , again, is the external force keeping the particle fixed at  $r_0$ . Since the particle is not moving on radial direction, and the external force is balanced by gravitational force, one gets

$$F_{Grav} = m \frac{d^2 r}{d\tau^2} = -F_{ext} = -\frac{m}{2} \frac{1}{g_{tt}g_{rr}} \partial_{r_0} g_{tt} \quad (5.2.15)$$

which is exactly the same expression as the gravitational force calculated from entropic force interpretation using the thermodynamic language on holographic screen.

In the derivation, starting from micro-canonical ensemble,  $F_a = T \nabla_a S$  is the only formula we use, it does not depend on other assumptions, such as equipartition of energy. So this is a very safe check on the idea about the entropic origin of gravity. And one can claim that gravity always points to the direction to increase the system entropy, which leads the phenomena that gravity is always attractive.

### 5.3 Understanding Entropic Force From Gravity Side Alone

In previous section we have seen how entropic force interpretation in dual field theory gives the correct expression for gravity in bulk. In this section, we will consider our derivation again but interpret only from gravity side alone, without any knowledge about dual description on holographic screen.

The way we work in last section is firstly to write down the total action, then identify it with the entropy in field theory side. Taking the expression for black hole temperature, and applying (5.1.1), one can derive the expression for gravity.

Now let us firstly forget about the field theory interpretation, and only consider the point-like particle in background metric. Instead of writing the Polyakov point particle action, we write it in Nambu-Goto form as

$$I_{part} = im \int d\lambda \sqrt{\dot{X}_\mu \dot{X}^\mu} \quad (5.3.1)$$

For a particle fixed at some point, after gauge fixing  $\lambda$  as particle's proper time, the action just reduces to Polyakov point particle action.

Again, since the particle is in the heat bath by black hole, the Euclidian time direction, after taking  $\lambda \rightarrow i\tau$ , should be periodical.

Following the standard procedure in classical mechanics, consider a system whose action integration range is coordinate dependent

$$S = \int_0^{f(q)} d\tau (L_{part}[q, \dot{q}] + L_{int}[q]) \quad (5.3.2)$$

here  $q$  is the canonical coordinate and  $\dot{q} = dq/d\tau$ ,  $L_{int}$  is the interaction term acting on the particle to keep it fixed, and it will give the term of  $F_{ext}$  in equation of motion. E.O.M. is given by functional derivative of  $q$  and  $\dot{q}$ . Thus one gets

$$\delta S = f(q) \frac{\partial L}{\partial q} - f(q) \frac{d}{d\tau} \frac{\partial L}{\partial \dot{q}} + \frac{\partial f(q)}{\partial q} L[q, \dot{q}] = 0 \quad (5.3.3)$$

In our case,

$$L_{part} = m \sqrt{\dot{X}_\mu \dot{X}^\mu} \quad (5.3.4)$$

and  $q$  is taken as  $r$ . Thus,

$$\frac{d}{d\tau} \frac{\partial L}{\partial \dot{r}} = g_{rr} \frac{d^2 r}{d\tau^2} \quad (5.3.5)$$

Taking (5.3.5) into (5.3.3), and notice in our case  $f(q) = \frac{\sqrt{g_{tt}}}{T}$ , one can again generate (5.2.15), which is what we expect.

We can see that, the same calculation procedure, from gravity side point of view without knowledge anything about dual description, is just solving the generalized Euler-Lagrange equation. The point here is that the normal gravity calculation can be reinterpreted in the language of thermodynamic variables on the holographic screen, where gravity can be treated as change of entropy from dual theory point of view. The concept of gravity as entropic force just comes out naturally if the correspondence between gravity and field theory is set up and interpreted correctly.

## 5.4 Thermal Fluctuation

In the previous sections, we checked the entropic interpretation of gravitational force in the language of thermodynamics variables on holographic screen. And since we interpret the force as a thermodynamic quantity, we can push this idea one more step to study the fluctuation of gravitational force. In our set-up,  $F_{Grav}$  and  $r_0$  are analog to pressure and volume in dual field theory side. And since the particle is held by external force and the system is in equilibrium, one is allowed to use normal thermodynamics analysis to do calculation. Since we are interested in the fluctuation of the force acting on the particle, i.e. the fluctuation of the gravitational

force, we can treat  $(I_{Grav} + I_{part})$  as the partition function of the system. One can consistently find that the first derivative of partition function respect to  $r_0$  does give the correct expression for external force, which is the standard way to calculate pressure in normal thermodynamic analogy.

Let us first do some analysis on fluctuation in usual statistical system. Partition function of the system can be written as

$$Z = \sum_s e^{-\beta E_s} \quad (5.4.1)$$

External force  $Y$ , by definition, is

$$Y = \frac{\partial E_s}{\partial y} \quad (5.4.2)$$

$y$  is the extensive quantity corresponding to  $Y$ , so

$$\bar{Y} = \frac{\sum_s \frac{\partial E_s}{\partial y} e^{-\beta(E_s)}}{Z} \quad (5.4.3)$$

Then the fluctuation of  $Y$  can be derived as

$$\overline{Y^2} - \bar{Y}^2 = \frac{1}{\beta^2} \frac{\partial^2}{\partial y^2} \ln Z + \frac{1}{\beta} \frac{\partial \bar{Y}}{\partial y} \quad (5.4.4)$$

If the system is adiabatic and in equilibrium, one has

$$\frac{\partial^2 E}{\partial y^2} = \frac{\partial \bar{Y}}{\partial y} = \frac{\partial \bar{Y}}{\partial y} \quad (5.4.5)$$

Now, come back to our analysis, we identify  $Y$  with  $F$  in (5.2.8),  $y$  with  $r_0$  and  $\ln Z$  with Euclidian action  $I$ . Then we have

$$\overline{F^2} - \bar{F}^2 = \frac{1}{\beta^2} \frac{\partial^2}{\partial r_0^2} I + \frac{1}{\beta} \frac{\partial \bar{F}}{\partial r_0} \quad (5.4.6)$$

The set-up of our system is a point particle fixed at a point in some generic metric background, so it is an adiabatic system in equilibrium. Thus we can apply (5.4.5).

After some derivations, one gets a simple formula

$$\overline{F^2} - \bar{F}^2 = Tm \frac{(\partial_{r_0} \sqrt{g_{tt}})^2}{\sqrt{g_{tt}}} = \frac{T}{m\sqrt{g_{tt}}} \bar{F}^2 \quad (5.4.7)$$

One can see that (5.4.7) is always positive. We will study (5.4.7) in some more details in following sections.

### 5.4.1 Asymptotic AdS space with black hole

Since the duality between AdS space with Schwarzschild black hole and the CFT with finite temperature is one of the most understood examples in AdS/CFT, we take the explicit metric

of that case into calculation. And also we take the near horizon limit of the metric. Thus we have, for example in  $AdS_4$

$$g_{tt} = \left( \frac{r^2}{l^2} - \frac{2GM}{r} \right) \quad (5.4.8)$$

which gives

$$\frac{\overline{F^2} - \bar{F}^2}{\bar{F}^2} = \frac{T}{m \sqrt{\frac{r^2}{l^2} - \frac{2GM}{r}}} \quad (5.4.9)$$

Notice that the force we discuss here is not the conventional gravitational force experienced by particle in AdS space, i.e.  $F_G = m \frac{d^2 r}{dt^2}$ , they are proportional to each other by a coefficient as function of background metric at  $r_0$ .

The particle should be outside of black hole, so  $r > \sqrt[3]{2Gl^2M}$ , so ratio is always finite outside the black hole, it will blow up at black hole horizon and goes to zero when  $r$  goes to infinity. Then one needs to find the point where the ratio becomes one, which implies the fluctuation is larger than the average value of gravitational force.

If the point where ratio becomes to one is close to black hole horizon, then there is nothing to worry about, since the particle will experience the heat radiation from black hole which naturally cause large fluctuation. The only dangerous case is that point is far away from black hole horizon, which is counter-intuitive and may potentially contradict with experiments. Let us talk about this possibility carefully.

Since we only care about the point where ratio equals to one is far away from horizon, we can take  $r^3 \gg 2Gl^2M = r_{BH}^3$ , then (5.4.9) approximately becomes

$$\frac{\overline{F^2} - \bar{F}^2}{\bar{F}^2} = \frac{Tl}{mr} \quad (5.4.10)$$

Using the expression for black hole temperature  $T \sim \frac{(GM^2)^{1/3}}{l^{4/3}}$  and the radius of black hole  $R_{BH} \sim (GMl^2)^{1/3}$ , one finds

$$lm_0 \sim \frac{l}{\lambda} \sim \left( \frac{r_{BH}}{r_{O(1)}} \right) \quad (5.4.11)$$

where  $r_{O(1)}$  is the radial position where the ratio becomes order one, and  $\lambda$  is the Compton wavelength of the particle with mass  $m_0$ .

From (5.4.11), if the equal ratio point is far away from black hole horizon, which means  $r_{O(1)} \gg r_{BH}$ , then it requires  $\lambda \gg l$ . But we know that the particle with Compton wavelength larger than AdS radius cannot be well approximately described by a point-like particle. This is against our analysis using Polyakov point particle action. Thus, within a self-consistent analysis, one finds the fluctuation experienced by a point like particle can never dominate the real force, and this can be treated as a consistency check of our analysis.

Also here is another point needs to be clear. One requires the Compton wavelength of particle to be smaller than AdS radius to use point particle as approximation. This is not inconsistent with the treatment as neglecting the back-reaction from particle to background metric. To get a stable black hole in AdS space, one needs to take  $M_{BH} \gg \frac{1}{l}$ . As long as the mass of particle is much smaller compared to black hole mass, our approximation is safe.

### 5.4.2 Asymptotic flat space with black hole

The result from (5.4.9) is very interesting in the case of flat space with black hole, the ratio between fluctuation and the value of gravitational force goes to a constant!

$$\frac{\overline{F^2} - \bar{F}^2}{\bar{F}^2} = \frac{T}{m} \quad (5.4.12)$$

$m$  again shows up in the dominator. However, just like the previous case, the ratio only becomes bigger than one for a particle whose Compton wavelength larger than  $R_{BH}$ . And it is against our initial set-up.

We recover the units of quantities, we have

$$\frac{\overline{F^2} - \bar{F}^2}{\bar{F}^2} = \frac{k_B T}{mc^2} \quad (5.4.13)$$

We see that even when ratio goes to one in (5.4.12), the fluctuation comparing with the real value of force is still extremely small. However this small number sheds light on an experimental verification on the idea of entropic force.

## 5.5 Discussion

In this paper, we study Verlinde's conjecture, gravitational force is induced by the change of entropy of dual field theory on holographic screen. Instead of applying other potentially dangerous assumptions, we take the idea from gauge/gravity duality, identifying the Euclidian action of gravity and field theory. We calculate the action of a point-like particle held fixed in a static metric background with black hole. Taking black hole's temperature as the temperature of the dual system, we get the expression of the force induced by entropy change when we move the particle along radial direction. The entropic force derived this way agrees with the gravitational force in such background metric. Thus, this is a very safe check on the idea about gravity as emergent phenomena.

The key formula (5.1.1) is motivated from thermodynamics of the dual field theory. To give a more clear picture on how thermodynamics of gravity is related to that of the dual field

theory, we study the gravity interpretation of (5.1.1). We did a similar calculation as entropic force in previous section, however we kept our interpretation in language of gravity side. We find  $F_a = T\nabla_a S$  is just corresponding to a generalized Euler-Lagrange equation in gravity side. This gives an intuitive answer on why (5.1.1) gives the correct formula for gravitational force, and provide a solid base for entropic force interpretation. From this section, if one sticks on the language of thermodynamics on holographic screen to describe the system, one can naturally claim gravity is induced by the entropy change on the dual field theory.

After checking and giving a more explicit explanation on the entropic force, we take a further step to study the fluctuation of gravitational force in our formalism. we find the fluctuation in that metric is always positive. We take two widely used metrics, as examples. We find that, for a point-like particle, the fluctuation will never dominate the real value of gravitational force outside black hole. And for asymptotic flat metric with black hole, the ratio between fluctuation and force goes to a constant at infinity. This phenomena might provide a clue to experimentally test the concept of entropic force, or even holographic principle.



## Bibliography

- [1] E. P. Verlinde, On the Origin of Gravity and the Laws of Newton. arXiv:1001.0785 [hep-th].
- [2] Hawking, S. W. (1974). "Black hole explosions?". Nature 248 (5443):30
- [3] J. D. Bekenstein, Phys. Rev. D **7**, 2333 (1973).
- [4] J. M. Bardeen, B. Carter and S. W. Hawking, Commun. Math. Phys. **31**, 161 (1973).
- [5] S. W. Hawking, Commun. Math. Phys. **43**, 199 (1975) [Erratum-ibid. **46**, 206 (1976)].
- [6] P. C. W. Davies, J. Phys. A **8**, 609 (1975).
- [7] W. G. Unruh, Phys. Rev. D **14**, 870 (1976).
- [8] T. Jacobson, Phys. Rev. Lett. **75**, 1260 (1995) [arXiv:gr-qc/9504004].
- [9] G. 't Hooft, arXiv:gr-qc/9310026.
- [10] L. Susskind, J. Math. Phys. **36**, 6377 (1995) [arXiv:hep-th/9409089].
- [11] J. M. Maldacena, Adv. Theor. Math. Phys. **2**, 231 (1998) [Int. J. Theor. Phys. **38**, 1113 (1999)] [arXiv:hep-th/9711200].
- [12] S. S. Gubser, I. R. Klebanov and A. M. Polyakov (1998). "Gauge theory correlators from non-critical string theory". Physics Letters B428: 105C114
- [13] Edward Witten (1998). "Anti-de Sitter space and holography". Advances in Theoretical and Mathematical Physics 2: 253C291. <http://arxiv.org/abs/hep-th/9802150>.
- [14] L. Susskind and E. Witten, "The holographic bound in anti-de Sitter space". arXiv:hep-th/9805114.
- [15] T. Padmanabhan, "Thermodynamical Aspects of Gravity: New insights". arXiv:0911.5004 [gr-qc].
- [16] L. Smolin, "Newtonian gravity in loop quantum gravity". arXiv:1001.3668 [gr-qc].

- [17] F. W. Shu and Y. Gong, “Equipartition of energy and the first law of thermodynamics at the apparent horizon”. arXiv:1001.3237 [gr-qc].
- [18] C. Gao, “Modified Entropic Force”. arXiv:1001.4585 [hep-th].
- [19] Y. Zhang, Y. g. Gong and Z. H. Zhu, “Modified gravity emerging from thermodynamics and holographic principle”. arXiv:1001.4677 [hep-th].
- [20] J. W. Lee, H. C. Kim and J. Lee, “Gravity from Quantum Information”. arXiv:1001.5445 [hep-th].
- [21] Y. S. Myung, “Entropic force in the presence of black hole”. arXiv:1002.0871 [hep-th].
- [22] J. Kowalski-Glikman, “A note on gravity, entropy, and BF topological field theory”. arXiv:1002.1035 [hep-th].
- [23] Y. X. Liu, Y. Q. Wang and S. W. Wei, “Temperature and Energy of 4-dimensional Black Holes from Entropic Force”. arXiv:1002.1062 [hep-th].
- [24] R. G. Cai, L. M. Cao and N. Ohta, “Notes on Entropy Force in General Spherically Symmetric Spacetimes”. arXiv:1002.1136 [hep-th].
- [25] F. Caravelli and L. Modesto, arXiv:1001.4364 [gr-qc].
- [26] Y. Tian and X. Wu, “Thermodynamics of Black Holes from Equipartition of Energy and Holography”, arXiv:1002.1275 [hep-th].
- [27] Y. S. Myung and Y. W. Kim, “Entropic force and entanglement system”, arXiv:1002.2292 [hep-th].
- [28] I. V. Vancea and M. A. Santos, “Entropic Force Law, Emergent Gravity and the Uncertainty Principle”, arXiv:1002.2454 [hep-th].
- [29] R. A. Konoplya, “Entropic force, holography and thermodynamics for static space-times”, arXiv:1002.2818 [hep-th].
- [30] R. G. Cai, L. M. Cao and N. Ohta, “Friedmann Equations from Entropic Force”. arXiv:1001.3470 [hep-th].
- [31] M. Li and Y. Wang, “Quantum UV/IR Relations and Holographic Dark Energy from Entropic Force”. arXiv:1001.4466 [hep-th].

- [32] S. W. Wei, Y. X. Liu and Y. Q. Wang, “Friedmann equation of FRW universe in deformed Horava-Lifshitz gravity from entropic force”. arXiv:1001.5238 [hep-th].
- [33] Y. Ling and J. P. Wu, “A note on entropic force and brane cosmology”. arXiv:1001.5324 [hep-th].
- [34] Y. Wang, “Towards a Holographic Description of Inflation and Generation of Fluctuations from Thermodynamics”. arXiv:1001.4786 [hep-th].

## Chapter 6

### Metastable Spontaneous SUSY Breaking in a Landscape of Fuzzy Droplets

#### 6.1 Introduction

$N = 1$  SUSY QCD has very rich structures in moduli space. It has been studied by (1; 2; 3; 4; 5; 6; 7; 8; 9; 10; 11; 12). Further, a chiral superfield  $\phi$  in adjoint representation has been added, named as  $N = 1$  adjoint SQCD, where more interesting features present(13; 14; 15; 16; 17; 18).

In this chapter, a class of  $\mathcal{N} = 1$  supersymmetric theories with gauge group  $U(N_c)$  and chiral multiplet matter in the adjoint representation along with  $N_f$  flavors of fundamental plus anti-fundamental is analyzed. With non-vanishing Fayet-Iliopoulos and matter field mass terms, these theories are shown to have a landscape of metastable vacua with spontaneously broken supersymmetry. The adjoint field configurations in the local metastable vacua are non-commutative, and may be interpreted as a fluid consisting of fuzzy droplets in a confining potential. The analogy between noncommutative gauge theory and noncommutative description of fluids using the Lagrange particle coordinates has been proposed and studied by(19; 20; 21; 22; 23; 24; 25) . The excited states of the meta-stable vacua may be interpreted as excitations of the fuzzy fluid droplets. The number of metastable vacua is exponentially large in the product of the gauge group rank and number of flavors. In the limit of large ratio of Fayet-Iliopoulos to mass terms, the lifetime of the metastable vacua become exponentially large in the inverse square of this ratio. The theories analyzed here could provide a simple analog model for a landscape of metastable vacua that may arise in certain classes of string or M-theory compactifications with blown-up branes dissolved inside branes.

#### 6.2 The model

The model consists of an  $N = 1$  supersymmetric  $U(N_c)$  gauge theory. In addition, we have the matter fields  $\phi$ , which transforms in the adjoint representation, the quarks  $Q_i$  and the antiquarks  $\tilde{Q}_i$ , in the fundamental representation with flavor  $i = 1, \dots, N_f$ . Thus the Lagrangian can be

written as

$$L = \int d^4\theta \text{Tr}[\phi^\dagger e^V \phi e^{-V} + \sum_{i=1}^{N_f} (Q_i^\dagger e^V Q_i + \tilde{Q}_i^\dagger e^{-V} \tilde{Q}_i)] + 2\zeta \int d^4\theta \text{Tr}(V) + \mathcal{L}_m + \mathcal{L}_{int} \quad (6.2.1)$$

where

$$\begin{aligned} \mathcal{L}_m &= \frac{1}{2} m_\phi \text{Tr} \phi^2 + m_{Q_i}^2 \text{Tr} Q_i \tilde{Q}_i \\ \mathcal{L}_{int} &= \sqrt{2} h \text{Tr} \tilde{Q}_i \phi Q \end{aligned}$$

$2\zeta \int d^4\theta \text{Tr}(V)$  is the F-I term which is used to break SUSY spontaneously if mass term is turned on, and it will spontaneously break the  $U(N_c)$  gauge symmetry when mass terms are vanishing or small.

We divide the discussion into two parts, without and with mass term, and we will not get into the discussion for  $\mathcal{L}_{int}$  turned on.

### 6.3 Model without mass terms

#### 6.3.1 Solutions for supersymmetric vacua

The D-term potential is written as

$$V_D = \text{Tr}([\phi^\dagger, \phi] + Q_i^\dagger Q_i - \tilde{Q}_i^\dagger \tilde{Q}_i + \zeta)^2 \quad (6.3.1)$$

Here  $\phi, Q_i$  and  $\tilde{Q}_i$  denote the scalar part of the corresponding fields. In matrix representation,  $\zeta$  is written as  $\zeta 1_{N_c \times N_c}$ .

The model is known to have a supersymmetric minimum (?) at

$$\begin{aligned} \phi &= \sqrt{\zeta} \begin{pmatrix} 0 & \sqrt{1+q} & & & \\ & 0 & \sqrt{2+q} & & \\ & & \ddots & \ddots & \\ & & & 0 & \sqrt{N_c-1+q} \\ & & & & 0 \end{pmatrix} \\ Q_1 &= \sqrt{\zeta} \begin{pmatrix} \sqrt{q} & \cdots & 0 \end{pmatrix} \\ \tilde{Q}_1 &= \sqrt{\zeta} \begin{pmatrix} 0 & \cdots & 0 & \sqrt{N_c+q} \end{pmatrix} \end{aligned}$$

where we take  $N_f = 1$ . We can define noncommunicative coordinates as  $X = \frac{\phi + \phi^\dagger}{\sqrt{2}}$  and  $Y = \frac{\phi - \phi^\dagger}{i\sqrt{2}}$ . Taking  $q = 0$ , the solution above is corresponding to a 2D disk with radius  $\sqrt{2N_c + 1}$ . In condense matter language, this describes the condensation of electrons forming a 2D noncommunicative droplet. And in D-brane's language, this solution is corresponding to

$N_c$  D0-branes diffusing on a D2-brane, which will contribute magnetic flux to D2-brane. For  $q \neq 0$ , it describes a ring whose inner and outer radii are  $\sqrt{q}$  and  $\sqrt{2N_c + q + 1}$ .

For the case of  $N_f > 1$ , e.g.  $N_1 = 2, N_2 = 3$ , one gets:

$$\begin{aligned} \phi &= \sqrt{\zeta} \begin{pmatrix} 0 & \sqrt{1} & & & \\ 0 & 0 & & & \\ & & 0 & \sqrt{1} & 0 \\ & & 0 & 0 & \sqrt{2} \\ & & 0 & 0 & 0 \end{pmatrix} \\ Q_1 &= \sqrt{\zeta} \begin{pmatrix} 0 & 0 & 0 & 0 & 0 \end{pmatrix} \\ \tilde{Q}_1 &= \sqrt{\zeta} \begin{pmatrix} 0 & \sqrt{2} & 0 & 0 & 0 \end{pmatrix} \\ Q_2 &= \sqrt{\zeta} \begin{pmatrix} 0 & 0 & 0 & 0 & 0 \end{pmatrix} \\ \tilde{Q}_2 &= \sqrt{\zeta} \begin{pmatrix} 0 & 0 & 0 & 0 & \sqrt{3} \end{pmatrix} \end{aligned}$$

This describes 2 droplets, of size  $\sqrt{5}$  and  $\sqrt{7}$ , laying on each other. The diagonal blocks describe the motion in each disk, and the off-diagonal blocks describe the interaction between the two disks.

There are also other classes of solutions. For the model without mass terms, the infinitesimal transformation,  $\phi' = \phi + \epsilon \phi^{\dagger n}$  ( $n \in [0, N_c - 1]$ ), also describes one of supersymmetric vacua. From the definition of coordinates (also from the viewpoint of operator parameterizing moduli space which will be discussed later), those solutions describe the ripples on the disk. For example,  $n = 0$  is for parallel transformation, and  $n = 1$  is corresponding to the ellipse.

### 6.3.2 Moduli space

The  $U(N_c)$  gauge group is completely broken. The moduli space with  $N_f \geq 1$  has complex dimension

$$\dim_C(N_{N_f}) = 2N_f N_c$$

In this paper, we only discuss the operators describing moduli space for  $N_f = 1$  case. Moduli space can be parameterized by following chiral operators (?):

$$Tr(\phi^k) \tag{6.3.2}$$

$$\tilde{Q} \phi^{k-1} Q \tag{6.3.3}$$

where  $k = 1, \dots, N_c$

There is a correspondence between those operators and directions in moduli space which vanish D-term potential. We will discuss it in detail when we turn on the mass term in Lagrangian.

### 6.3.3 The spectrum

The  $U(N_c)$  gauge symmetry is spontaneously broken by  $\phi$ ,  $Q$  and  $\tilde{Q}$  background, so the  $2(N_c \times N_c + 2N_c)$  real scalar d.o.f play the role of Higgs.  $N_c^2$  real degrees of freedom are eaten by the gauge bosons (each Lorentz component of vector field is an  $N_c \times N_c$  Hermitian matrix which has  $N_c^2$  d.o.f). Another  $N_c^2$  d.o.f are lifted to be massive modes, and they have the same mass spectrum as gauge bosons in F-I mechanism if the mass Lagrangian is turned off. The left  $4N_c$  d.o.f are massless which are corresponding to moduli space.

Let us talk about the massive modes first. An easy way to calculate the massive modes is to calculate the spectrum of gauge bosons, because they share the same masses with massive scalars. The Lagrangian which gives masses to gauge bosons is proportional to

$$Tr[\phi^\dagger A A \phi + \phi^\dagger \phi A A - 2\phi^\dagger A \phi A] + Q^\dagger A A Q + \tilde{Q} A A \tilde{Q}^\dagger \quad (6.3.4)$$

Here  $A \equiv A^\mu$ . The spectrum of gauge bosons shows several structures:

1. There are  $N_c$  singlet states and  $N_c(N_c - 1)$  doublet states in the spectrum. So in total, we have  $N_c^2$  d.o.f.
2. The eigenvectors for singlet states are the excitations of elements on diagonal line. And eigenvectors for doublet states are the excitations along the line parallel to the diagonal line. (It is easy to understand. Because  $A$  is Hermitian, the elements on diagonal line can only be real, so they will give singlets. And the complex elements on off-diagonal lines will give doublets.)
3. We can group the eigenvalues by the line their eigenvectors belonging to. And for the  $n$ th eigenvalue on the line  $m$  units away from the diagonal line, one can find that the eigenvalues are approximately equal to  $J[m, n]/(2N + 1)$ , where  $J[m, n]$  is the  $n$ th zero solution for  $m$ th order BesselJ function. Thus

$$m^2 = J[m, n]^2 / (2N + 1)$$

This is the harmonic oscillation on the 2D round surface with Dirichlet boundary condition. And from formula for eigenvalues that the radius of the disk is  $\sqrt{2N + 1}$ . Singlet states are corresponding to  $m = 0$ , doublet states are  $m \neq 0$ . The derivation between eigenvalues and the numbers from Bessel function increases with  $m$  and  $n$ , but decrease with  $N_c$ .

Here we show a table where we can compare the eigenvalues from the mass matrix and Helmholtz equation with Dirichlet boundary condition.

| n | $m = 0$ Matrix | $m = 0$ Helmholtz | $m = 1$ Matrix | $m = 1$ Helmholtz | $m = 2$ Matrix | $m = 2$ Helmholtz |
|---|----------------|-------------------|----------------|-------------------|----------------|-------------------|
| 1 | 0.0288         | 0.0288            | 0.0734         | 0.0730            | 0.1325         | 0.1312            |
| 2 | 0.1516         | 0.1516            | 0.2461         | 0.2449            | 0.3561         | 0.3525            |
| 3 | 0.3726         | 0.3726            | 0.5176         | 0.5149            | 0.6787         | 0.6717            |
| 4 | 0.6919         | 0.6917            | 0.8879         | 0.8832            | 1.1006         | 1.0892            |
| 5 | 1.1096         | 1.1091            | 1.3572         | 1.3497            | 1.6220         | 1.6048            |
| 6 | 1.6258         | 1.6247            | 1.9255         | 1.9143            | 2.2430         | 2.2185            |

Table 6.1: Comparison between eigenvalues from mass matrix and Helmholtz equation with Dirichlet boundary condition, for  $N_c = 100$ .

We can explain it by claiming that the disk describing by equally separated lattice, which is not continuous. And we will show that explicitly later. So in the large  $N_c$  limit, one can expect that those two sets of numbers match exactly.

### 6.3.4 The explanation to the spectrum

The eigenvalues are obtained from the mass matrix of gauge bosons. So we expect to read off the Laplacian equation from observation of the matrix, and the matrix does show such kind of structure if we arrange the matrix carefully.

For the matrix representation of gauge boson, instead of naming matrix elements by row and column number, we name them by lines parallel to the diagonal line. The reason we use this way is from the third point mentioned at the end of last section, i.e. we can group the eigenvalues by the line their eigenvectors belonging to.

$$\begin{pmatrix} A_{1,1} & A_{2,1} & & & \\ A_{2,1}^* & A_{1,2} & A_{2,2} & & \\ & A_{2,2}^* & \ddots & \ddots & \\ & & \ddots & A_{1,N_c-1} & A_{2,N_c-1} \\ & & & A_{2,N_c-1}^* & A_{1,N_c} \end{pmatrix}$$

The benefit for this way to label the elements is that the mass matrix of gauge boson will be automatically separated into blocks along diagonal line, so we just need to analyze each block individually. To find the relation between Helmholtz equation and the mass matrix, we need to identify  $A_{m,j}$  as  $R_j^{(m)}$ , where  $R_j^{(m)}$  is the discretized radial part of the wavefunction, i.e.  $\psi = R^{(m)}(r)e^{\pm im\phi}$ , and  $r = \sqrt{2j+1}$ . (There is a subtle point of this identification. The radius of the disk is  $\sqrt{2N+1}$  for all values of  $m$ , but label  $j$  runs from 1 to  $(N_c - m)$ , so for large  $m$ , this identification does not work even approximately.)

Firstly, let us write down the discrete form of  $\psi \square^2 \psi$  on the lattice, this is the term in Lagrangian to describe the wave on the disk. One point needed to be mentioned is that the



coordinates in this Lagrangian is the coordinates in  $\phi$  and  $\phi^\dagger$  plane, not the coordinates used in Eq. (1). And we can solve the equation of motion as  $\square^2\psi = 0$ . Assuming that the disk is isotropic, so we can take  $\psi = R^{(m)}(r)e^{\pm im\theta}e^{i\omega t}$ , then  $\square^2\psi = 0$  goes to

$$\frac{1}{r} \frac{d}{dr} \left( r \frac{dR^{(m)}(r)}{dr} \right) - \frac{m^2}{r^2} R^{(m)}(r) + \omega^2 R^{(m)}(r) = 0$$

which is actually a problem to solve the eigenvalues of operator:  $\frac{1}{r} \frac{d}{dr} \left( r \frac{d}{dr} \right) - \frac{m^2}{r^2}$

Now assume the lattice is equally spaced 2D lattice, and we write  $R^{(m)}(r)$  as  $R_n^{(m)}$ , where  $n$  is the  $n$ th site away from the center of the disk. In the discussion, we treat  $n$  as a large number and do expansion by power of  $\frac{1}{n}$ , this limit treatment means we do not discuss the center of the disk where the continuum approximation broken down. Because the lattice is equally spaced, and according to the previous discussion of  $R^2$  matrix, we set radial distance as  $r = \sqrt{2n-1}$ . ( From now on we will drop index  $m$  for convenience. ) Firstly,  $\frac{1}{r} \frac{d}{dr} \left( r \frac{dR}{dr} \right) - \frac{m^2}{r^2} R$  can be written as

$$\frac{\frac{R_{n+1}-R_n}{\sqrt{2n+1}-\sqrt{2n-1}} - \frac{R_n-R_{n-1}}{\sqrt{2n-1}-\sqrt{2n-3}}}{\sqrt{2n-1}-\sqrt{2n-3}} + \frac{1}{\sqrt{2n-1}} \frac{R_n-R_{n-1}}{\sqrt{2n-1}-\sqrt{2n-3}} - \frac{m^2}{2n-1} R_n \quad (6.3.5)$$

Do the expansion by power of  $\frac{1}{n}$ , we get

$$2n(R_{n+1}-2R_n+R_{n-1}) + (4R_n-3R_{n-1}-R_{n+1}) + \frac{2R_n+R_{n-1}-3R_{n+1}-4m^2R_n}{8} \frac{1}{n} + O\left(\frac{1}{n^2}\right) \quad (6.3.6)$$

On the other hand, the mass matrix introduce the interaction between two nearby sites along radial direction, and they introduce the following terms in the Lagrangian:

$$R_n[\sqrt{(2n)2(n+m)}R_{n+1} - 2(2n-1+m)R_n + \sqrt{2(n-1)2(n-1+m)}R_{n-1}] \quad (6.3.7)$$

Similarly, we do the same  $\frac{1}{n}$  expansion to the mass matrix expression, and we get

$$2n(R_{n+1}+R_{n-1}-2R_n) + (2R_n-2R_{n-1}+m(R_{n+1}+R_{n-1}-2R_n)) - \frac{m^2}{4n}(R_{n+1}+R_{n-1}) \quad (6.3.8)$$

Subtract those two expansions, we can find the difference between them as

$$-(m+1)(R_{n+1}+R_{n-1}-2R_n) + \frac{1}{8n}[-2(R_{n+1}-R_{n-1}) + (2m^2-1)(R_{n+1}+R_{n-1}-2R_n)] \quad (6.3.9)$$

Let us analyze the difference order by order. On the zeroth order of  $\frac{1}{n}$ , the difference is  $-(m+1)(R_{n+1}+R_{n-1}-2R_n)$ . We can write  $(R_{n+1}+R_{n-1}-2R_n)$  in terms of differential operators as  $a^2 \frac{d^2 R}{dr^2}$ , where  $a$  is the space between two sites. Obviously, this term will vanish in continuum limit where we take  $N_c$  to infinity. For  $\frac{1}{n}$  order term, it is separated into two parts. The part proportional to  $(R_{n+1}+R_{n-1}-2R_n)$ , just like before, will vanish in continuum limit.

The other term proportional to  $R_{n+1} - R_{n-1}$ . This term can be written as  $a \frac{dR}{dr}$ , so it will vanish as well in continuum limit.

Thus, those two expressions match to each other in the continuum limit, this explains why the spectrum from mass matrix matches with the one from Helmholtz equation.

The boundary condition is left to be checked. To see how mass matrix shows Dirichlet boundary condition, let us firstly discuss one dimensional lattice case. There the interaction among sites can be written as

$$R_n[(R_{n-1} - R_n) - (R_n - R_{n+1})]$$

which is just the discretized form of  $R \frac{d^2 R}{dr^2}$ . Suppose we have  $N + 1$  sites along the lattice, and we take Dirichlet boundary condition, i.e. set  $R_{N+1} = 0$ , then the interaction of the last three sites is

$$R_N(R_{N-1} - 2R_N)$$

the matrix stops at  $N$ th element, and takes the form as

$$\begin{pmatrix} -2 & 1 & & & \\ 1 & -2 & 1 & & \\ & 1 & \ddots & \ddots & \\ & & \ddots & -2 & 1 \\ & & & 1 & -2 \end{pmatrix}$$

And for Neumann boundary condition, the last two sites always take the same value so that the derivative of the wavefunction vanishes at boundary. Thus, we can write the interaction among the last three points as

$$R_N(R_{N-1} - R_N)$$

And the matrix can be written as

$$\begin{pmatrix} -2 & 1 & & & \\ 1 & -2 & 1 & & \\ & 1 & \ddots & \ddots & \\ & & \ddots & -2 & 1 \\ & & & 1 & -1 \end{pmatrix}$$

Now come back to the mass matrix in our model, if we take radius of the disk very large, then the radial part of the Laplacian operator on the disk come to one dimensional lattice form, where the element on the diagonal line is twice as big as elements one step up or left, with a

minus sign. This asymptotic behavior of the mass matrix tells us that the boundary condition should be Dirichlet.

There is another rough way to show why the mass spectrum obeys the solution of harmonic oscillation on the disk. According to (26), there is invertible maps, Weyl-Wigner formalism, between operators and functions on a given manifold, a disk in our case. Then one has

$$\begin{aligned}\partial_z f &= \frac{1}{\theta} \langle z | [\hat{f}, \hat{a}^\dagger] | z \rangle \\ \partial_{\bar{z}} f &= \frac{1}{\theta} \langle z | [\hat{a}, \hat{f}] | z \rangle\end{aligned}$$

where

$$\hat{f} = \sum_{m,n} f_{mn} |\psi_m\rangle \langle \psi_n|$$

in density matrix notation, and

$$f(\bar{z}, z) = e^{|z|^2/\theta} \sum_{m,n} f_{mn} \frac{\bar{z}_m z_n}{\sqrt{m!n!\theta^{m+n}}}$$

So

$$\nabla^2 f(\bar{z}, z) \sim \langle z | [\hat{a}, [\hat{f}, \hat{a}^\dagger]] | z \rangle$$

Recall that  $\phi$  and  $\phi^\dagger$  in our model just play the role of vanishing and generating operators. And the gauge boson field  $A$  is corresponding to the function  $f$  on the fuzzy disk. One can check that the interaction Lagrangian between  $\phi$  and gauge boson  $A$  can be written as

$$\mathcal{L}_{int} \sim Tr(\hat{A}[\hat{\phi}, [\hat{A}, \hat{\phi}^\dagger]]) \quad (6.3.10)$$

Thus, this formulation provides a clue to build up the relation between Laplacian operator and gauge boson mass matrix on 2D fuzzy disk.

## 6.4 Model with mass terms

In this section, we will study the case where the mass terms are turned on

$$W = \frac{1}{2} m_\phi^2 Tr \phi^2 + m_Q^2 Tr Q_i \tilde{Q}_i$$

Thus SUSY is spontaneously broken by F-I mechanism. For the case of  $m_\phi, m_Q \gg \zeta$ , there is only one kind of vacuum which has  $V = \frac{1}{2} \zeta^2$ . It is not an interesting case because the characters of F-I term are all covered up by big mass terms. So we will be focus on the case of  $m_\phi, m_Q \ll \zeta$ , where the solution for  $m_\phi = m_Q = 0$  case is still an approximate solution.

Since we turn on the mass terms, the moduli directions are lifted, and the corresponding modes will not be massless any more, but having a small mass instead, in the limit of  $m_\phi, m_Q \ll \zeta$ .

### 6.4.1 One flavor case

Let us start from one flavor case. Up to quadratic order in the masses, there is a homogenous shift in all the fields as

$$X = [(1 - \frac{m_Q^2}{2\zeta})1 - \frac{m_\phi^2}{2\zeta}((N_c - 1)1 - \frac{1}{2\zeta}\phi_0^\dagger\phi_0)]X_0 \quad (6.4.1)$$

And potential will be

$$V = \frac{(N_c - 1)N_c}{2}m_\phi^2\zeta + N_cm_Q^2\zeta + \mathcal{O}(m^4) \quad (6.4.2)$$

We can calculate the mass spectrum for scalar fields  $\phi$ ,  $Q$  and  $\tilde{Q}$ . There are  $N_c^2$  heavy modes, of order  $\sqrt{\zeta}$ . Those are just the modes which are the same as the spectrum of gauge bosons. There are some light modes left in the spectrum of scalars. Those can be divided into two groups,  $\phi$  modes and  $Q$  modes which will be explained later:

$\phi$ -modes ripples

$$m^2 = km_\phi^2 + \mathcal{O}(m^4/\zeta) \quad (6.4.3)$$

$Q$ -modes

$$m^2 = (k - 1)m_\phi^2 + 2m_Q^2 + \mathcal{O}(m^4/\zeta) \quad (6.4.4)$$

where  $k$  runs from 1 to  $N_c$ . Studying the eigenvectors of those modes can be helpful for understanding them.

The fluctuation of  $\phi$ -modes can be written as, after being normalized to one,

$$a(\phi)_{i,j} = \sqrt{\zeta} \frac{\sqrt{\binom{j+k-2}{j-1}}}{\sqrt{\sum_{j=1}^{N_f-k+1} \binom{j+k-2}{j-1}}} \delta_{i-k,j} \quad (6.4.5)$$

where  $i$  and  $j$  are the labels for row and column. And there are no components in  $Q$  and  $\tilde{Q}$  turned on. For example, we take  $N_c = 6$  and  $k = 3$ , we can write the fluctuation for this mode as

$$\delta\phi = \sqrt{\zeta} \begin{pmatrix} 0 & 0 & 0 & 0 & 0 & 0 \\ 0 & 0 & 0 & 0 & 0 & 0 \\ \frac{1}{\sqrt{20}} & 0 & 0 & 0 & 0 & 0 \\ 0 & \frac{\sqrt{3}}{\sqrt{20}} & 0 & 0 & 0 & 0 \\ 0 & 0 & \frac{\sqrt{6}}{\sqrt{20}} & 0 & 0 & 0 \\ 0 & 0 & 0 & \frac{\sqrt{10}}{\sqrt{20}} & 0 & 0 \end{pmatrix}$$

We would interpret this kinds of fluctuation as ripples around the disk because operator  $Tr(\phi^k)$  breaks the  $U(1)$  global symmetry to the discrete group  $\mathbb{Z}_k$ .

We can also check this point by looking at  $R^2$  matrix. Taking  $\phi' = \phi_0 + \epsilon \delta \phi_k$ , where  $\phi_0$  is the droplet background,  $\epsilon$  is the small parameter which is kept only to first order, and  $\delta \phi_k$  is the fluctuation corresponding to  $Tr(\phi^k)$ . Then the  $R^2$  matrix can be written as

$$R_{i,j}^2 = \zeta(\sqrt{2i-1}\delta_{i,j} + \epsilon \frac{[\sqrt{j+k-1}\sqrt{\binom{j+k-2}{j-1}} + \sqrt{j}\sqrt{\binom{j+k-1}{j}}]\delta_{i-k,j} + [\sqrt{i+k-1}\sqrt{\binom{i+k-2}{i-1}} + \sqrt{i}\sqrt{\binom{i+k-1}{i}}]\delta_{i,j-k}}{\sqrt{\sum_{j=1}^{N_f-k+1}\binom{j+k-2}{j-1}}}) \quad (6.4.6)$$

For example, we take  $N_c = 6$  and  $k = 3$ , then the  $R^2$  matrix will be

$$R^2 = \zeta \begin{pmatrix} 1 & 0 & 0 & \epsilon \frac{2\sqrt{3}}{\sqrt{20}} & 0 & 0 \\ 0 & 3 & 0 & 0 & \epsilon \frac{4\sqrt{3}}{\sqrt{20}} & 0 \\ 0 & 0 & 5 & 0 & 0 & \epsilon \frac{2\sqrt{30}}{\sqrt{20}} \\ \epsilon \frac{2\sqrt{3}}{\sqrt{20}} & 0 & 0 & 7 & 0 & 0 \\ 0 & \epsilon \frac{4\sqrt{3}}{\sqrt{20}} & 0 & 0 & 9 & 0 \\ 0 & 0 & \epsilon \frac{2\sqrt{30}}{\sqrt{20}} & 0 & 0 & 11 \end{pmatrix}$$

We see that for the mode of  $Tr(\phi^k)$ , only the elements on lines  $k$  units away from the diagonal line get fluctuations, which is consistent with our interpretation of ripples on the disk.

One interesting case is  $k = N_c$ , there is no fluctuation on the  $R^2$  matrix, which turns out to be the same as  $R^2$  matrix of the disk. This can be understood as Umklapp oscillation on the lattice where one cannot distinguish the frequency exceeding the first Brillouin zone against its counterpart in the first Brillouin zone by just looking at the motion of the points on lattice. And we see that if we take large  $N_c$  limit, then the droplet can have higher and higher frequency, which means our matrix description are approaching continuum limit.

For the  $\phi$ -modes, we can find exact soliton solutions for some of the operators, not just first order approximation. Here we just write down the VEV in  $\phi$  part because the VEV got by  $Q$  and  $\tilde{Q}$  are the same as droplet solution for all the cases:

$$Q_1 = \sqrt{\zeta} \begin{pmatrix} & 0 & \cdots & 0 \end{pmatrix}$$

$$\tilde{Q}_1 = \sqrt{\zeta} \begin{pmatrix} & 0 & \cdots & 0 & \sqrt{N_c} \end{pmatrix}$$

It is clear to see that those modes do not turn on operators in  $Q$ -modes. Here is a list for several different  $\phi$ -modes, and their corresponding  $R^2$  matrix.

$Tr(\phi)$ :

$$\phi = \sqrt{\zeta} \begin{pmatrix} q & \sqrt{1} & & & \\ & q & \sqrt{2} & & \\ & & \ddots & \ddots & \\ & & & q & \sqrt{N_c - 1} \\ & & & & q \end{pmatrix}$$

This is corresponding to the displacement of the disk. And we can write the  $R^2$  matrix as

$$R^2 = \zeta \begin{pmatrix} 1 + 2q^2 & 2\sqrt{1}q & 0 & 0 & 0 \\ 2\sqrt{1}q & 3 + 2q^2 & 2\sqrt{2}q & 0 & 0 \\ 0 & 2\sqrt{2}q & 5 + 2q^2 & \ddots & 0 \\ 0 & 0 & \ddots & \ddots & 2\sqrt{N_c - 1}q \\ 0 & 0 & 0 & 2\sqrt{N_c - 1}q & 2N_c + 2q^2 - 1 \end{pmatrix}$$

$Tr(\phi^2)$ :

$$\phi = \sqrt{\zeta} \begin{pmatrix} 0 & \frac{(A+B)}{2}\sqrt{1} & & & \\ \frac{(A-B)}{2}\sqrt{1} & 0 & \frac{(A+B)}{2}\sqrt{2} & & \\ & \frac{(A-B)}{2}\sqrt{2} & \ddots & \ddots & \\ & & \ddots & 0 & \frac{(A+B)}{2}\sqrt{N_c - 1} \\ & & & \frac{(A-B)}{2}\sqrt{N_c - 1} & 0 \end{pmatrix}$$

A and B has to satisfy  $A * B = 1$ . This solution is corresponding to ellipse because we can get this solution by stretching X matrix by a factor of A and compressing Y matrix by a factor of B,  $A * B = 1$  comes from the requirement of preserving the area of the droplet. And we can write the  $R^2$  matrix as

$$R^2 = \zeta \begin{pmatrix} \frac{(A^2+B^2)}{2} & 0 & \frac{\sqrt{1*2}(A^2-B^2)}{2} & & & \\ 0 & \frac{3(A^2+B^2)}{2} & 0 & \frac{\sqrt{2*3}(A^2-B^2)}{2} & & \\ \frac{\sqrt{1*2}(A^2-B^2)}{2} & 0 & \frac{5(A^2+B^2)}{2} & \ddots & \ddots & \\ \frac{\sqrt{2*3}(A^2-B^2)}{2} & \ddots & \ddots & \ddots & 0 & \frac{\sqrt{(N_c-2)*(N_c-1)}(A^2-B^2)}{2} \\ \ddots & \ddots & 0 & \frac{(2N_c-3)(A^2+B^2)}{2} & 0 & \frac{(2N_c-1)(A^2+B^2)}{2} \\ \frac{\sqrt{(N_c-2)*(N_c-1)}(A^2-B^2)}{2} & 0 & \frac{(2N_c-3)(A^2+B^2)}{2} & 0 & \frac{(2N_c-1)(A^2+B^2)}{2} & \frac{\sqrt{(N_c-2)*(N_c-1)}(A^2-B^2)}{2} \end{pmatrix}$$

$$Tr(\phi^{N_c-1}):$$

$$\phi = \sqrt{\zeta} \begin{pmatrix} 0 & \frac{\sqrt{N_c-1+q}}{\sqrt{N-1}} & 0 & 0 & 0 & 0 & 0 \\ \vdots & 0 & \frac{\sqrt{2(N_c-1)+N_cq}}{\sqrt{N-1}} & 0 & 0 & \vdots & \vdots \\ 0 & \vdots & 0 & \frac{\sqrt{3(N_c-1)+N_cq}}{\sqrt{N-1}} & 0 & 0 & 0 \\ 0 & 0 & 0 & 0 & \ddots & 0 & 0 \\ 0 & 0 & 0 & 0 & 0 & \frac{\sqrt{(N_c-2)(N_c-1)+N_cq}}{\sqrt{N-1}} & 0 \\ \frac{\sqrt{q}}{\sqrt{N_c-1}} & 0 & \dots & 0 & 0 & 0 & \frac{\sqrt{(N_c-1)^2+(N_c-1)q}}{\sqrt{N-1}} \\ 0 & \sqrt{q} & 0 & \dots & 0 & 0 & 0 \end{pmatrix}$$

And we can write the  $R^2$  matrix as

$$R^2 = \zeta \begin{pmatrix} 1 + \frac{2q}{N_c-1} & 0 & 0 & 0 & 0 & \frac{2\sqrt{q}\sqrt{N_c-1+q}}{\sqrt{N_c-1}} \\ 0 & 3 + \frac{2N_cq}{N_c-1} & 0 & 0 & 0 & \vdots \\ 0 & 0 & 5 + \frac{2N_cq}{N_c-1} & 0 & 0 & 0 \\ 0 & 0 & 0 & \ddots & 0 & 0 \\ 0 & 0 & 0 & 0 & 2N_c - 3 + \frac{2N_cq}{N_c-1} & 0 \\ \frac{2\sqrt{q}\sqrt{N_c-1+q}}{\sqrt{N_c-1}} & 0 & \dots & 0 & 0 & 2N_c - 1 + \frac{2q}{N_c-1} \end{pmatrix}$$

$Tr(\phi^{N_c}):$

$$\phi = \sqrt{\zeta} \begin{pmatrix} 0 & \sqrt{1+q} & & & \\ & 0 & \sqrt{2+q} & & \\ & & \ddots & \ddots & \\ & & & 0 & \sqrt{N_c-1+q} \\ \sqrt{q} & & & & 0 \end{pmatrix}$$

And we can write the  $R^2$  matrix as

$$R^2 = \zeta \begin{pmatrix} 1 & & & & \\ & 3 & & & \\ & & 5 & & \\ & & & \ddots & \\ & & & & 2N_c - 1 \end{pmatrix}$$

For this case, we get the same  $R^2$  matrix as the disk, but describing different physics state.

Also, we can find the fluctuations for Q-modes as well, and they can be written as

$$Q = \delta_{N_c, (i+k-1)} \quad (6.4.7)$$

Other elements are all zero. Those modes are corresponding to direction in moduli space described by  $\tilde{Q}\phi^{k-1}Q$ . And for the Q-mode case, the fluctuation does not change  $R^2$  at the leading order.

Again, we find exact solutions for the operators describing Q-modes:

For  $\tilde{Q}\phi^{k-1}Q$ , we can have the solution as

$$a_{i,j}^\phi = \begin{pmatrix} \sqrt{i}\delta_{i,j-1} & \text{for } 1 \leq i \leq N_c - k + 1 \\ \sqrt{i+q}\delta_{i,j-1} & \text{for } N_c - k + 2 \leq i \leq N_c \end{pmatrix}$$

$$a_i^Q = \sqrt{q}\delta_{i,N_c-k+1}$$

$$a_i^{\tilde{Q}} = \sqrt{N_c + q}\delta_{i,N_c}$$

And the  $R^2$  matrix can be written as

$$R_{i,j}^2 = \begin{pmatrix} (2i-1)\delta_{i,j} & \text{for } 1 \leq i \leq N_c - k \\ (2i-1+2q)\delta_{i,j} & \text{for } N_c - k + 1 \leq i \leq N_c \end{pmatrix}$$

From the  $R^2$  matrix we can find that Q-modes are corresponding to cutting droplet into one smaller disk and one annulus, then push the annulus far away from the smaller disk.

For example,  $\tilde{Q}Q$ :

$$\phi = \sqrt{\zeta} \begin{pmatrix} 0 & \sqrt{1} & & & \\ & 0 & \sqrt{2} & & \\ & & \ddots & \ddots & \\ & & & 0 & \sqrt{N_c-1} \\ & & & & 0 \end{pmatrix}$$

$$Q = \sqrt{\zeta} \begin{pmatrix} 0 & \cdots & 0 & \sqrt{q} \end{pmatrix}$$

$$\tilde{Q} = \sqrt{\zeta} \begin{pmatrix} 0 & \cdots & 0 & \sqrt{N_c+q} \end{pmatrix}$$

And the corresponding  $R^2$  matrix is

$$R^2 = \zeta \begin{pmatrix} 1 & & & & \\ & 3 & & & \\ & & 5 & & \\ & & & \ddots & \\ & & & & 2N_c - 3 \\ & & & & & 2N_c - 1 + 2q \end{pmatrix}$$

This corresponding to pushing the most outer ring away from the inner disk.



$\tilde{Q}\phi Q$ :

$$\phi = \sqrt{\zeta} \begin{pmatrix} 0 & \sqrt{1} & & & & \\ & 0 & \sqrt{2} & & & \\ & & \ddots & \ddots & & \\ & & & 0 & \sqrt{N_c-1} & \\ & & & & \ddots & \sqrt{N_c-1+q} \\ & & & & & 0 \end{pmatrix}$$

$$Q = \sqrt{\zeta} \begin{pmatrix} 0 & \cdots & 0 & \sqrt{q} & 0 \end{pmatrix}$$

$$\tilde{Q} = \sqrt{\zeta} \begin{pmatrix} 0 & \cdots & 0 & \sqrt{N_c+q} \end{pmatrix}$$

And the corresponding  $R^2$  matrix is

$$R^2 = \zeta \begin{pmatrix} 1 & & & & & \\ & 3 & & & & \\ & & 5 & & & \\ & & & \ddots & & \\ & & & & 2N_c-5 & \\ & & & & & 2N_c-3+2q \\ & & & & & & 2N_c-1+2q \end{pmatrix}$$

This corresponding to pushing the most 2 outer rings far away.

$\tilde{Q}\phi^{N_c-1}Q$ :

$$\phi = \sqrt{\zeta} \begin{pmatrix} 0 & \sqrt{1+q} & & & & \\ & 0 & \sqrt{2+q} & & & \\ & & \ddots & \ddots & & \\ & & & 0 & \sqrt{N_c-1+q} & \\ & & & & 0 & \end{pmatrix}$$

$$Q = \sqrt{\zeta} \begin{pmatrix} \sqrt{q} & \cdots & 0 \end{pmatrix}$$

$$\tilde{Q} = \sqrt{\zeta} \begin{pmatrix} 0 & \cdots & 0 & \sqrt{N_c+q} \end{pmatrix}$$

And the corresponding  $R^2$  matrix is

$$R^2 = \zeta \begin{pmatrix} 1+q & & & & & \\ & 3+q & & & & \\ & & 5+q & & & \\ & & & \ddots & & \\ & & & & 2N_c-1+q \end{pmatrix}$$

From the  $R^2$  matrix, we can see that this solution corresponding to pushing the whole disk to an annulus.

### 6.4.2 Multiple flavor case

We now increase the flavor number. The solution is just copies of single droplet case, which describes multiple droplets.

$$\phi_{0,N_i} = \sqrt{\zeta} \begin{pmatrix} 0 & \sqrt{1} & & & \\ & 0 & \sqrt{2} & & \\ & & \ddots & \ddots & \\ & & & 0 & \sqrt{N_i-1} \\ & & & & 0 \end{pmatrix} \quad (6.4.8)$$

$$\phi_0 = \text{Diag}(\phi_{0,N_1}, \dots, \phi_{0,N_i}, \dots, \phi_{0,N_{N'_f}}) \quad (6.4.9)$$

$$Q_{i,0} = \sqrt{\zeta} (\underbrace{0, \dots, 0}_{N_1}, \dots, \underbrace{0, \dots, 0}_{N_i}, \dots, \underbrace{0, \dots, 0}_{N_{N'_f}}) \quad (6.4.10)$$

$$\tilde{Q}_{i,0} = \sqrt{\zeta} (\underbrace{0, \dots, 0}_{N_1}, \dots, \underbrace{0, \dots, \sqrt{N_i}}_{N_i}, \dots, \underbrace{0, \dots, 0}_{N_{N'_f}}) \quad (6.4.11)$$

$$X = [1 - \frac{\mathcal{M}_Q^2}{2\zeta} - \frac{m_\phi^2}{2\zeta} (\mathcal{N} - 1 - \frac{1}{2\zeta} \phi_0^\dagger \phi_0)] X_0 \quad (6.4.12)$$

where

$$\mathcal{N} \equiv \text{diag}(\underbrace{N_1, \dots, N_1}_{N_1}, \dots, \underbrace{N_i, \dots, N_i}_{N_i}, \dots, \underbrace{N_{N'_f}, \dots, N_{N'_f}}_{N_{N'_f}}) \quad (6.4.13)$$

$$\mathcal{M}_Q^2 \equiv \text{diag}(\underbrace{m_{Q_1}^2, \dots, m_{Q_1}^2}_{N_1}, \dots, \underbrace{m_{Q_i}^2, \dots, m_{Q_i}^2}_{N_i}, \dots, \underbrace{m_{Q_{N'_f}}^2, \dots, m_{Q_{N'_f}}^2}_{N_{N'_f}}) \quad (6.4.14)$$

$$V = \sum_{i=1}^{N'_f} [\frac{(N_i-1)N_i}{2} m_\phi^2 \zeta + N_i m_{Q_i}^2 \zeta] + \mathcal{O}(m^4) \quad (6.4.15)$$

The spectrum of light modes can be written as

$$m_i^2 = k_i m_\phi^2 + \mathcal{O}(m^4/\zeta) \quad (6.4.16)$$

$$m_{ij}^2 = (k_i + N_j - N_i) m_\phi^2 - m_{Q_i}^2 + m_{Q_j}^2 + \mathcal{O}(m^4/\zeta) \quad (6.4.17)$$

$$m_i^2 = (k_i - 1) m_\phi^2 + 2m_{Q_i}^2 + \mathcal{O}(m^4/\zeta) \quad (6.4.18)$$

$$m_{ij}^2 = (k_{(i,j)} - 1) m_\phi^2 + m_{Q_i}^2 + m_{Q_j}^2 + \mathcal{O}(m^4/\zeta) \quad (6.4.19)$$

where  $k_i$  runs from 1 to  $N_i$ .

For the first group of modes, we find the eigenvectors for them are the same as single droplet case, appearing in each block respectively.

The second group is interesting. We assume  $m_{Q_i} < m_\phi$ , then if  $|N_i - N_j| > 1$ , we will get tachyonic states anyway. If  $|N_i - N_j| = 1$ , the smaller Q mass has to belong to bigger droplet so that we do not get tachyonic state. For  $N_i = N_j$ , all states are stable. It is a strong constraint which will be used when we count the number of possible vacua.

We take two droplets case as an example, because more droplets cases are just simple copies of two droplets case in corresponding blocks. When  $k < (N_{f2} - N_{f1} + 1)$  (which may include tachyonic, massless or the lightest massive state, depending on the choice of parameters), we can find that the eigenvectors as (we set the first diagonal block corresponding to  $N_{f1}$ , the smaller disk)

$$a(\phi)_{i,j} = \frac{\sqrt{\binom{j+k-2}{j-1}}}{\sqrt{\sum_{j=1}^{N_{f1}+1} \binom{j+k-2}{j-1}}} \delta_{N_{f1}+i-k,j}$$

$$a(\tilde{Q}_1)_i = \pm \frac{\sqrt{\binom{N_{f1}+k-1}{N_{f1}}}}{\sqrt{\sum_{j=1}^{N_{f1}+1} \binom{j+k-2}{j-1}}} \delta_{2N_{f1}+k,i}$$

For example, we take  $N_{f1} = 2$ ,  $N_{f2} = 5$  and  $k = 3$ , the eigenvector for this state should be

$$\phi = \begin{pmatrix} 0 & 0 & 0 & 0 & 0 & 0 & 0 \\ 0 & 0 & 0 & 0 & 0 & 0 & 0 \\ 0 & 0 & 0 & 0 & 0 & 0 & 0 \\ 0 & 0 & 0 & 0 & 0 & 0 & 0 \\ \frac{1}{\sqrt{10}} & 0 & 0 & 0 & 0 & 0 & 0 \\ 0 & \frac{\sqrt{3}}{\sqrt{10}} & 0 & 0 & 0 & 0 & 0 \\ 0 & 0 & 0 & 0 & 0 & 0 & 0 \end{pmatrix}$$

$$\tilde{Q}_1 = \begin{pmatrix} 0 & 0 & 0 & 0 & 0 & 0 & \pm \frac{\sqrt{6}}{\sqrt{10}} \end{pmatrix}$$

Here we can see that in those states,  $\tilde{Q}$  is turned on and Q is still zero. Recall that in the vacuum,  $\phi$  and  $\tilde{Q}$  have non-zero elements, and Q are always zero. Thus we cannot form any gauge invariant operator by  $\phi$ , Q and  $\tilde{Q}$  which is turned on for such kind of fluctuation. So we believe that those states are not corresponding to any directions on moduli space.

And when  $k \geq (N_{f2} - N_{f1} + 1)$ , the states will become massive states, and there will be only  $\phi$  field turned on. Then we can write the eigenvector as

$$a(\phi)_{i,j} = \frac{\sqrt{\binom{j+k-2}{j-1}}}{\sqrt{\sum_{j=1}^{N_{f2}-k+1} \binom{j+k-2}{j-1}}} \delta_{N_{f1}+i-k,j}$$

And we should notice that the range of  $j$  is  $1, \dots, N_{f2} - k + 1$ , different from the previous case where  $j$  is  $1, \dots, N_{f1}$ .

For example, we take again  $N_{f1} = 2$ ,  $N_{f2} = 5$  but  $k = 4$  for this time,

$$\phi = \begin{pmatrix} 0 & 0 & 0 & 0 & 0 & 0 & 0 \\ 0 & 0 & 0 & 0 & 0 & 0 & 0 \\ 0 & 0 & 0 & 0 & 0 & 0 & 0 \\ 0 & 0 & 0 & 0 & 0 & 0 & 0 \\ 0 & 0 & 0 & 0 & 0 & 0 & 0 \\ \frac{1}{\sqrt{5}} & 0 & 0 & 0 & 0 & 0 & 0 \\ 0 & \frac{\sqrt{4}}{\sqrt{5}} & 0 & 0 & 0 & 0 & 0 \end{pmatrix}$$

The eigenvectors for the third and forth groups are not complicated to write. For the third group,

$$Q_{1,i} = \delta_{N_1, (i+k_1-1)} \quad (6.4.20)$$

$$Q_{2,i} = \delta_{N_1+N_2, (i+k_2-1)} \quad (6.4.21)$$

For the forth group,

$$Q_{1,i} = \delta_{N_1+N_2, (i+k_2-1)} \quad (6.4.22)$$

$$Q_{2,i} = \delta_{N_1, (i+k_1-1)} \quad (6.4.23)$$

## 6.5 Counting the number of vacua

With studying this simple model in details, we are finally ready to pursue our original goal, counting the number of (meta)-stable vacua.

### 6.5.1 How to get a stable vacuum state

We are only interested in the case when  $\phi$  field is turned on, so there are two kinds of cases to discuss: Only  $\phi$  is turned on, or both  $\phi$ ,  $\tilde{Q}$  and  $Q$  are turned on. For the first case, we know that vacuum can only appear when  $\phi$  is at origin, which means it does not get vacuum expectation value. This case is stable, so it contributes to the vacuum number by one, not a big deal. The second case is more interesting, we find that there are two rules which have to be satisfied so that we can get a (meta)-stable vacuum. Firstly, the F-I term, which is proportional to identity matrix, has to be totally canceled by  $\phi$ 's and  $Q$ 's. Moreover, if there are several sizes of  $\phi$  fields, the difference between each block has to be smaller or equal to one, which means we can only have  $n \times n$  matrix and  $(n+1) \times (n+1)$  matrices. So there are three ways to cancel the identity

matrix from F-I term, smaller droplet with one flavor to form an  $n \times n$  identity matrix, bigger droplet with one flavor to form an  $(n + 1) \times (n + 1)$  identity matrix, and only one flavor to cancel one element in F-I term.

### 6.5.2 How many vacua there are when we fix $N_c$ and $N_f$

The case only with  $\phi$  contributes one, so it will not be important, and we will focus on the second case, which both  $\phi$ 's and Q's appear. Firstly, we have  $N_f$  flavors, and treat them distinguishable with each other. And we take out  $N_{f1}$  out of them to obtain non-zero vacuum expectation values, so there are  $N_f - N_{f1}$  of them stay in the origin of phase space.  $N_{f1}$  can be divided into three kinds, Q's for smaller droplets, Q's for bigger droplets and Q's for individual 1's. Assume there are  $N_{f2}$  Q's for canceling individual 1's in F-I term, without  $\phi$  fields. So there are  $N_c - N_{f2}$  spaces left to be filled by droplets. Because of gauge symmetry which appears as permutation of blocks in the whole  $N_c \times N_c$  matrix, we can put all of individual 1's together, and the left space form an  $(N_c - N_{f2}) \times (N_c - N_{f2})$  block to be filled by  $N_{f1} - N_{f2}$  droplets. One can find that if we do not care about the sequence of the droplets (because changing the sequence of droplets does not generate new vacuum), there is only a unique way to fill up the blocks by droplets when the number of droplets is fixed.

Now we need to find out the range of  $N_{f1}$  and  $N_{f2}$ . Firstly,  $N_{f1}$  has to be smaller than  $\text{Min}(N_f, N_c - 1)$ . We are discussing the case having at least one droplet, and the smallest possible size of the droplet is 2 by 2 matrix, so there are at most  $(N_c - 1)$  flavors getting VEV. Then after we fix  $N_{f1}$ , there will be  $N_{f1} - N_{f2}$  droplets and  $N_c - N_{f2}$  spaces for droplets. For the reason that the smallest size of droplets is 2 by 2 matrix, we get the constrain as  $N_{f1} - N_{f2} \leq [\frac{N_c - N_{f2}}{2}]$ , where [...] means taking the integer part of the number. Thus we can get lower bound of  $N_{f2}$  as  $\text{Max}(0, 2N_{f1} - N_c)$ . Also from the definition of  $N_{f2}$ , we can get its upper bound as  $\text{Min}(N_c - 2, N_{f1} - 1)$ .

Now we can write the expression for the total number of vacuums,

$$\sum_{N_{f1}=1}^{\text{Min}(N_f, N_c-1)} \sum_{N_{f2}=\text{Max}(0, 2N_{f1}-N_c)}^{\text{Min}(N_c-2, N_{f1}-1)} \frac{N_f!}{(N_f - N_{f1})! N_{f2}! a! b!} \quad (6.5.1)$$

where a and b are numbers of smaller and larger droplets. Another way to understand this formula is that we can consider the total number of  $N_f$  is divided into four parts, Q's without non-zero VEV, Q's for vanishing individual 1's in F-I term, Q's for smaller droplets and Q's for larger droplets.

It is not easy to go further without any approximation because general expressions for a and

b are complicated. But if we assume  $N_f$  is a large number and only care about the dominant part of the expression, then we can deal with it in a simple way. Firstly we see that the sum of the four terms in dominator is  $N_f$  which is fixed, so we know that the minimal value of the dominator is obtained when we set

$$N_{f1} = \frac{3}{4}N_f$$

$$N_{f2} = a = b = \frac{1}{4}N_f$$

And after applying Sterling formula, we can get the dominant part of the expression as  $4^{N_f}$ . A very rough approximation of correction around dominant part gives a factor  $O(N_f^2, N_f N_c, N_c^2)$  in the number of vacua, so the total number of vacua will be approximately equal to

$$e^{N_f \ln 4 + O(\ln F(N_f, N_c))}$$

where  $F(N_f, N_c)$  is some function of order  $N_f^2$ ,  $N_f N_c$  or  $N_c^2$ . So the total number of (meta)-stable vacua is a very large number if we choose  $N_f$  and  $N_c$  are large.

### 6.5.3 Life time of the meta-stable vacua

Now, we need to calculate the life time of the meta-stable vacuum. From the argument of instanton, we know the decay rate of a meta-stable vacuum is

$$\Gamma \sim e^{-(S_E(\phi(r)) - S_E(\phi_+))} \equiv e^{-B}$$

where  $\phi_+$  is the vacuum before decay, and  $S_E$  is the action written in Euclidian form which can be generally expressed as

$$S_E = 2\pi^2 \int_0^\infty r^3 dr \left[ \frac{1}{2} \dot{\phi}^2 + V(\phi) \right]$$

For convenience, we can set  $V(\phi_+) = 0$ , so  $S_E(\phi_+)$  in  $\Gamma$  vanishes. The evolution of  $\phi$  follows the equation derived from the action

$$\ddot{\phi} + \frac{3}{r} \dot{\phi} = V'(\phi)$$

This is actually an equation for describing the motion under potential  $V$  with a time dependent damping term. And to simplify the equation, we take  $z = \ln(r)$ , and then the equation changes to

$$\frac{d^2}{dz^2} \phi + 2 \frac{d}{dz} \phi = V'(\phi) e^{2z}$$

To get rid of the  $e^{2z}$  term in the equation, we take  $\phi = -\frac{\lambda}{8} \chi e^{2z}$  where  $\lambda$  has same order as  $V'$ .

Then we can get the equation as

$$\frac{1}{8} \ddot{\chi} + \frac{3}{4} \dot{\chi} + \chi = -\frac{V'}{\lambda}$$

On left hand side, coefficients before  $\chi, \dot{\chi}$  and  $\ddot{\chi}$  are all  $O(1)$ . On the right hand side,  $\frac{V'}{\lambda}$  is also  $O(1)$ . So we should expect the solution of the equation,  $\chi$ , is a function of  $O(1)$ .

Another ingredient needed to estimate the order of decay rate is the typical time of the evolution. Although the integration is from 0 to  $\infty$  for Euclidian time  $r$ , there is a typical time  $R$ , after that time, the kinetic term in  $S_E(\phi)$  is almost zero, and the potential part are almost canceled by  $S_E(\phi_+)$ . So we can neglect the contribution to  $B$  after that typical time.

Let us assume the potential has the a general form in our case as

$$V(\phi) = m^2 \xi f\left(\frac{\phi}{\sqrt{\xi}}\right)$$

where  $f(\frac{\phi}{\sqrt{\xi}})$  is an  $O(1)$  function. So we get

$$V'(\phi) = m^2 \sqrt{\xi} f'(\phi/\sqrt{\xi})$$

Here  $f'(\phi/\sqrt{\xi})$  is actually  $\frac{df(\phi/\sqrt{\xi})}{d(\frac{\phi}{\sqrt{\xi}})}$  which is again an  $O(1)$  number.

Firstly, we need to estimate the order of  $\frac{1}{2}\dot{\phi}^2$  term in  $B$ . We know  $\phi = -\frac{\lambda}{8}\xi e^{2z}$ , so we can get

$$\dot{\phi}^2 \sim \lambda^2 r^2$$

According to the definition, we know  $\lambda \sim m^2 \sqrt{\xi}$ . So

$$2\pi^2 \int_0^R dr r^3 \frac{1}{2} \dot{\phi}^2 \sim \frac{\pi^2}{6} m^4 \xi R^6$$

And the second term in  $B$  will be

$$2\pi^2 \int_0^\infty r^3 dr V(\phi) \sim \frac{\pi^2}{2} m^2 \xi R^4$$

The last step is to estimate the typical time  $R$ . The velocity of evolution,  $\frac{d\phi}{dr}$ , is  $m^2 \sqrt{\xi} r$  times an  $O(1)$  function. And the change of  $\phi$  during the evolution is of order  $\sqrt{\xi}$ . So

$$R \sim \frac{1}{m}$$

Finally, we get

$$B \sim \frac{\xi}{m^2}$$

which in our case is a large number. So the decay rate of meta-stable vacuum is very small, thus their life time is long.

## Bibliography

- [1] K. A. Intriligator and N. Seiberg, Nucl. Phys. Proc. Suppl. **45BC**, 1 (1996) [hep-th/9509066].
- [2] J. Gray, A. Hanany, Y. H. He, V. Jejjala and N. Mekareeya, “SQCD: A Geometric Apercu,” arXiv:0803.4257 [hep-th].
- [3] A. Hanany and N. Mekareeya, “Counting Gauge Invariant Operators in SQCD with Classical Gauge Groups,” arXiv:0805.3728 [hep-th].
- [4] Y. Noma, T. Nakatsu and T. Tamakoshi, “Plethystics and instantons on ALE spaces,” arXiv:hep-th/0611324.
- [5] D. Forcella, A. Hanany, and A. Zaffaroni, “Baryonic generating functions,” arXiv:hep-th/0701236.
- [6] A. Butti, D. Forcella, A. Hanany, D. Vegh, and A. Zaffaroni, “Counting chiral operators in quiver gauge theories,” arXiv:0705.2771 [hep-th].
- [7] D. Forcella, “BPS Partition Functions for Quiver Gauge Theories: Counting Fermionic Operators,” arXiv:0705.2989 [hep-th].
- [8] P. Pouliot, “Molien function for duality,” JHEP **9901** (1999) 021 [arXiv:hep-th/9812015].
- [9] C. Romelsberger, “Counting chiral primaries in N=1, d=4 superconformal field theories,” Nucl. Phys. B **747** (2006) 329 [arXiv:hep-th/0510060].
- [10] A. Hanany, “Counting BPS operators in the chiral ring: The plethystic story,” AIP Conf. Proc. **939**, 165 (2007).
- [11] F. A. Dolan, “Counting BPS operators in N=4 SYM,” Nucl. Phys. B **790**, 432 (2008) [arXiv:0704.1038 [hep-th]].
- [12] F. A. Dolan and H. Osborn, “Applications of the Superconformal Index for Protected Operators and q-Hypergeometric Identities to N=1 Dual Theories,” arXiv:0801.4947 [hep-th].



- [13] D. Kutasov, “A Comment on duality in  $N=1$  supersymmetric nonAbelian gauge theories,” *Phys. Lett. B* **351**, 230 (1995) [arXiv:hep-th/9503086].
- [14] D. Kutasov and A. Schwimmer, “On duality in supersymmetric Yang-Mills theory,” *Phys. Lett. B* **354**, 315 (1995) [arXiv:hep-th/9505004].
- [15] D. Kutasov, A. Schwimmer and N. Seiberg, “Chiral Rings, Singularity Theory and Electric-Magnetic Duality,” *Nucl. Phys. B* **459**, 455 (1996) [arXiv:hep-th/9510222].
- [16] A. Giveon and D. Kutasov, “Brane dynamics and gauge theory,” *Rev. Mod. Phys.* **71**, 983 (1999) [arXiv:hep-th/9802067].
- [17] D. Kutasov, A. Parnachev and D. A. Sahakyan, “Central charges and  $U(1)_R$  symmetries in  $N = 1$  super Yang-Mills,” *JHEP* **0311**, 013 (2003) [arXiv:hep-th/0308071].
- [18] A. Parnachev and S. S. Razamat, “Comments on Bounds on Central Charges in  $N=1$  Superconformal Theories,” arXiv:0812.0781 [hep-th].
- [19] R. Jackiw and A. P. Polychronakos, *Phys. Rev. D* **62**, 085019 (2000) [hep-th/0004083].
- [20] S. Bahcall and L. Susskind, Fluid dynamics, Chern-Simons theory and the quantum Hall effect, *Int. J. Mod. Phys. B* **5**, 2735 (1991).
- [21] D. Bak, K. -M. Lee and J. -H. Park, *Phys. Lett. B* **501**, 305 (2001) [hep-th/0011244].
- [22] L. Susskind, hep-th/0101029.
- [23] R. Jackiw, S. Y. Pi and A. P. Polychronakos, *Annals Phys.* **301**, 157 (2002) [hep-th/0206014].
- [24] A. P. Polychronakos, *Annals Phys.* **301**, 174 (2002) [hep-th/0206013].
- [25] A. P. Polychronakos, arXiv:0706.1095 [hep-th].
- [26] Fedele Lizzia, Patrizia Vitale and Alessandro Zampini, *Journal of Physics: Conference Series* **53** (2006) 830C842.